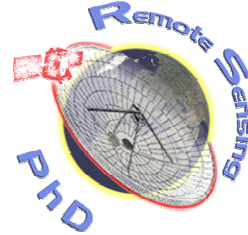


UNIVERSITÀ DI PISA

Dipartimento di Ingegneria dell'Informazione:
Elettronica, Informatica e Telecomunicazioni

Dottorato in Telerilevamento



Tesi di Dottorato

Performance Analysis of Bistatic Radar and Optimization methodology in Multistatic Radar System

Candidato:

Ing. Pietro Stinco

Tutori:

Prof.ssa Maria Sabrina Greco

Prof. Fulvio Gini

Abstract

This work deals with the problem of calculating the Cramér-Rao lower bounds (CRLBs) for bistatic radar channels. To this purpose we exploited the relation between the Ambiguity Function (AF) and the CRLB. The bistatic CRLBs are analyzed and compared to the monostatic counterparts as a function of the bistatic geometric parameters. In the bistatic case both geometry factors and transmitted waveforms play an important role in the shape of the AF, and therefore in the estimation accuracy of the target range and velocity. In particular, the CRLBs depend on the target direction of arrival, the bistatic baseline length, and the distance between the target and the receiver. The CRLBs are then used to select the “optimum” bistatic channel (or set of channels) for the tracking of a radar target moving along a trajectory in a multistatic scenario and for design weighting coefficients for the multistatic detection process. This work also deals with the calculation of the Posterior Cramér-Rao Lower Bound (PCRLB) for sequential target state estimators for a bistatic tracking problem. In the context of tracking, the PCRLB provides a powerful tool, enabling one to determine a lower bound on the optimal achievable accuracy of target state estimation. The bistatic PCRLBs are analyzed and compared to the monostatic counterparts for a fixed target trajectory. Two different kinematic models are analyzed: constant velocity and constant acceleration. The derived bounds are also valid when the target trajectory is characterized by the combination of these two motions.

Acknowledgments

I would like to express my sincere gratitude to Prof. Maria Sabrina Greco and Prof. Fulvio Gini for their precious suggestions and for the great work environment that they have created during the development of this research project. Thank you so much!!

Summary

Introduction	4
1 The Ambiguity Function.....	7
1.1 Introduction	7
1.2 Ambiguity Function of a Rectangular Pulse	9
1.3 Ambiguity Function of a LFM pulse.....	13
1.4 Ambiguity Function of a SFM pulse	16
1.5 Ambiguity Function of a burst of pulses	36
1.6 Ambiguity Function of a burst of rectangular pulses	36
1.7 Ambiguity Function of a burst of LFM pulses	40
2 Bistatic Radar Systems and Bistatic Ambiguity Function.....	44
2.1 Introduction	44
2.2 Bistatic Geometry	45
2.3 Bistatic Ambiguity Function	47
2.4 Active Bistatic Radar Systems: Burst of LFM pulses	48
2.5 Passive Bistatic Radar Systems: SFM pulse	52
3 Channel Performance Evaluation in a Bistatic Radar System	60
3.1 Bistatic Cramér-Rao Lower Bounds	60
3.2 Bistatic Cramér-Rao Lower Bounds for a burst of LFM pulses	64
3.3 Bistatic Cramér-Rao Lower Bounds for a SFM pulse.....	68
4 Multistatic Radar Systems.....	71
4.1 Introduction	71
4.2 Optimal channel selection in a multistatic radar system	71
4.3 Optimization algorithm	79
4.4 Optimum weighting rule for multistatic detection	84
4.5 Performance of the optimum multistatic detector	92
5 Posterior Cramér-Rao Lower Bounds for Bistatic Systems.....	95
5.1 Introduction	95
5.2 Analyzed Scenario	95
5.3 Constant velocity motion.....	97
5.4 Constant acceleration motion	101
5.5 PCRLB for Monostatic and Bistatic radar systems	103
Conclusions	105
APPENDIX A: Relation between CRLB and AF.....	107
APPENDIX B: CRLBs of Doppler and Delay	112
APPENDIX C: CRLBs of Doppler and Delay using a SFM pulse.....	114
APPENDIX D: CRLB derivation: Change of variables	117
APPENDIX E: CRLB derivation: Chain rule	118
References.....	119

Introduction

A bistatic radar is a system in which transmitter and receiver are at separate locations. In the last years, as proved by the numerous experimental systems being built and the results reported in the literature, there is a great interest in these systems.

Bistatic radars are very interesting because they can operate with their own dedicated transmitters, designed for bistatic operation, or with transmitters of opportunity, which are designed for other purposes but suitable for bistatic operation.

In radar system a known waveform is transmitted and the signal reflected from the target of interest is used to estimate the target parameters.

Typically, the received signal is a scaled, delayed and Doppler-shifted version of the transmitted signal. In monostatic configuration, estimation of the time-delay and Doppler shift directly provides information on target range and velocity.

This information can be retrieved also in a bistatic radar configuration, even if the relation between measured (or estimated) time delay and Doppler frequency and target distance and velocity, respectively, is not linear [Tsa97].

To measure the possible global resolution and large error properties of the target parameters estimates, the Ambiguity Function (AF) is often used, both in monostatic and multistatic scenarios [Tsa97], [Dad86], [Bra07], [Der10], [Gri05], [Kel61], [Pap05]. In fact, the AF directly determines the capability of a system to resolve two targets that exist at different ranges from the radar and have different radial velocities. When the receiver target signals have similar energy, the resolution is assumed to be equal to the half-power-width of the AF mainlobe. The AF is also related to the accuracy on the estimation of target range and velocity. In [Van71] a relationship between the ambiguity function and the Fisher information matrix (FIM) was derived, based on the observation that the FIM is derived by the received data log-likelihood function (LLF) and the AF is the LLF excluding the effect of signal attenuation and noise.

The inverse of the Fisher information is the Cramér-Rao lower bound (CRLB), which bounds the error variance of the estimates obtained from the radar measurements. This is useful because it gives an indication of the best achievable performance, independent of the filtering algorithm. In particular, in [Van71] it is shown that when the signal-to-noise power ratio

(SNR) is high, the CRLB is dependent on both the SNR and the second derivatives of the AF, that is, the sharpness of the AF mainlobe.

The novel contribution of this work is the computation of the CRLB on the estimation of range and velocity of a radar target in a bistatic scenario.

Both the Active and the Passive bistatic system are analyzed. In the Active case, the transmitted waveform is a burst of Linear Frequency Modulated (LFM) pulses while in the Passive case the transmitted waveform is a Sinusoidal Frequency Modulated (SFM) pulse. In both the cases, the target signal is received embedded in white Gaussian noise.

These results are obtained after calculating the bistatic ambiguity function of the transmitted signal and exploiting the relation between the AF and the FIM.

The results show that the estimation accuracy in the bistatic scenario depends not only on the transmitted waveform but also on the bistatic geometry, that is, the position of the target with respect to the receiver and the transmitter. In this work, we compare as well the bistatic CRLBs with its monostatic counterparts as a function of number of integrated pulses, target direction of arrival (DOA) and bistatic baseline length (BBL).

The information gained through the calculation of the bistatic CRLBs can be used in a multistatic radar system for the performance evaluation of each channel of a multistatic radar system. As known, multistatic radar utilises multiple transmitter and receiver sites to provide several different monostatic and bistatic channels of observation, leading to an increase in the information on a particular area of surveillance [Che98].

The performance of each bistatic channel heavily depends upon the geometry of the scenario and the position of the target with respect to each receiver and transmitter.

We approach the problem of optimally selecting the transmitter-receiver (TX-RX) pair based upon the bistatic CRLB for each TX-RX pair. The best pair is defined as that exhibiting the lowest bistatic CRLB for the target velocity or range.

These results can be used for the dynamical selection of the TX-RX signals for the tracking of a radar target moving along a trajectory in a multistatic scenario.

This work also deals with the design and performance evaluation of a multistatic radar system where target detection is performed by jointly combining the signals arising from multiple spatially dispersed transmitters and receivers.

The proposed receiver exploits the CRLBs to compute the rules for selecting the best weighting coefficients for fusing the signals from multiple receivers in order to improve the detection performance and the estimation accuracy of the kinematic parameters of the target.

Moreover, in this work, exploiting the general method provided by Tichavsky et al. [Tic98], we derive the Posterior CRLB (PCRLB) of target state for bistatic radar tracking.

The definitions of CRLB and PCRLB are similar.

The CRLB is defined to be the inverse of the Fisher information matrix and provides a mean square error bound on the performance of any unbiased estimator of an unknown parameter vector. The bound is referred to as the PCRLB if this parameter vector is also subject to random fluctuations.

1 The Ambiguity Function

1.1 Introduction

Classically, the properties of radar waveforms are analysed and presented in terms of the Complex Ambiguity Function, originated by Woodward in the 1950s [Wod80].

The Complex Ambiguity Function (CAF) is well known in the context of radar as a key tool for determining target resolution capability, and is a consequence of the nature of the optimal detector, which involves decision-making based on the output of a matched filter determined from the transmitted waveform [Tsa97]. As a matter of fact, the CAF is the auto-correlation of the complex envelope of the waveform with a copy shifted in time and frequency, and presents the point target response of the waveform as a two-dimensional function of range and Doppler, showing the resolution, sidelobe structure and ambiguities in the delay and Doppler domains. The CAF is intuitively appealing and has been very widely used – indeed, it is no exaggeration to say that every serious radar engineer on the planet will have encountered and used the Woodward ambiguity function.

The mathematical definition of the Complex Ambiguity Function is [Tsa97]:

$$X(\tau_H, \tau_a, \nu_H, \nu_a) = \int_{-\infty}^{+\infty} u(t - \tau_a) u^*(t - \tau_H) e^{-j2\pi(\nu_H - \nu_a)t} dt \quad (1.1)$$

where $u(t)$ is the complex envelope of the transmitted signal, τ_a and ν_a are the actual delay and Doppler frequency of the radar target respectively and τ_H and ν_H are the hypothesized delay and frequency.

The Ambiguity Function (AF) is defined as the absolute value of the Complex Ambiguity Function and is clearly maximum for $\tau_H = \tau_a$ and $\nu_H = \nu_a$. The CAF in (1.1) and the AF can be also expressed as a function of τ and ν , where $\tau = \tau_H - \tau_a$ and $\nu = \nu_H - \nu_a$. In this case the definition of the Ambiguity Function is:

$$|X(\tau, \nu)| = \left| \int_{-\infty}^{+\infty} u(t) u^*(t - \tau) \exp(-j2\pi\nu t) dt \right| \quad (1.2)$$

Three properties of the AF are of particular interest [Van71].

If the waveform has energy E , then

$$|X(\tau, \nu)| \leq |X(0, 0)| = E \quad (1.3)$$

Thus, when the filter is matched both in delay and Doppler the response attains the maximum. If the filter is not matched then the response assumes a value lower than the maximum. The second property states that the total area under any ambiguity function is constant and it is given by

$$\int_{-\infty}^{+\infty} \int_{-\infty}^{+\infty} |X(\tau, \nu)|^2 d\tau d\nu = E^2 \quad (1.4)$$

This conservation of energy statement implies that, in the design of waveforms, one cannot remove energy from one portion of the ambiguity surface without placing it somewhere else; it can only be moved around on the ambiguity surface.

The third property is a symmetry relation

$$X(\tau, \nu) = X(-\tau, -\nu) \quad (1.5)$$

Moreover, if we consider the CAF for $\nu=0$, we obtain the autocorrelation function of $u(t)$, similarly, if we consider the CAF for $\tau=0$, we obtain the Fourier transform of $|u(t)|^2$.

It is reasonable to ask how an ideal ambiguity function should be. The answer varies depending on the aim of the system design, but a common goal is the thumbtack shape, which features a single central peak, with the remaining energy spread uniformly throughout the delay-Doppler plane. The lack of any secondary peak implies that there will be no delay or Doppler ambiguities. The uniform plateau suggests low and uniform side lobes, minimizing target masking effects. All of these features are beneficial for a system designed to make high resolution measurement of targets in delay and Doppler, or to perform radar imaging.

1.2 Ambiguity Function of a Rectangular Pulse

As a first example of an AF, let consider the unitary energy rectangular pulse with time duration T given by the following:

$$u(t) = \frac{1}{\sqrt{T}} \text{rect}\left(\frac{t-T/2}{T}\right) \quad (1.6)$$

Applying eq. (1.2) for $\tau > 0$ we get

$$\begin{aligned} X(\tau, \nu) &= \int_{\tau}^T \frac{1}{T} \exp(-j2\pi\nu t) dt = \\ &= \frac{\exp(-j2\pi\nu T) - \exp(-j2\pi\nu\tau)}{-j2\pi\nu T} = \\ &= \frac{1}{j2\pi\nu T} \exp(-j\pi\nu(\tau+T)) \{ \exp(j\pi\nu(T-\tau)) - \exp(-j\pi\nu(T-\tau)) \}. \end{aligned} \quad (1.7)$$

The ambiguity function for $\tau > 0$ is the absolute value of (1.7), therefore:

$$|X(\tau, \nu)| = \left| \frac{\sin(\pi\nu(T-\tau))}{\pi\nu T} \right| \text{ for } 0 \leq \tau \leq T \quad (1.8)$$

Repeating the derivation for $\tau < 0$, the result is similar but with the quantity $(T-\tau)$ replaced by $(T+\tau)$. The AF of the rectangular pulse is therefore

$$|X(\tau, \nu)| = \left| \frac{\sin(\pi\nu(T-|\tau|))}{\pi\nu T} \right| \text{ for } -T \leq \tau \leq T \quad (1.9)$$

and zero elsewhere.

The AF of eq. (1.9) is plotted in Figure 1.1 in a three-dimensional surface plot and in Figure 1.2 as a contour plot. These Figures have been obtained by choosing $T=0.1$ sec

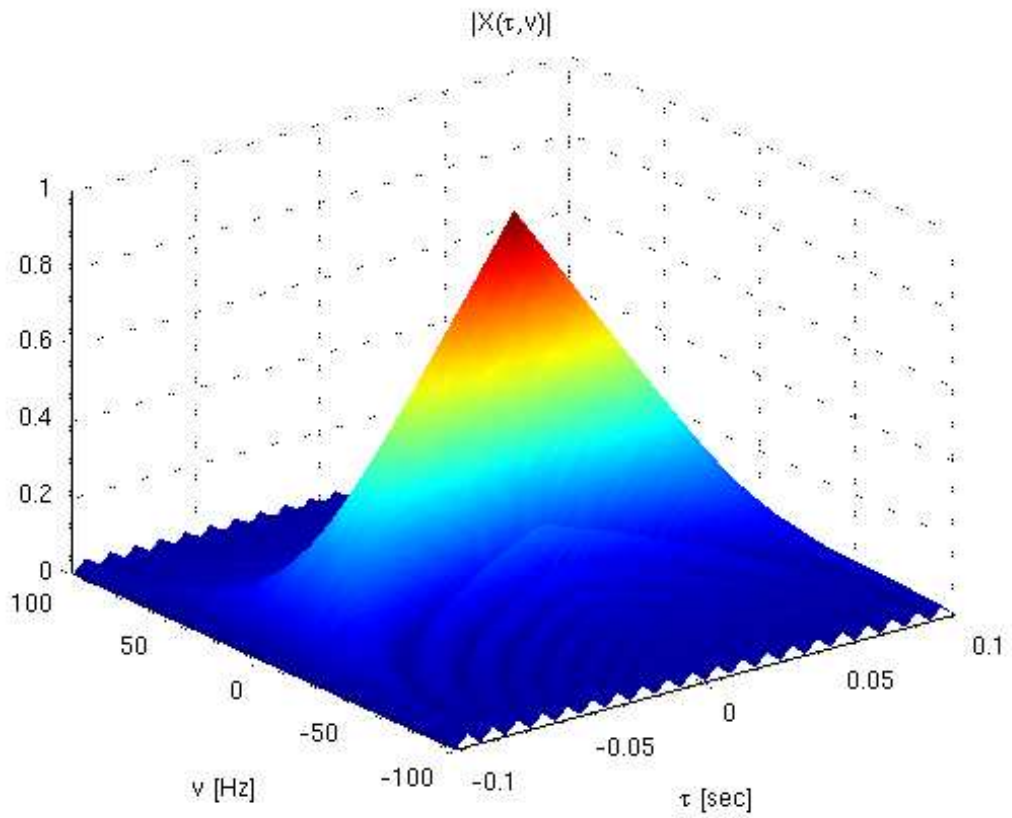


Figure 1.1 – Ambiguity function of a rectangular pulse, 3D-plot.

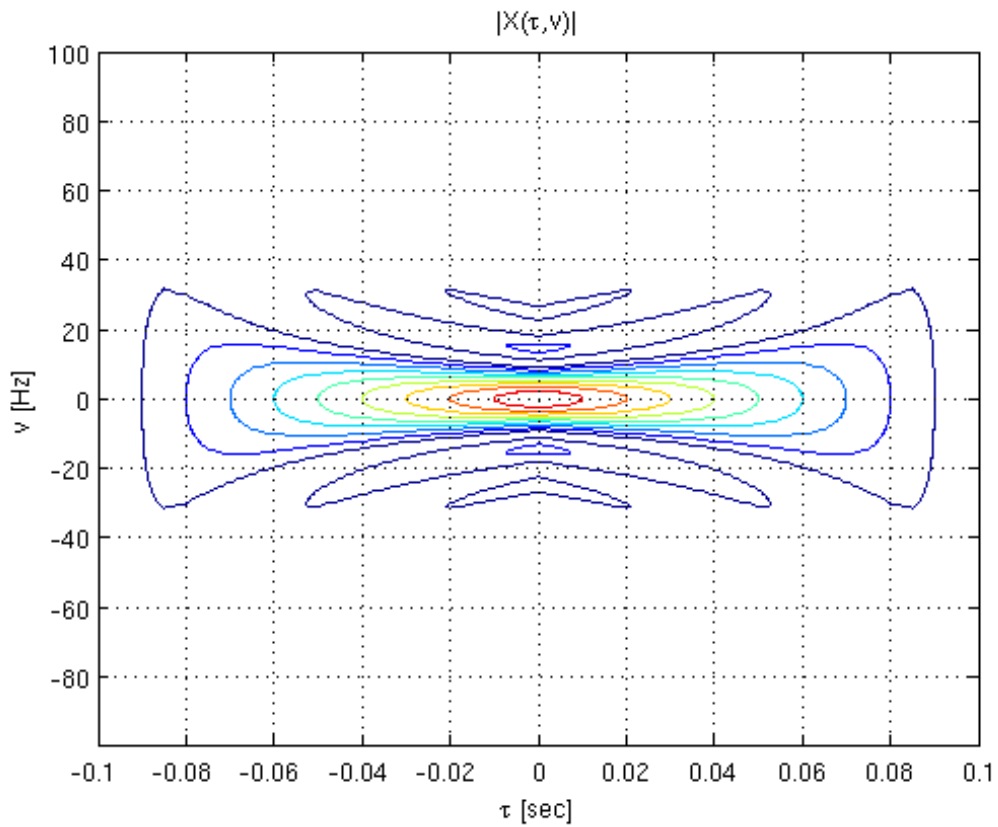


Figure 1.2 - Ambiguity function of a rectangular pulse, contour plot.

It is of particular interest to calculate the AF for $\tau=0$ or $\nu=0$. In the first case we obtain the *zero-delay* cut $|X(0, \nu)|$ which represents the output of the matched filter at the expected peak time $\tau=0$. Using $\tau=0$ in (1.9) immediately gives

$$|X(0, \nu)| = \left| \frac{\sin(\pi\nu T)}{\pi\nu T} \right| \quad (1.10)$$

In the second case we obtain the *zero-Doppler* cut $|X(\tau, 0)|$ which represents the matched filter output when there is no Doppler mismatch. Setting $\nu=0$ in eq. (1.9) and using L'Hopital's rule to solve the indeterminate form, it is easy to verify that

$$|X(\tau, 0)| = 1 - \frac{|\tau|}{T} \quad \text{for } -T \leq \tau \leq T \quad (1.11)$$

Equations (1.10) and (1.11) are the expected *sinc* and *triangle* functions. They are illustrated in Figures 1.3 and 1.4.

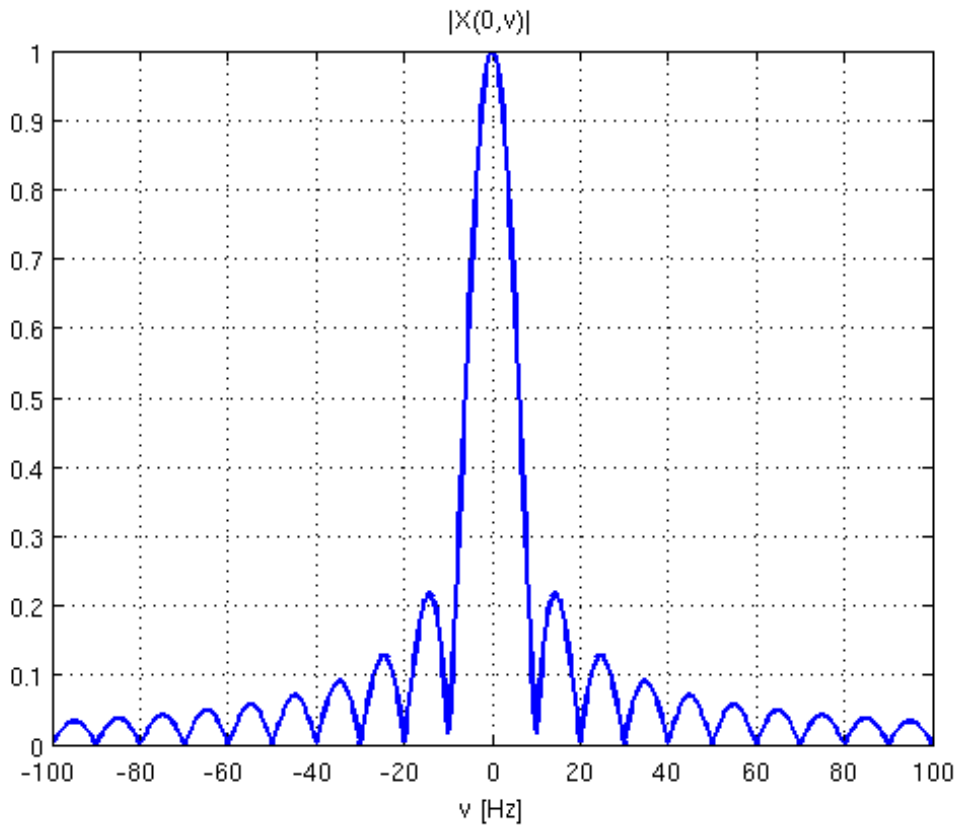


Figure 1.3 – Ambiguity function of a rectangular pulse, zero-delay cut.

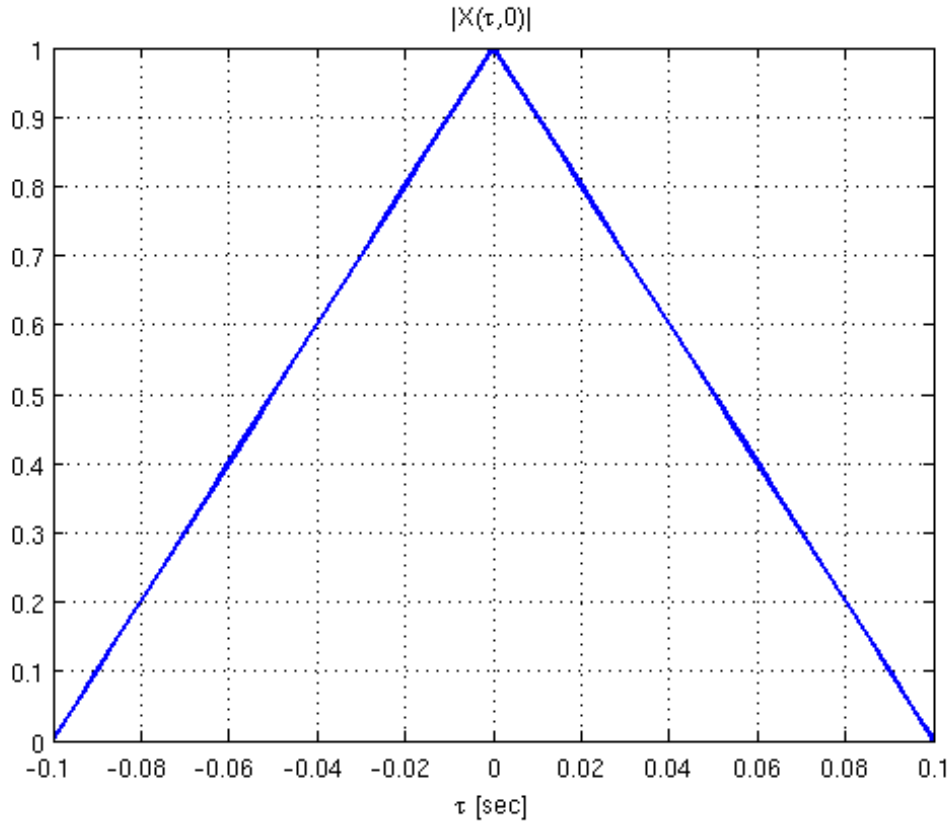


Figure 1.4 - Ambiguity function of a rectangular pulse, zero-Doppler cut.

Recalling that the definition of the Rayleigh resolution is the peak-to-first null distance, by inspection of Figures 1.3 and 1.4, it is clear that T is the delay resolution while $1/T$ is the Doppler resolution. As known, for a monostatic radar system, that is when the transmitter is collocated with the receiver, there is a linear relationship between the delay and the range and between the Doppler and the radial velocity. In this case, when the transmitted waveform is a rectangular pulse, the range resolution is $cT/2$, where c is the speed of light, while the velocity resolution is $cv/2f_c$, where f_c is the carrier frequency. For typical pulse lengths, these are fairly large values. As an example, a $T = 1 \mu\text{sec}$ pulse would exhibit a range resolution of 150 m and a Doppler resolution of 1 MHz . Considering an X-band radar ($f_c = 10 \text{ GHz}$) and the velocity resolution in velocity is of 15000 m/sec .

1.3 Ambiguity Function of a LFM pulse

A simple pulse has only two parameters, its amplitude A and its duration T . The range resolution is directly proportional to T ; better resolution requires a shorter pulse. Most modern radars operate with the transmitter in saturation. That is, any time the pulse is on, its amplitude is kept at the maximum value of A ; amplitude modulation, other than on/off switching, is not used. The energy in the pulse is then A^2T . This mode of operation maximizes the pulse energy, which is then also directly proportional to T . This means that increasing pulse energy improves detection performances. Thus, improving resolution requires a shorter pulse, while improving detection performances requires a longer pulse.

As well known, pulse compression waveforms decouple energy and resolution. Pulse compression waveforms are obtained by adding frequency or phase modulation to a rectangular pulse. There are many coded waveforms in the literature, as an example, in this section the Linear Frequency Modulated (LFM) pulse or CHIRP will be described.

The LFM pulse is defined as

$$u(t) = \frac{1}{\sqrt{T}} e^{j\pi kt^2} \text{rect}\left(\frac{t-T/2}{T}\right) \quad (1.12)$$

where $kT^2=BT$ is the effective time-bandwidth product of the signal and B is the total frequency deviation.

Instead of computing the Ambiguity Function for the LFM pulse, we use an interesting property for arbitrary signal $f(t)$. In particular, if the Complex Ambiguity Function of $f_1(t)$ is $X_1(\tau, \nu)$, that is:

$$f_1(t) \longrightarrow X_1(\tau, \nu) \quad (1.13)$$

then

$$f_2(t) \triangleq f_1(t) e^{j\pi kt^2} \longrightarrow X_2(\tau, \nu) = X_1(\tau, \nu - k\tau) \quad (1.14)$$

This result follows directly from the definition in (1.2). Clearly, similar relation holds for the Ambiguity Function. Thus, a linear frequency sweep shears the ambiguity diagram parallel to the ν -axis.

The Ambiguity Function of the LFM pulse is therefore given by the following:

$$|X(\tau, \nu)| = \left| \frac{\sin[\pi(\nu - k\tau)(T - |\tau|)]}{\pi T(\nu - k\tau)} \right| \quad (1.15)$$

The AF of the LFM pulse is showed in Figure 1.5 in a three-dimensional surface plot and in Figure 1.6 as a contour plot. Figures 1.7 and 1.8 show the zero-delay and the zero-Doppler cuts, respectively. These Figures have been obtained by choosing $T=0.1$ sec and $B=5/T$. From eq. (1.12) it is clear that $|u(t)|^2$ is a rectangular pulse of length T . Recalling that the zero-delay section represents the absolute value of the Fourier transform of $|u(t)|^2$, the response in Figure 1.7 is a *sinc* function with first null at $\nu = 1/T$. The Doppler resolution is therefore the same as a rectangular pulse of length T . On the other hand, it is apparent from Figure 1.8 that the range resolution is almost $1/B$. Therefore, the effect of the matched filter is to compress the long pulse at the input of the receiver into a shorter pulse at the output of the processor, with an accompanying increase in range measurement accuracy.

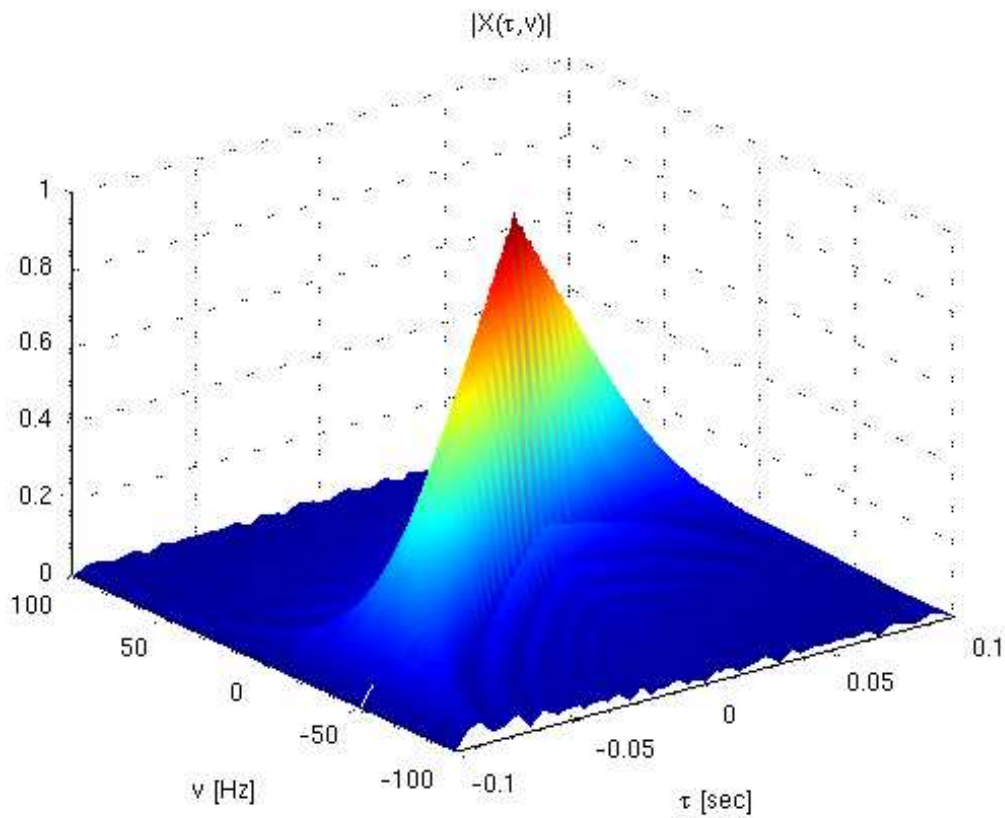


Figure 1.5 – Ambiguity function of a LFM pulse, 3D-plot.

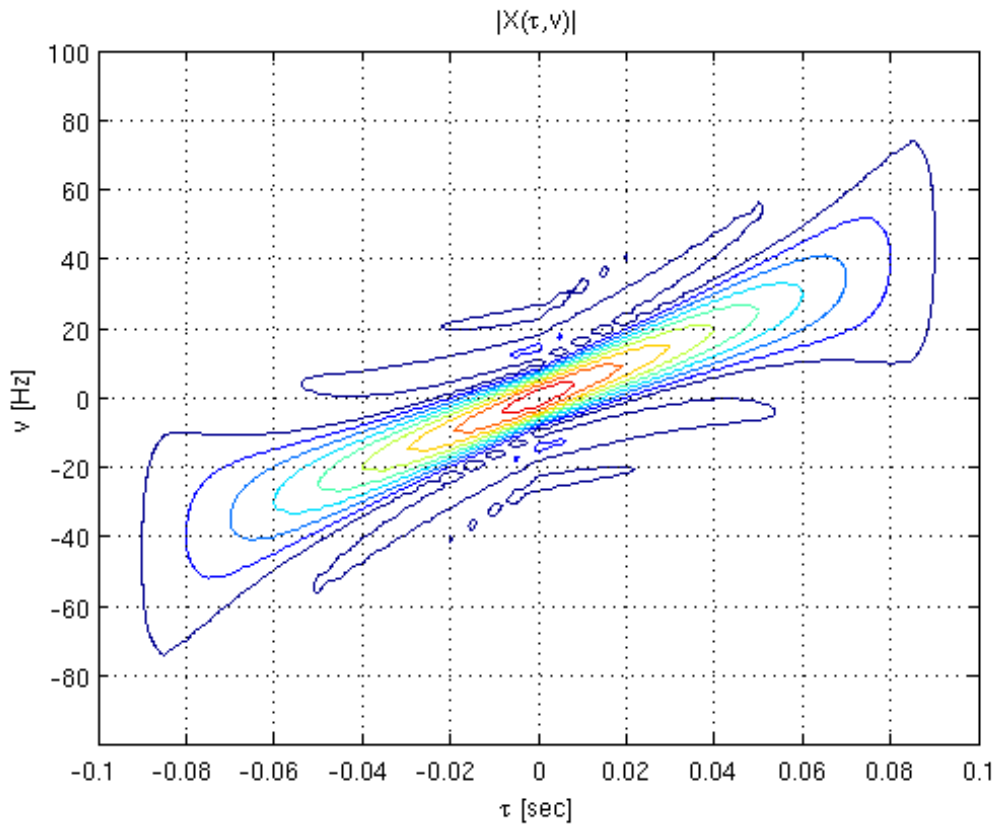


Figure 1.6 - Ambiguity function of a LFM pulse, contour plot.

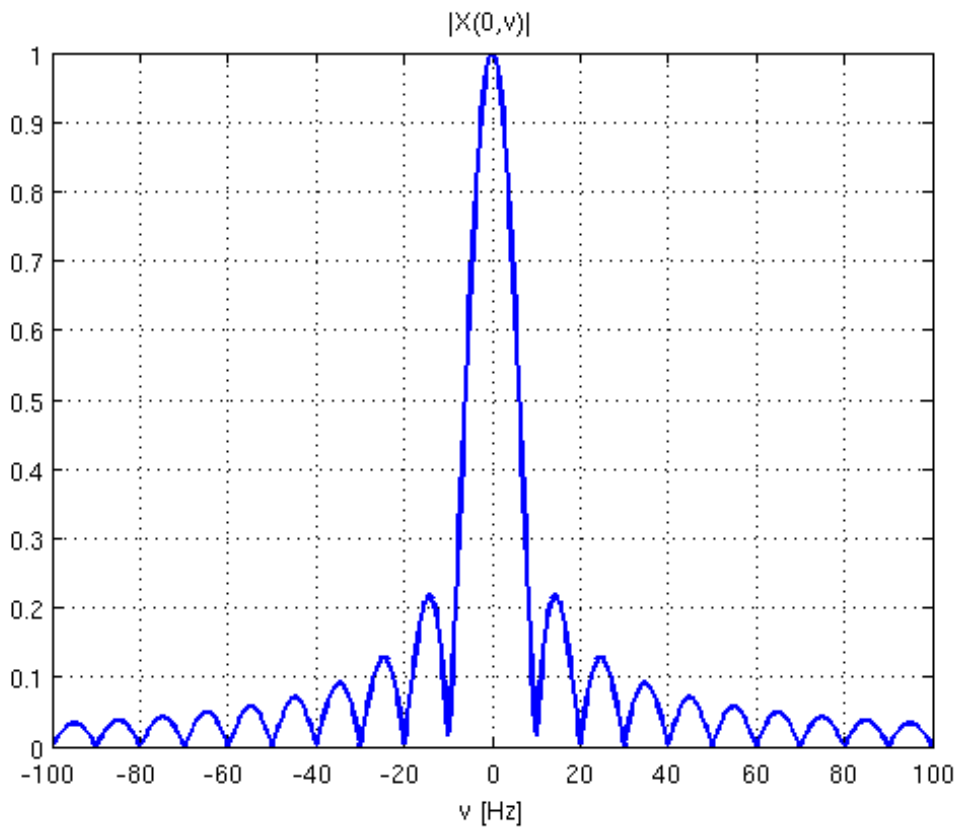


Figure 1.7 – Ambiguity function of a LFM pulse, zero-delay cut.

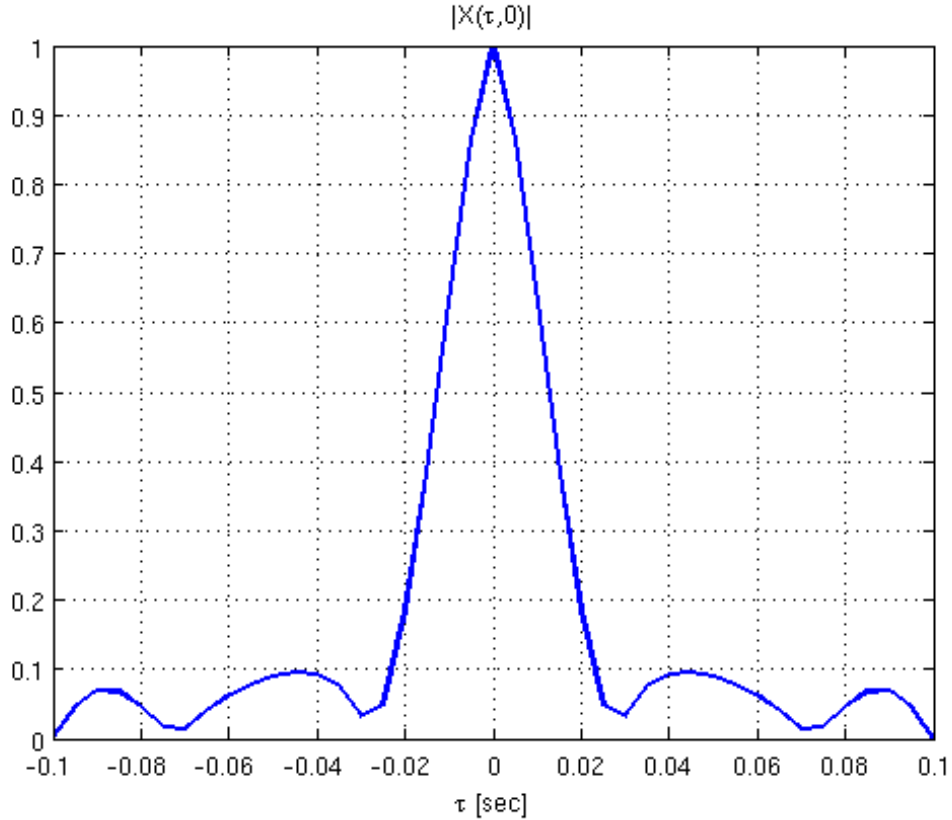


Figure 1.8 - Ambiguity function of a LFM pulse, zero-Doppler cut.

1.4 Ambiguity Function of a SFM pulse

In this Section we will derive the Complex Ambiguity Function (CAF) of the unitary energy Sinusoidal Frequency Modulated (SFM) pulse. This is a new contribution not present in the open literature. The SMP is defined as:

$$u(t) = \frac{1}{\sqrt{T}} e^{j\beta \sin(2\pi f_0 t + \varphi)} \text{rect}\left(\frac{t}{T}\right) \quad (1.16)$$

that is a pulse which instantaneous frequency¹ is a sinusoidal oscillation. In particular, T is the observation time, β is the modulation index and $1/f_0$ is the period of the instantaneous frequency.

¹ The instantaneous frequency is the derivative of the instantaneous phase divided by 2π . In eq. (1.16) the instantaneous phase is $\vartheta(t) = \beta \sin(2\pi f_0 t + \varphi)$, therefore the instantaneous frequency is $\zeta(t) = d\vartheta(t)/dt/2\pi = f_0 \beta \cos(2\pi f_0 t + \varphi)$. The peak frequency deviation is defined as $\Delta f = \max\{|\zeta(t)|\}$, in our case $\Delta f = \beta f_0$.

As will be clear in the following Chapter, for proper values of β and f_0 , this pulse can be used to approximate the signal transmitted by a FM commercial radio station in a PCL (Passive Coherent Location) system.

From eq. (1.2), it is easy to verify that the CAF of a generic pulse $x(t)$, can be considered as

$$X_x(\tau, \nu) = \int_{-\infty}^{+\infty} x(t)x^*(t-\tau)e^{-j2\pi\nu t} dt = FT\{x(t)x^*(t-\tau)\} \quad (1.17)$$

where $FT\{\cdot\}$ is the Fourier Transform operator.

In particular, if the signal $x(t)$ is the product of two signals

$$x(t) = x_1(t)x_2(t) \quad (1.18)$$

it is possible to write

$$\begin{aligned} X_x(\tau, \nu) &= FT\{x_1(t)x_2(t)x_1^*(t-\tau)x_2^*(t-\tau)\} = \\ &= FT\{x_1(t)x_1^*(t-\tau)\} \otimes FT\{x_2(t)x_2^*(t-\tau)\} = X_{x_1}(\tau, \nu) \otimes X_{x_2}(\tau, \nu) \end{aligned} \quad (1.19)$$

where \otimes is the convolution along the frequency domain ν .

In particular, the signal $u(t)$ in eq. (1.16) can be written as the product of the signals

$$y(t) = \frac{1}{\sqrt{T}} \text{rect}\left(\frac{t}{T}\right) \quad (1.20)$$

$$z(t) = e^{j\beta \sin(2\pi f_0 t + \phi)} \quad (1.21)$$

therefore, the CAF of $u(t)$ is given by the convolution along the frequency domain between the CAF of $y(t)$ and the CAF of $z(t)$.

After straightforward manipulation and using the results showed in Section 1.2, it is easy to verify that the CAF function of $y(t)$ is given by

$$X_y(\tau, \nu) = e^{-j\pi\nu\tau} \frac{\sin(\pi\nu(T-|\tau|))}{\pi\nu T} \text{rect}\left(\frac{\tau}{2T}\right) \quad (1.22)$$

The CAF of the $z(t)$ can be written as

$$X_z(\tau, \nu) = FT\{z(t)z^*(t-\tau)\} = FT\{z(t)\} \otimes FT\{z^*(t-\tau)\} = Z(\nu) \otimes e^{-j2\pi\nu\tau} Z^*(-\nu) \quad (1.23)$$

where

$$Z(\nu) = \int_{-\infty}^{+\infty} z(t)e^{-j2\pi\nu t} dt = \int_{-\infty}^{+\infty} e^{j\beta\sin(2\pi f_0 t + \varphi)} e^{-j2\pi\nu t} dt \quad (1.24)$$

is the Fourier Transform of $z(t)$.

It apparent that $z(t)$ is a $1/f_0$ -periodic signal, therefore its Fourier Transform is given by

$$Z(\nu) = \sum_n Z_n \delta(\nu - nf_0) \quad (1.25)$$

where $\delta(\cdot)$ is the Dirac Delta function and Z_n are the Fourier coefficients given by

$$Z_n = f_0 \int_{-1/2f_0}^{1/2f_0} e^{j\beta\sin(2\pi f_0 t + \varphi)} e^{-j2\pi n f_0 t} dt = \frac{e^{jn\varphi}}{2\pi} \int_{-\pi}^{\pi} e^{j(\beta\sin(\alpha) - n\alpha)} d\alpha = e^{jn\varphi} J_n(\beta) \quad (1.26)$$

and $J_n(\beta)$ is the Bessel function of the first kind and order n .

Therefore, it is possible to write²

$$Z(\nu) = \sum_n e^{jn\varphi} J_n(\beta) \delta(\nu - nf_0) \quad (1.27)$$

$$z(t) = \sum_n e^{jn\varphi} J_n(\beta) e^{j2\pi n f_0 t} \quad (1.28)$$

Carrying out the convolution along ν , as in eq. (1.23), it is easy to verify that

$$X_z(\tau, \nu) = \sum_n \sum_k a_{n,k} e^{+j2\pi k f_0 \tau} \delta(\nu - (n-k) f_0) \quad (1.29)$$

where

$$a_{n,k} = e^{j(n-k)\varphi} J_n(\beta) J_k(\beta) \quad (1.30)$$

² The signal $z(t)$ could be approximated by considering only the elements from $-N$ to N in the infinite sums in (1.13) and cutting off all the other elements. Choosing $N = \text{int}(\beta + 1)$, the power of the approximated signal is 98% of the power of $z(t)$.

Using eq. (1.19), we have

$$X_u(\tau, \nu) = \sum_n \sum_k a_{n,k} e^{+j2\pi k f_0 \tau} X_y(\tau, \nu - (n-k)f_0) \quad (1.31)$$

that is

$$X_u(\tau, \nu) = \sum_n \sum_k e^{j(n-k)\varphi} J_n(\beta) J_k(\beta) e^{+j2\pi k f_0 \tau} e^{-j\pi(\nu - (n-k)f_0)\tau} \frac{\sin(\pi(\nu - (n-k)f_0)(T - |\tau|))}{\pi(\nu - (n-k)f_0)T} \text{rect}\left(\frac{\tau}{2T}\right) \quad (1.32)$$

Figures 9-40 show the absolute value of the CAF for different values of T , φ and β . All the results have been obtained setting $f_0=15\text{kHz}$ ³ and choosing $T=k/f_0$. Figures are divided into eight cases, each of which is composed by four figures.

Figure 9-12 show the AF obtained setting $k=1$ and $\beta=0$. In this case the analyzed pulse is a unitary energy rectangular pulse of time duration $1/f_0=0.0667\text{msec}$. In this case the CAF is the same as that obtained for a rectangular pulse. Figure 13-15 shows the AF obtained setting $k=1$, $\beta=5$ and $\varphi= \pi/2$. The obtained AF is a distorted and rotated version of the AF of a rectangular pulse. Observing the results in Figures 16-40, it is apparent that increasing the value of k the 0-Doppler cut is characterized by the presence of secondary lobes. Considering $k \in \mathbb{N}$, the number of secondary lobes is $2(k-1)$. The presence of secondary lobes is due to the periodicity of the analyzed pulse. Moreover, for $k>1$, the AF has a T -periodic behaviour along the delay axis. Moreover, it is apparent that the value of β influences the Doppler spread of the AF, while by modifying the value of φ , the AF rotates.

As previously shown, the 0-Delay cut is the absolute value of the Fourier transform of the squared amplitude of the analyzed pulse. The squared amplitude of the analyzed pulse is a rectangular pulse of time duration T , therefore, the 0-Delay cut is always the absolute value of a *sinc* function.

³ As will be clear in next Chapter, if we are interested in modelling the signal emitted by a FM commercial radio station f_0 must belong to the range of audible frequencies (i.e. [20Hz, 20kHz]).

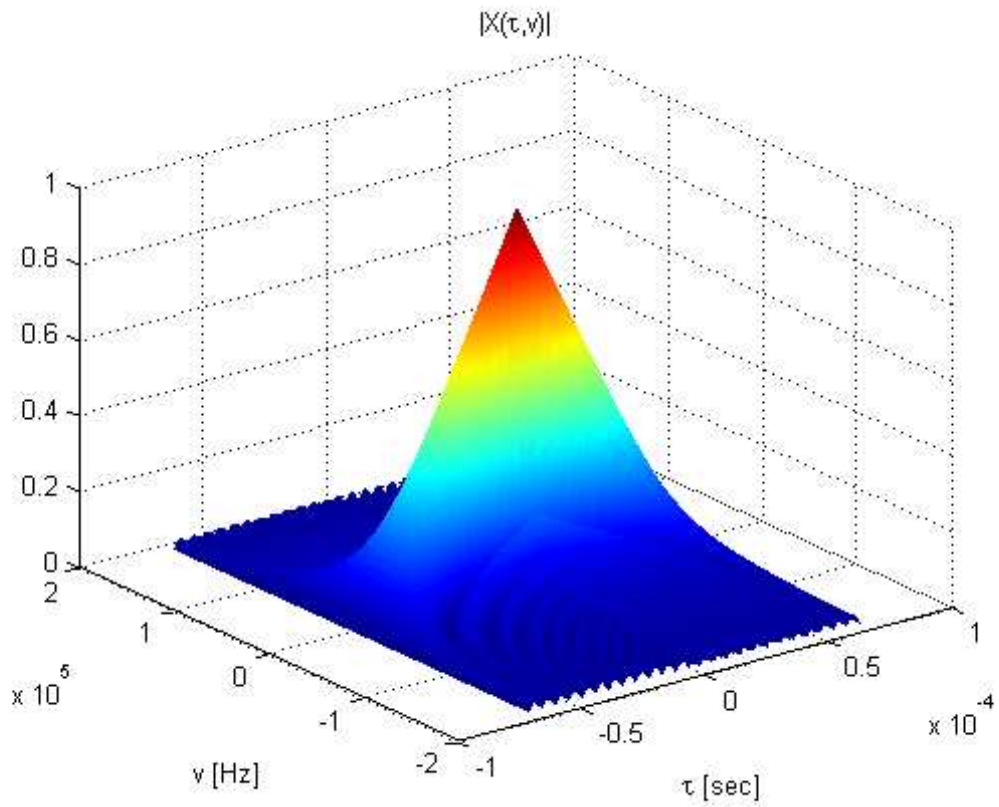


Figure 1.9 – AF of SFM pulse, 3D-graph. $T=1/f_0, f_0=15\text{kHz}, \beta=0, \varphi=\pi/2$

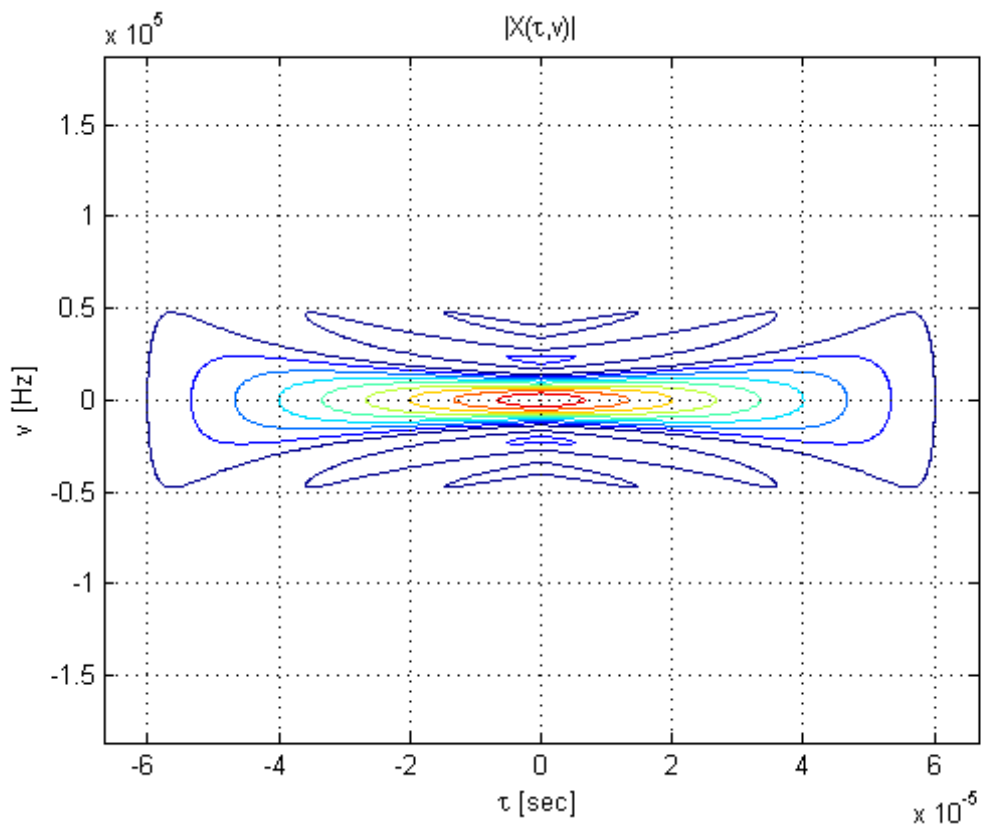


Figure 1.10 - AF of SFM pulse, contour-plot. $T=1/f_0, f_0=15\text{kHz}, \beta=0, \varphi=\pi/2$

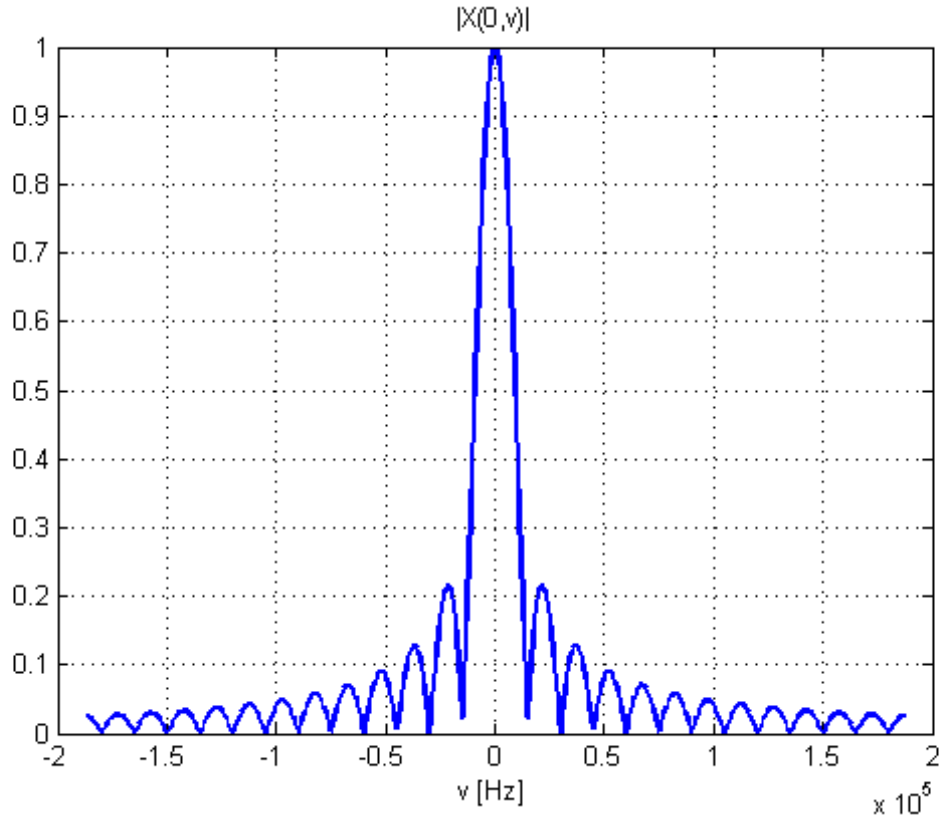


Figure 1.11 - AF of SFM pulse, 0-Delay Cut. $T=1/f_0$, $f_0=15\text{kHz}$, $\beta=0$, $\varphi=\pi/2$

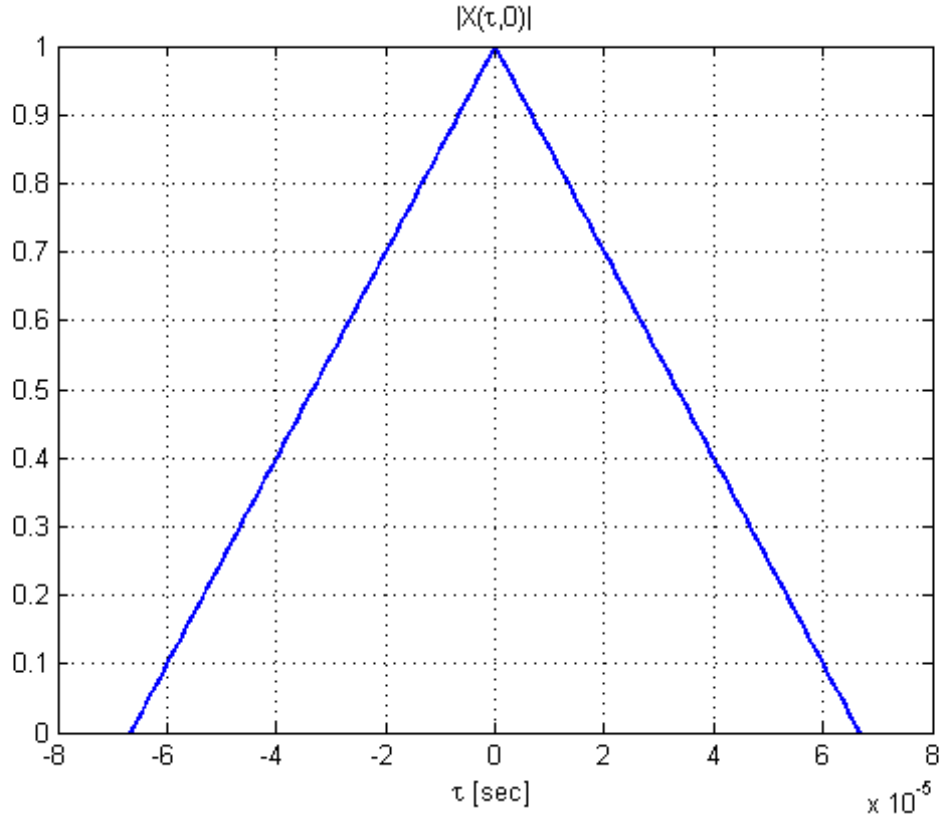


Figure 1.12 - AF of SFM pulse, 0-Doppler Cut. $T=1/f_0$, $f_0=15\text{kHz}$, $\beta=0$, $\varphi=\pi/2$

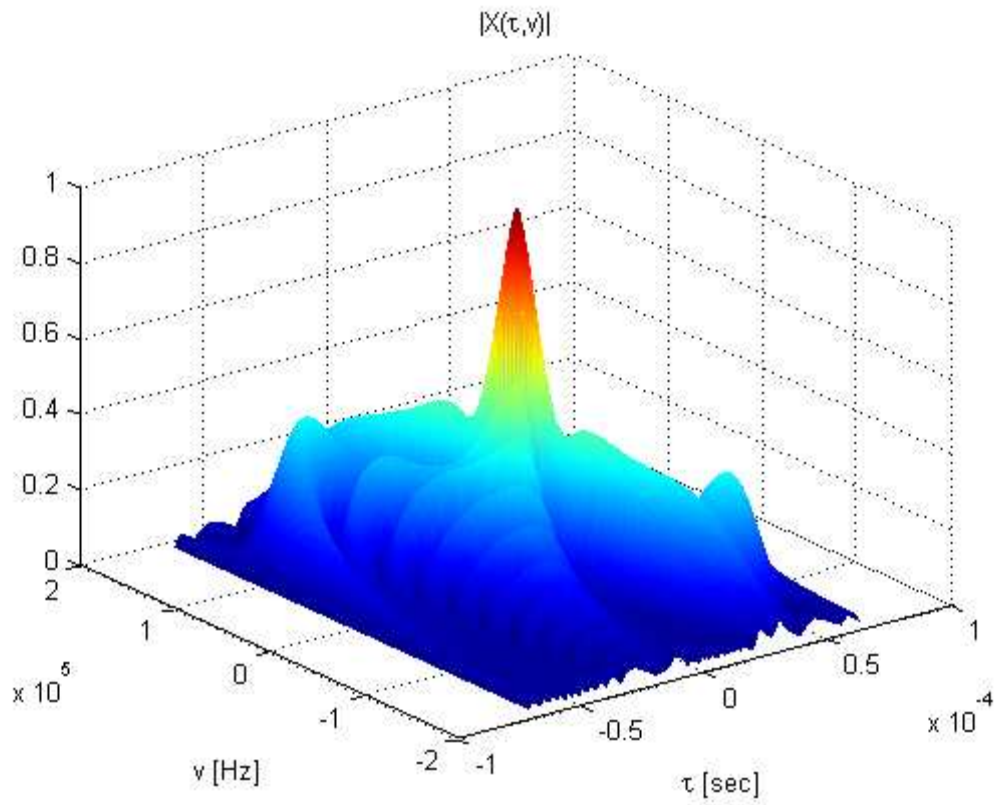


Figure 1.13 - AF of SFM pulse, 3D-graph. $T=1/f_0, f_0=15\text{kHz}, \beta=5, \varphi=\pi/2$

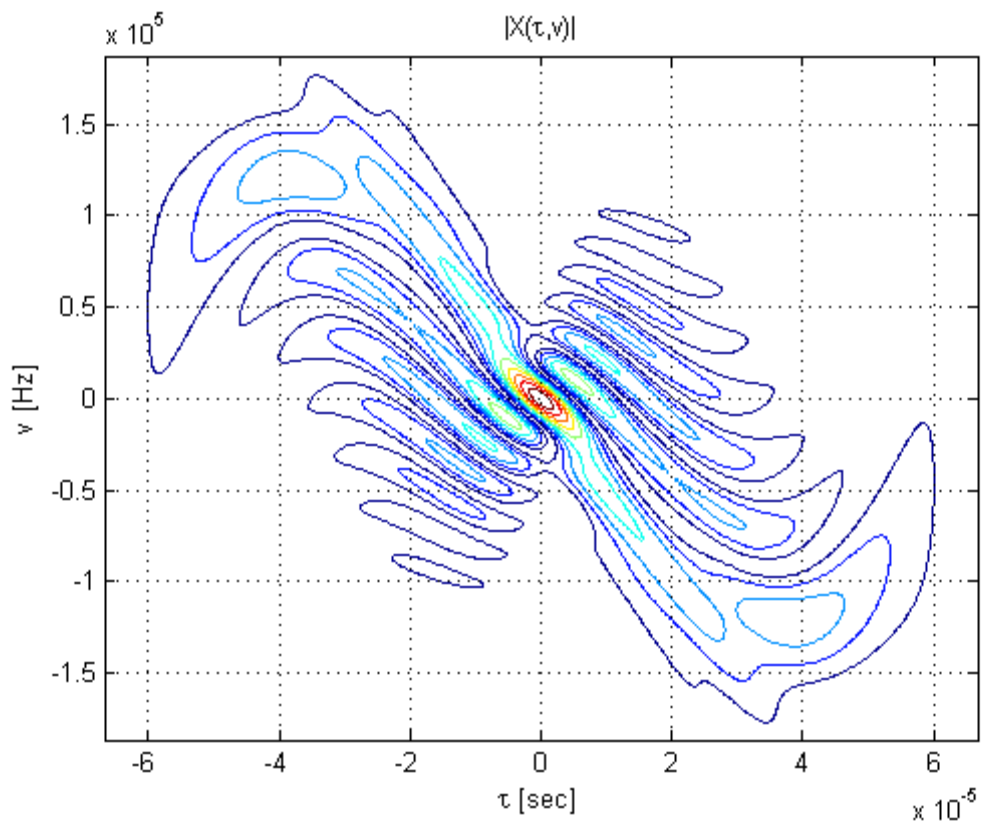


Figure 1.14 - AF of SFM pulse, contour-plot. $T=1/f_0, f_0=15\text{kHz}, \beta=5, \varphi=\pi/2$

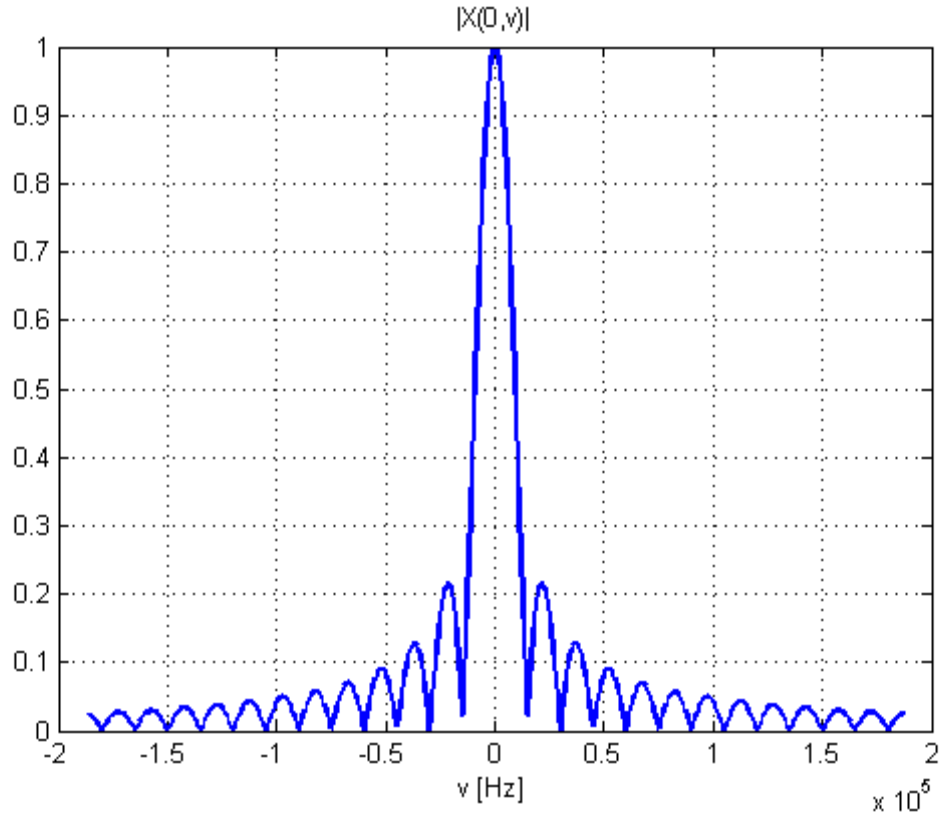


Figure 1.15 - AF of SFM pulse, 0-Delay Cut. $T=1/f_0$, $f_0=15\text{kHz}$, $\beta=5$, $\varphi=\pi/2$

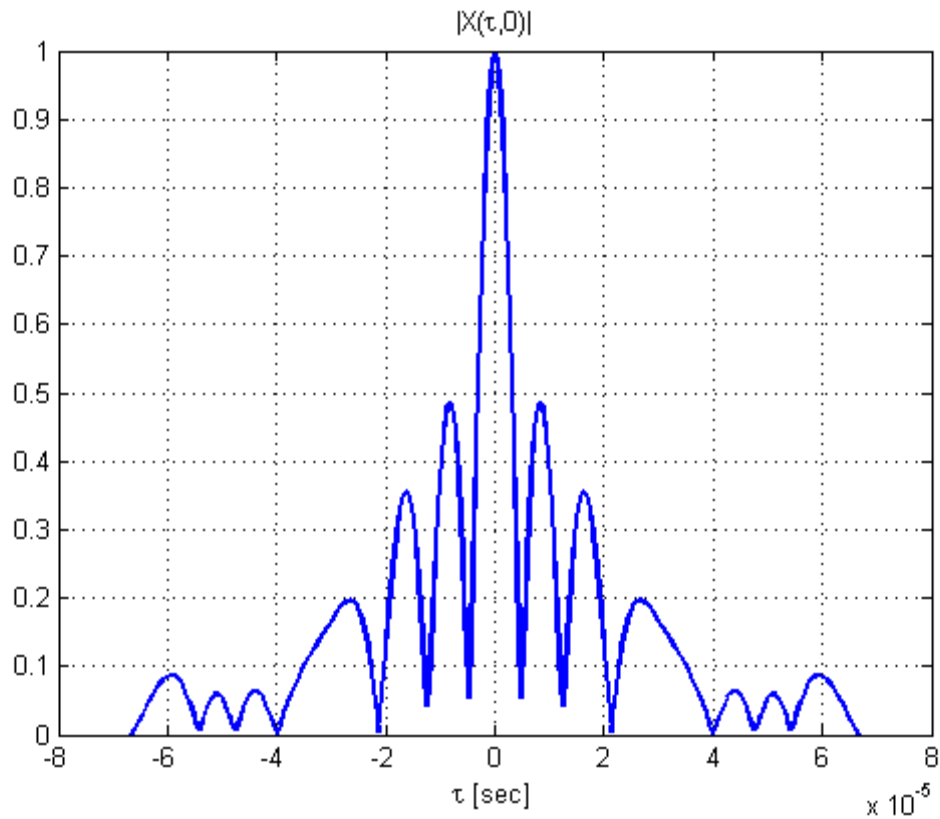


Figure 1.16 - AF of SFM pulse, 0-Doppler Cut. $T=1/f_0$, $f_0=15\text{kHz}$, $\beta=5$, $\varphi=\pi/2$

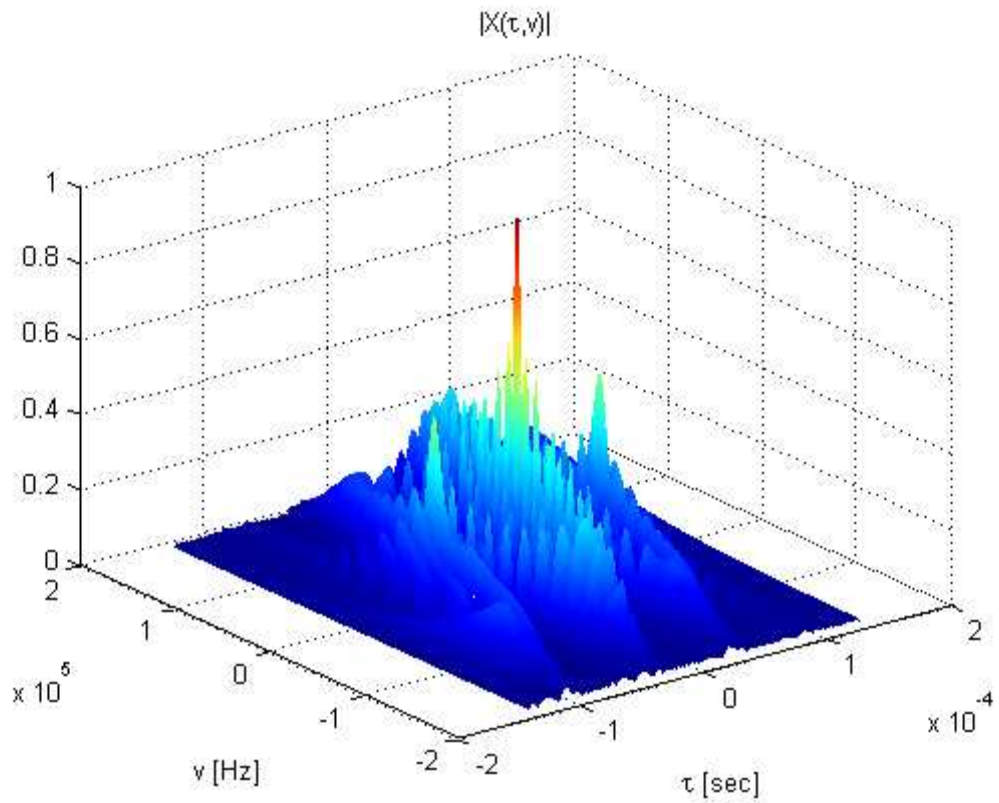


Figure 1.17 - AF of SFM pulse, 3D-graph. $T=2/f_0$, $f_0=15\text{kHz}$, $\beta=5$, $\varphi=\pi/2$

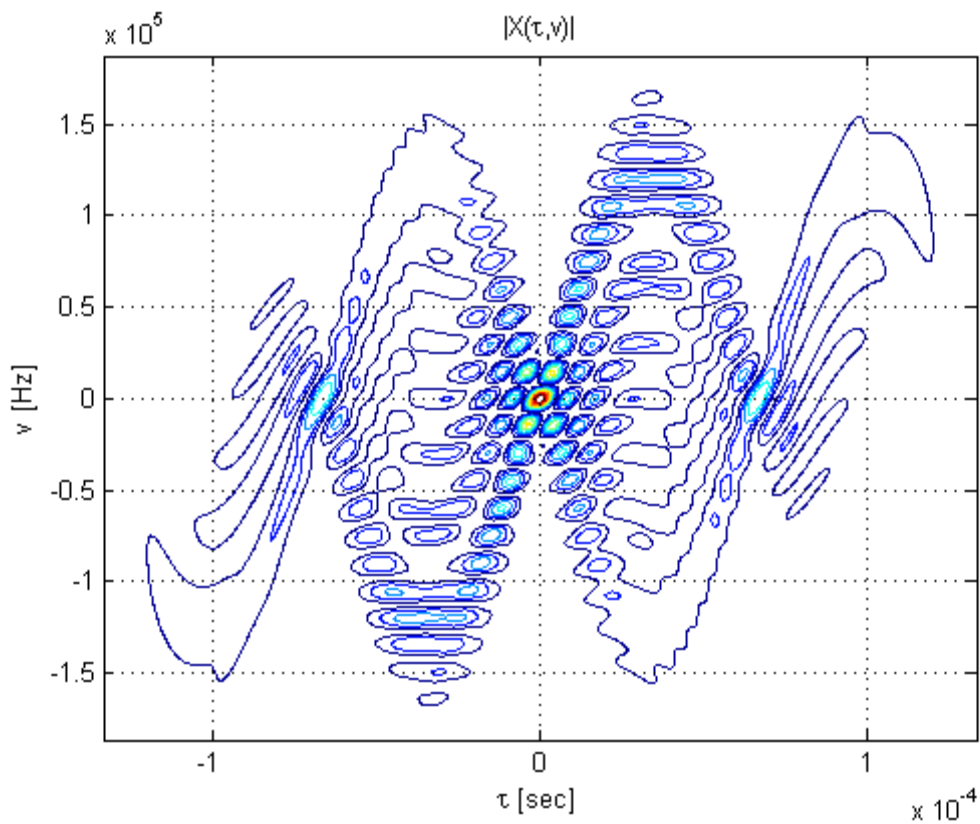


Figure 1.18 - AF of SFM pulse, contour-plot. $T=2/f_0$, $f_0=15\text{kHz}$, $\beta=5$, $\varphi=\pi/2$

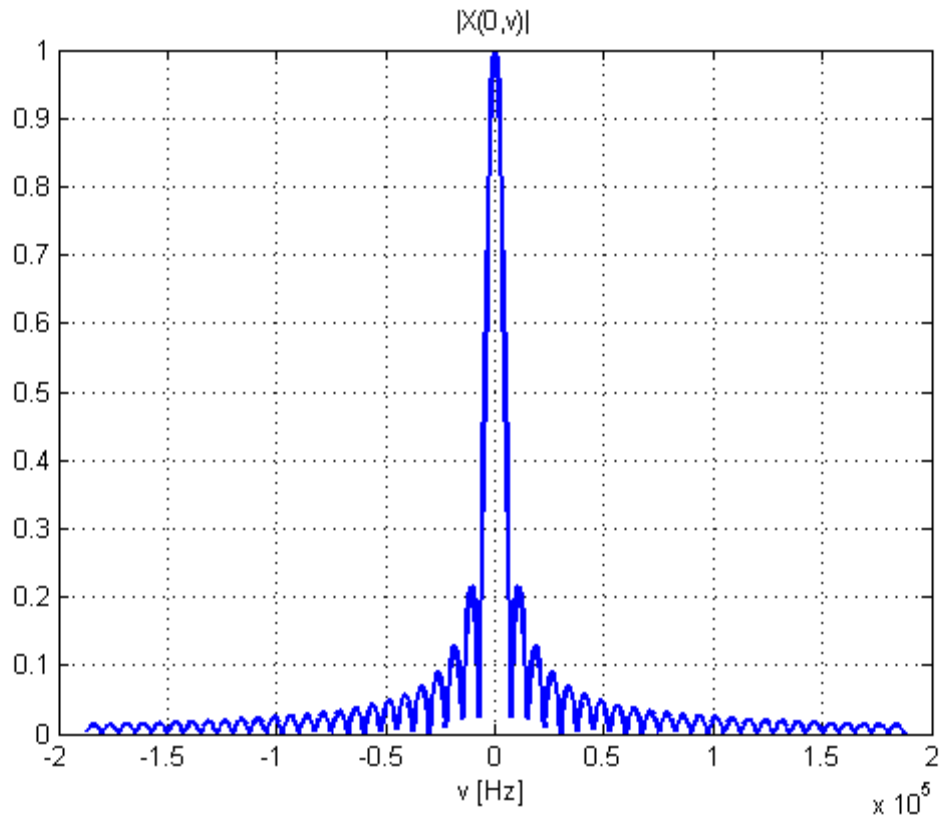


Figure 1.19 - AF of SFM pulse, 0-Delay Cut. $T=2/f_0$, $f_0=15\text{kHz}$, $\beta=5$, $\varphi=\pi/2$

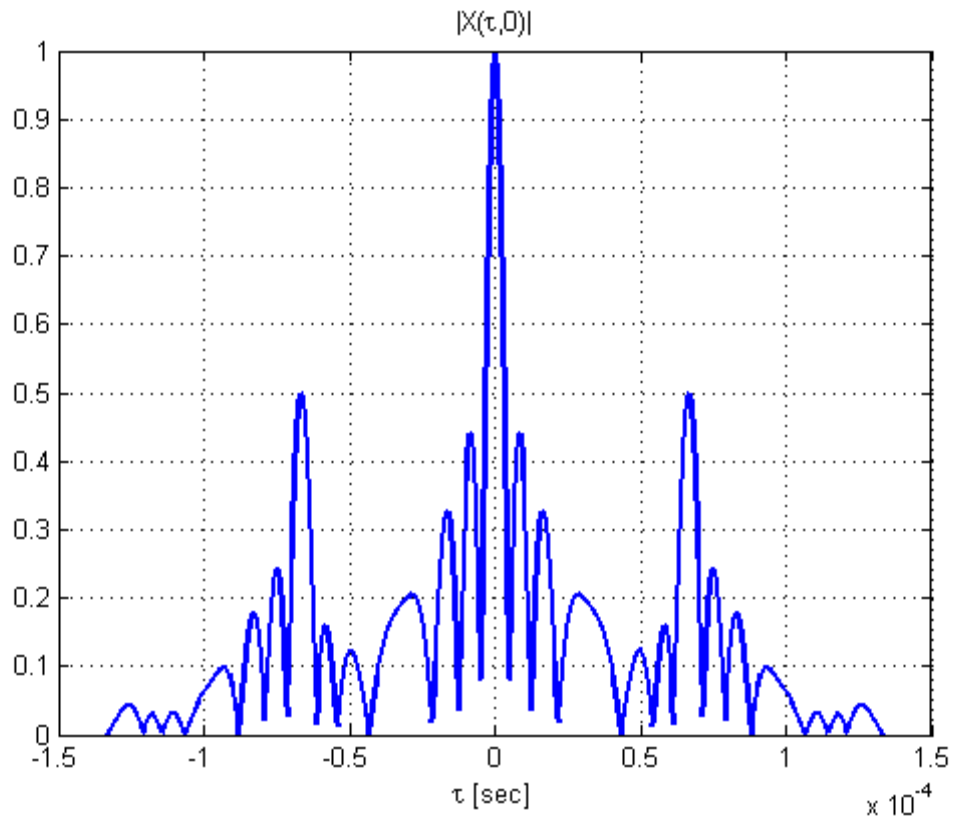


Figure 1.20 - AF of SFM pulse, 0-Doppler Cut. $T=2/f_0$, $f_0=15\text{kHz}$, $\beta=5$, $\varphi=\pi/2$

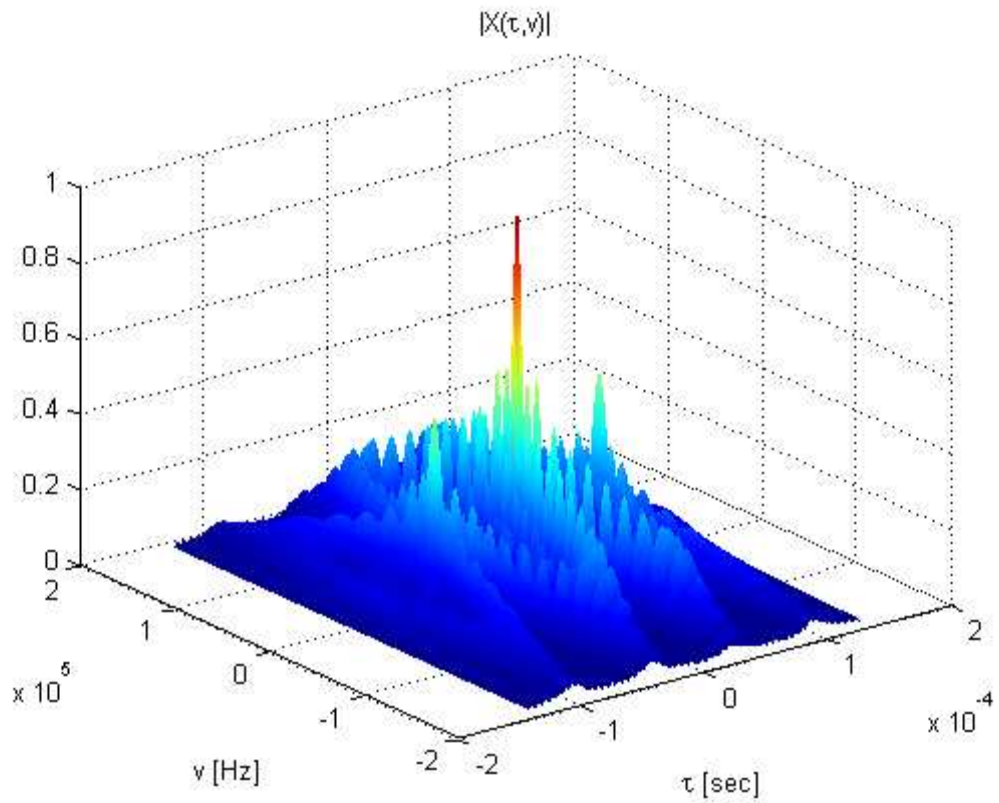


Figure 1.21 - AF of SFM pulse, 3D-graph. $T=2/f_0, f_0=15\text{kHz}, \beta=5, \varphi=0$ ($\varphi=\pi$)

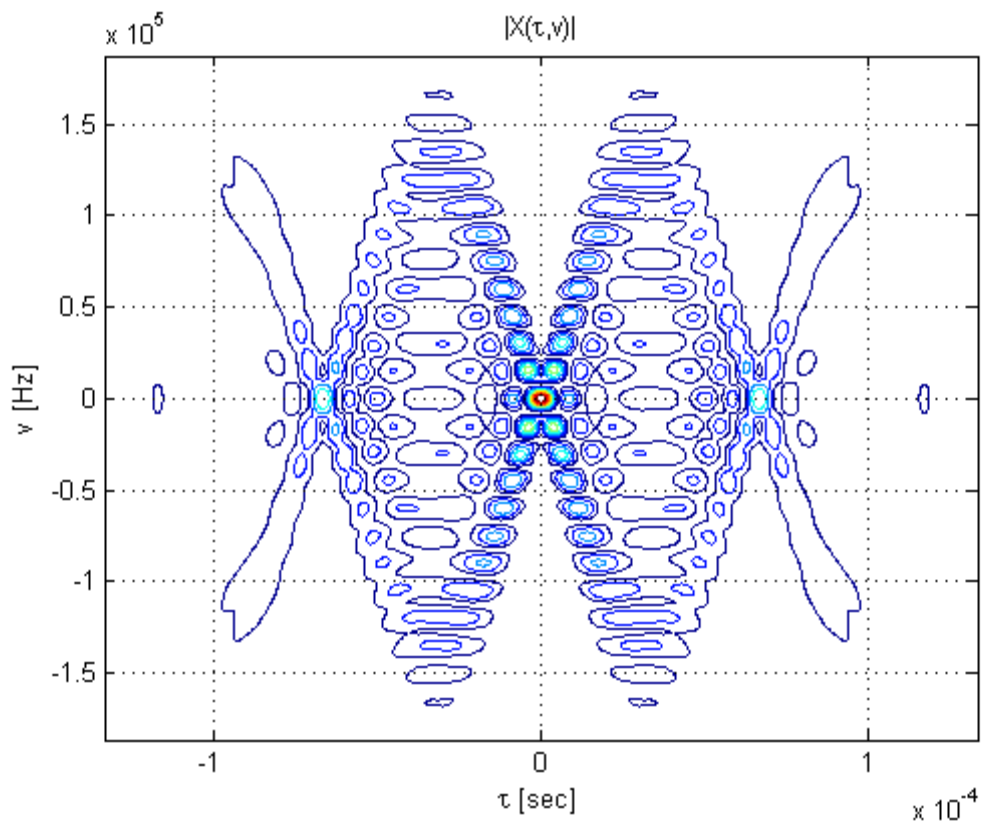


Figure 1.22 - AF of SFM pulse, contour-plot. $T=2/f_0, f_0=15\text{kHz}, \beta=5, \varphi=0$ ($\varphi=\pi$)

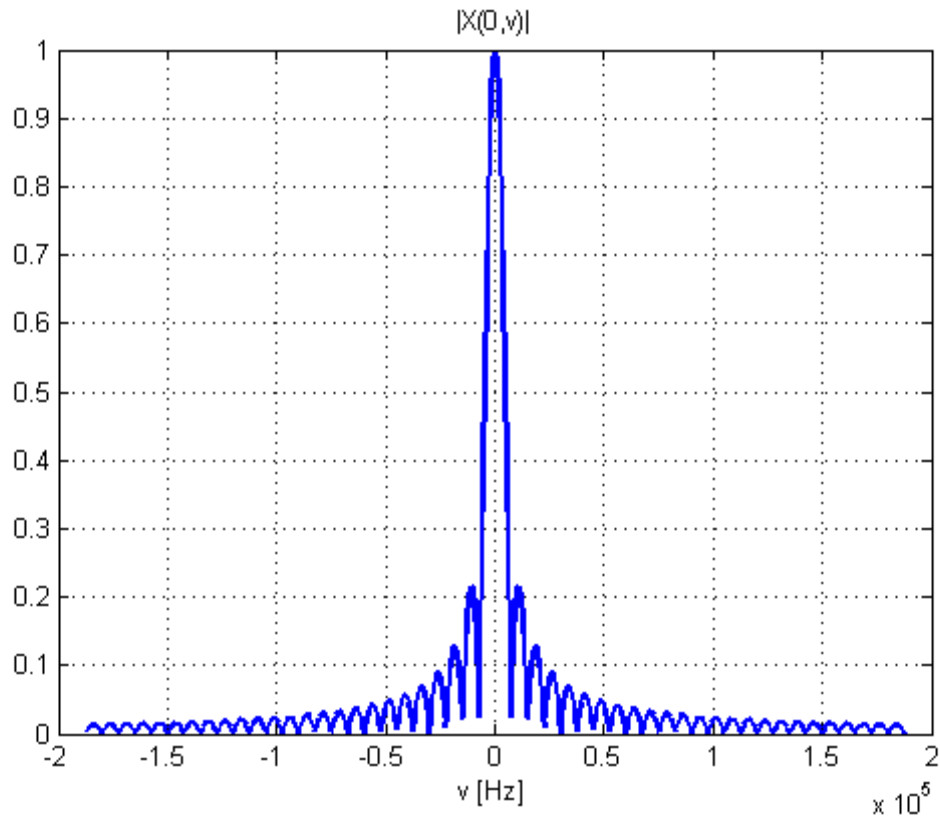


Figure 1.23 - AF of SFM pulse, 0-Delay Cut. $T=2/f_0$, $f_0=15\text{kHz}$, $\beta=5$, $\varphi=0$ ($\varphi=\pi$)

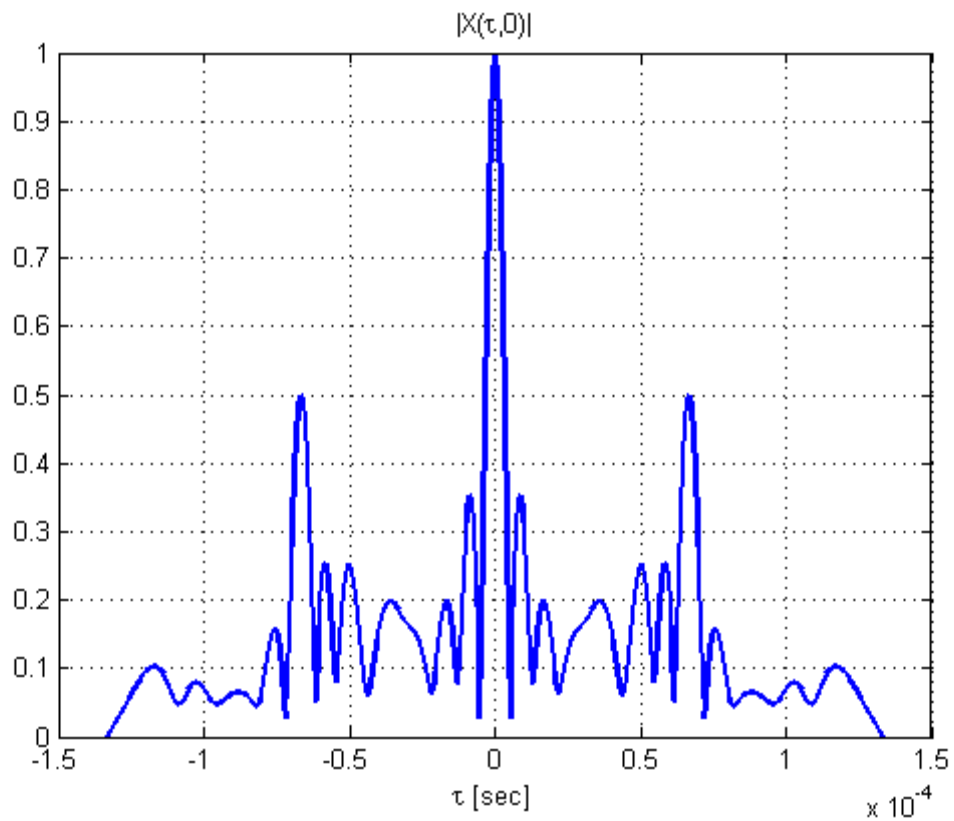


Figure 1.24 - AF of SFM pulse, 0-Doppler Cut. $T=2/f_0$, $f_0=15\text{kHz}$, $\beta=5$, $\varphi=0$ ($\varphi=\pi$)



Figure 1.25 - AF of SFM pulse, 3D-graph. $T=2/f_0$, $f_0=15\text{kHz}$, $\beta=5$, $\varphi=-\pi/2$

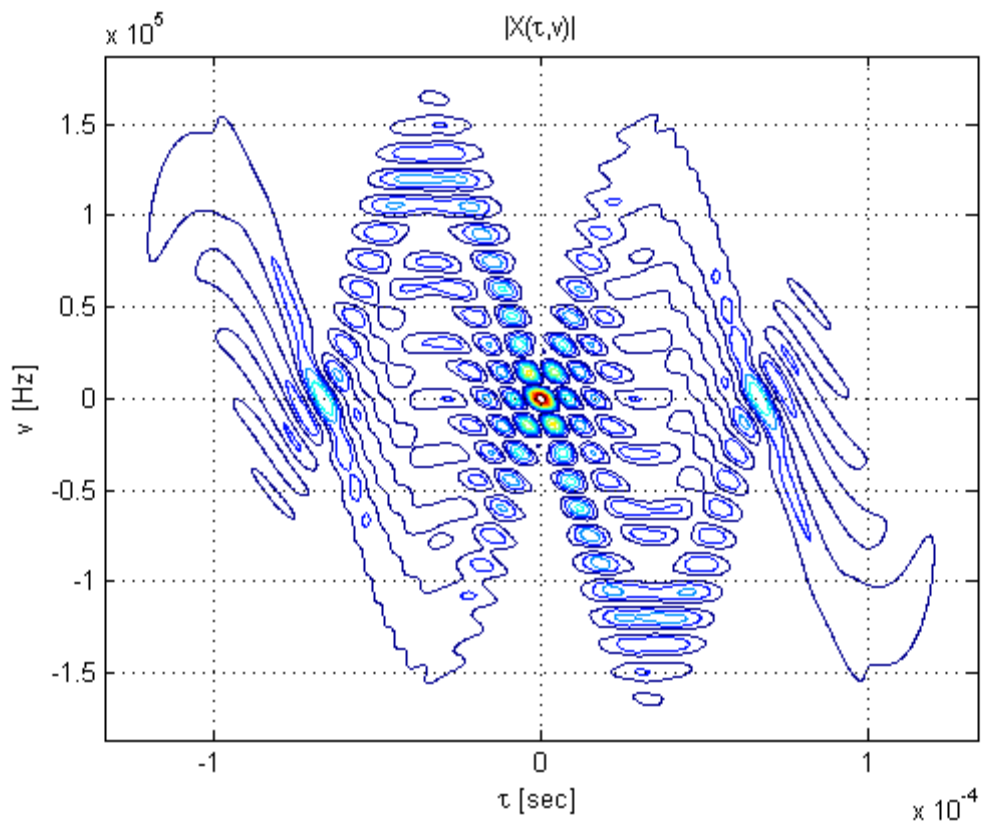


Figure 1.26 - AF of SFM pulse, contour-plot. $T=2/f_0$, $f_0=15\text{kHz}$, $\beta=5$, $\varphi=-\pi/2$

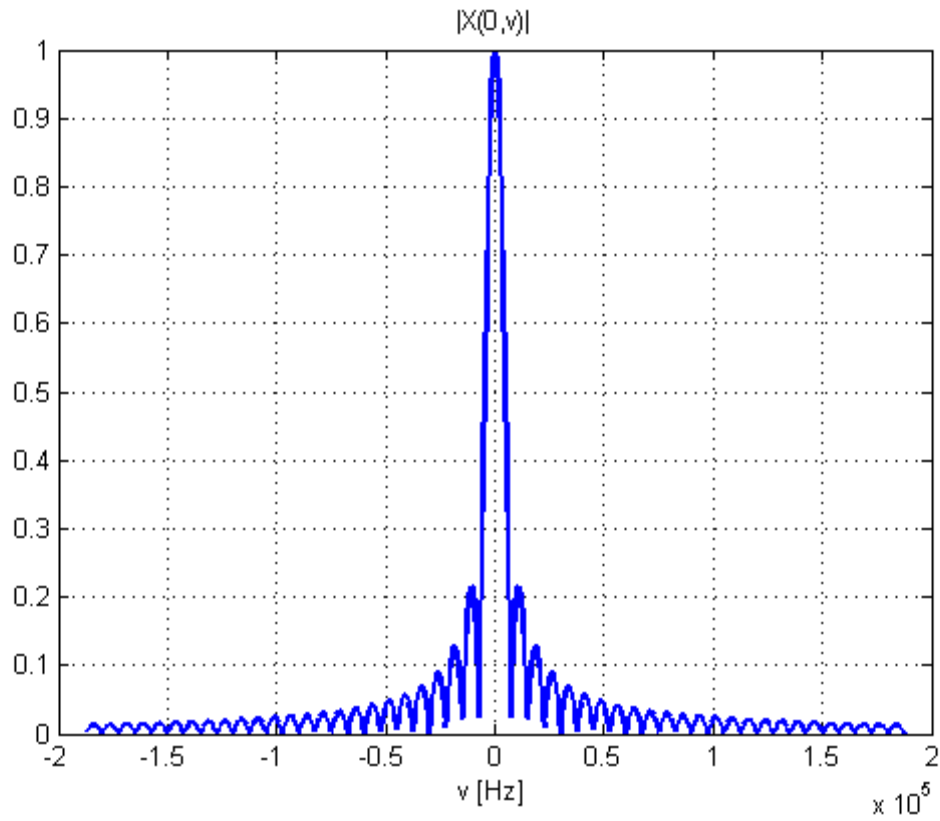


Figure 1.27 - AF of SFM pulse, 0-Delay Cut. $T=2/f_0$, $f_0=15\text{kHz}$, $\beta=5$, $\varphi=-\pi/2$

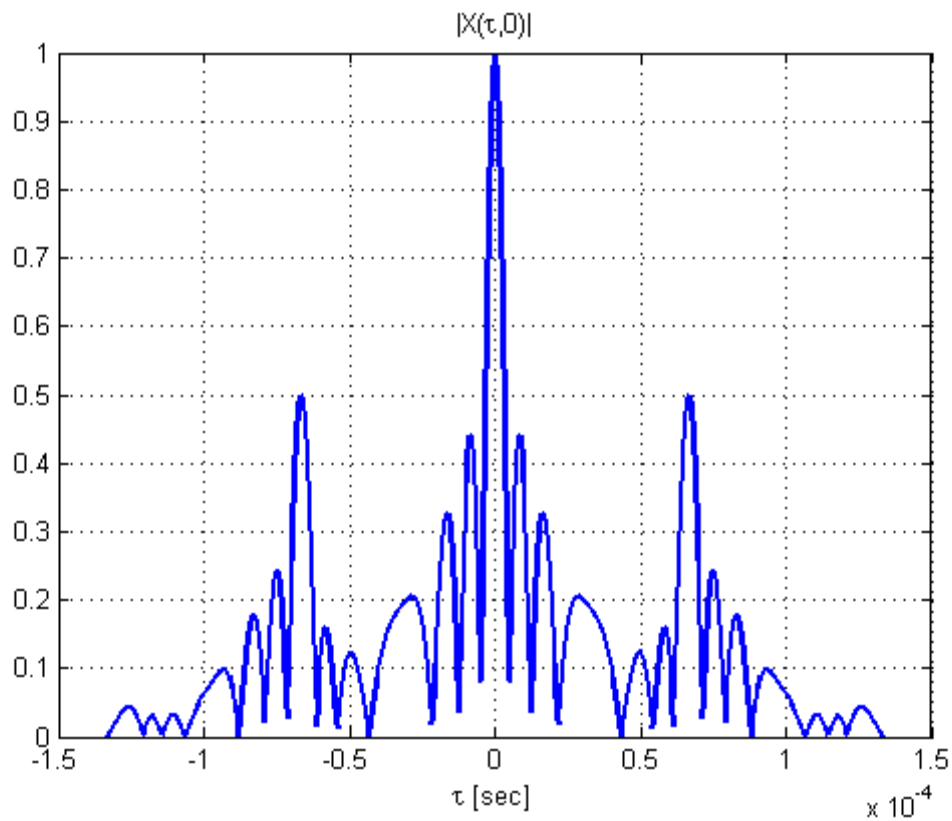


Figure 1.28 - AF of SFM pulse, 0-Doppler Cut. $T=2/f_0$, $f_0=15\text{kHz}$, $\beta=5$, $\varphi=-\pi/2$

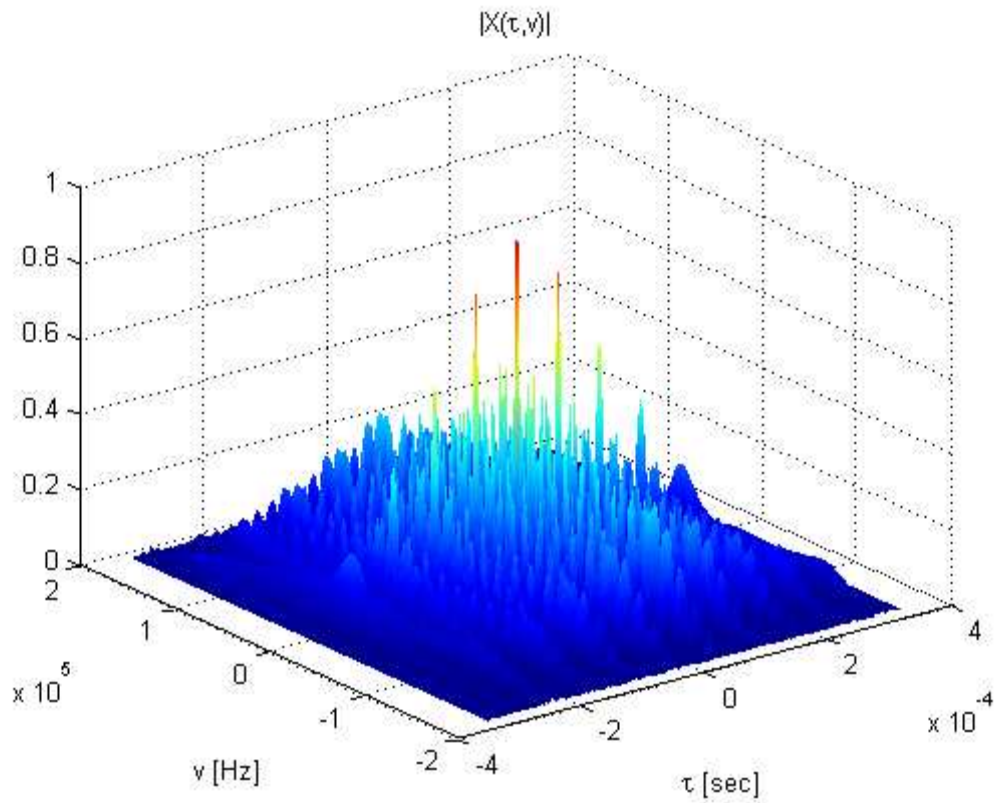


Figure 1.29 - AF of SFM pulse, 3D-graph. $T=5/f_0$, $f_0=15\text{kHz}$, $\beta=5$, $\varphi=\pi/2$

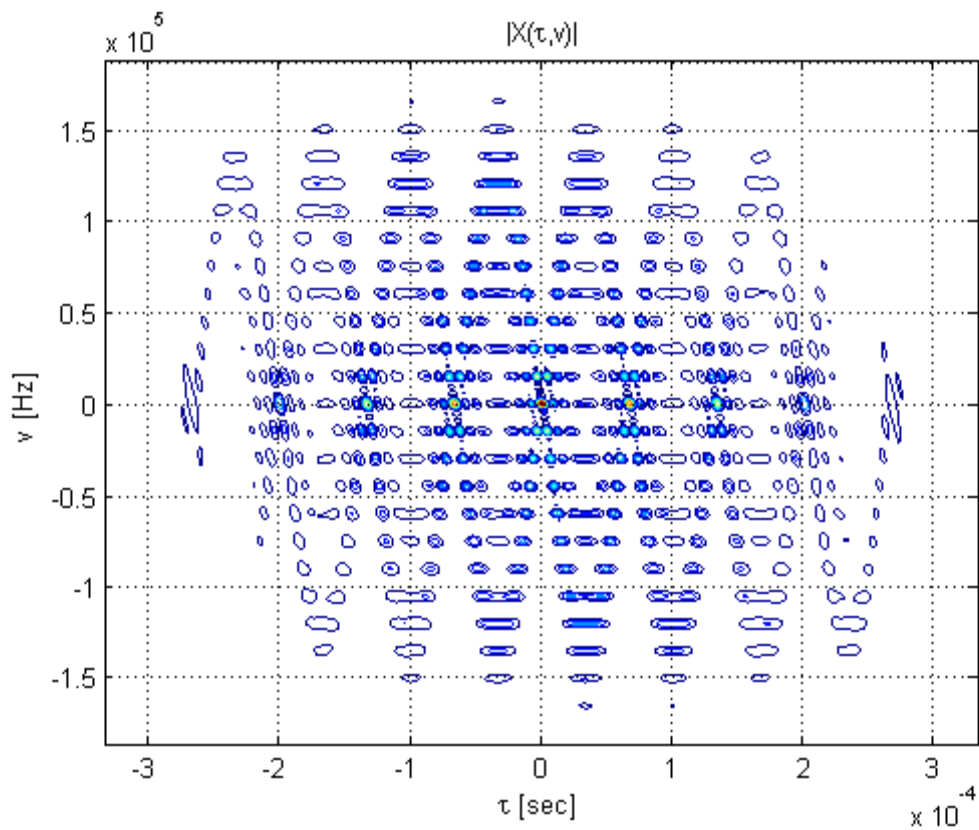


Figure 1.30 - AF of SFM pulse, contour-plot. $T=5/f_0$, $f_0=15\text{kHz}$, $\beta=5$, $\varphi=\pi/2$

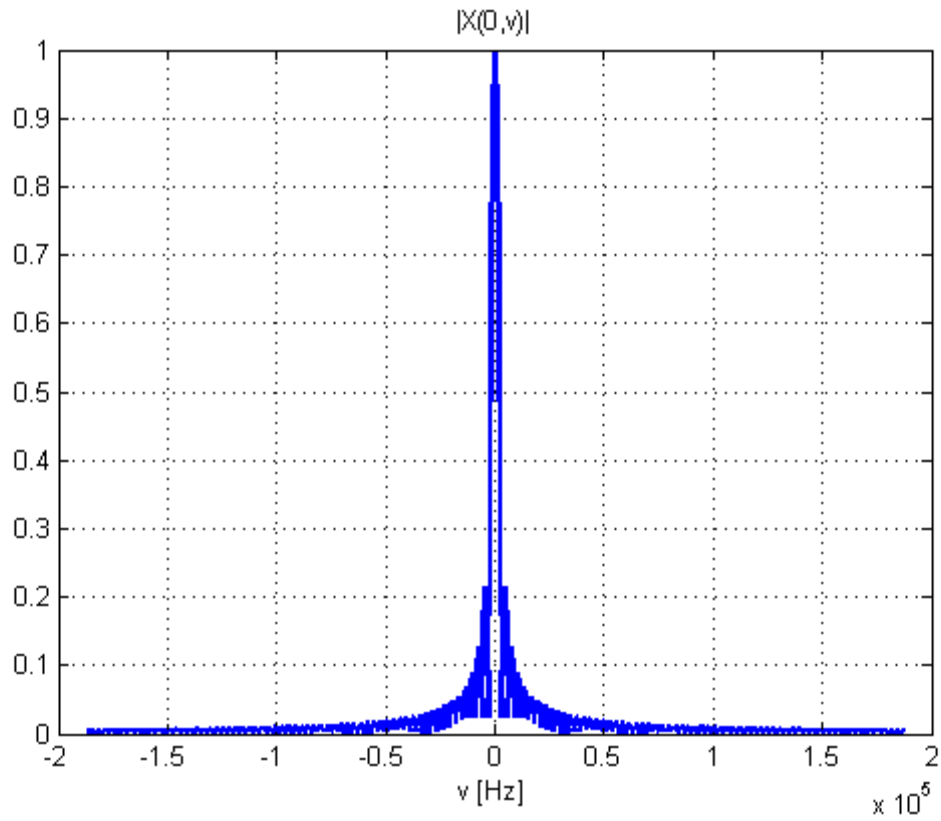


Figure 1.31 - AF of SFM pulse, 0-Delay Cut. $T=5/f_0$, $f_0=15\text{kHz}$, $\beta=5$, $\varphi=\pi/2$

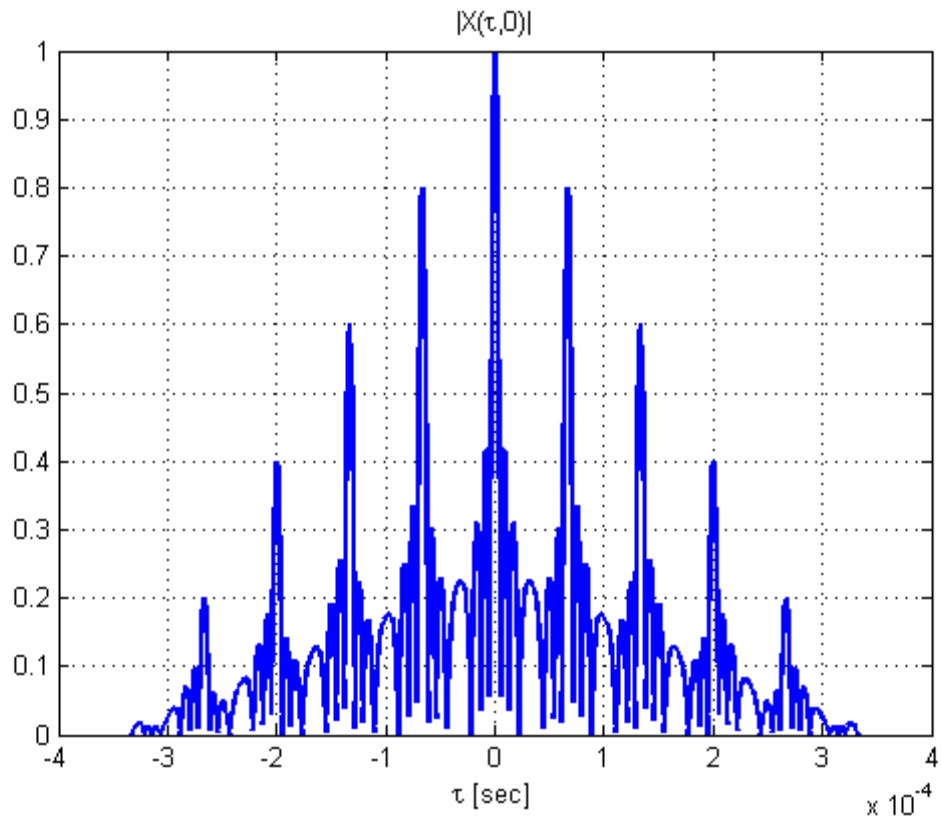


Figure 1.32 - AF of SFM pulse, 0-Doppler Cut. $T=5/f_0$, $f_0=15\text{kHz}$, $\beta=5$, $\varphi=\pi/2$

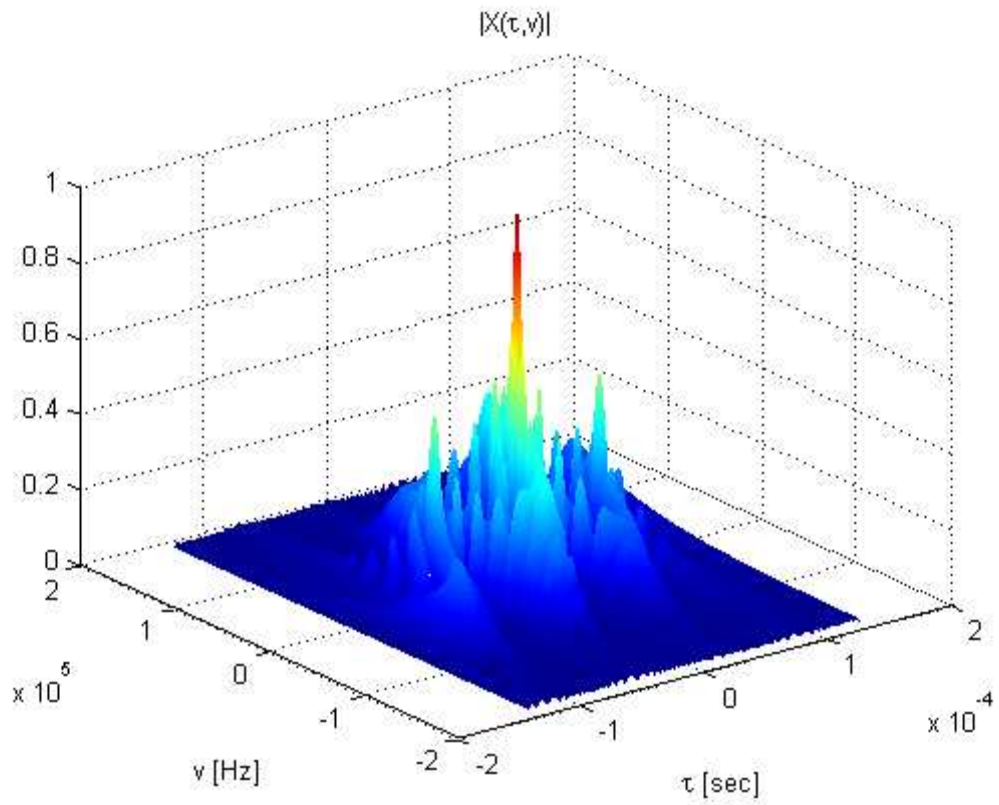


Figure 1.33 - AF of SFM pulse, 3D-graph. $T=2/f_0$, $f_0=15\text{kHz}$, $\beta=3$, $\varphi=\pi/2$

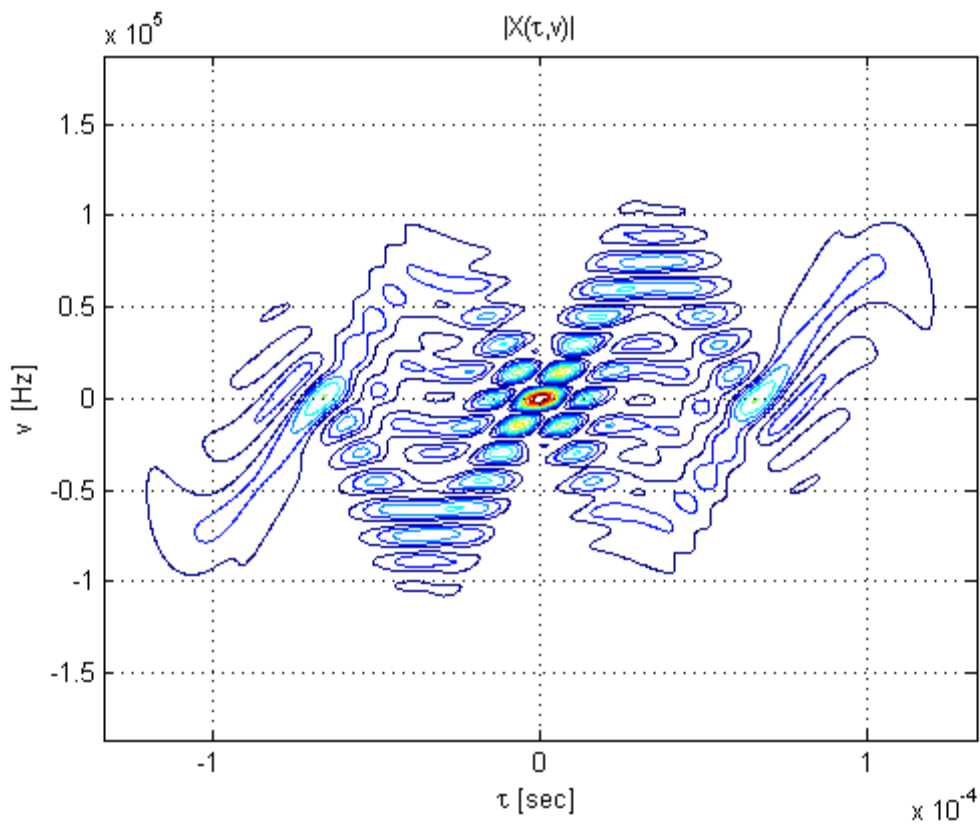


Figure 1.34 - AF of SFM pulse, contour-plot. $T=2/f_0$, $f_0=15\text{kHz}$, $\beta=3$, $\varphi=\pi/2$

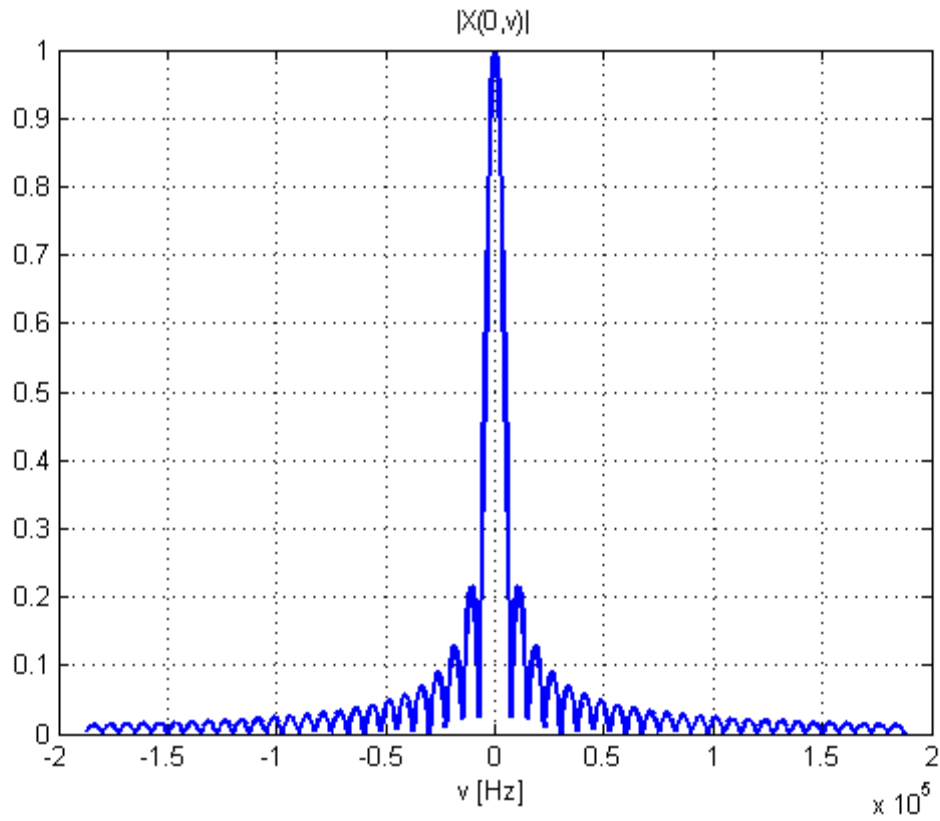


Figure 1.35 - AF of SFM pulse, 0-Delay Cut. $T=2/f_0$, $f_0=15\text{kHz}$, $\beta=3$, $\varphi=\pi/2$

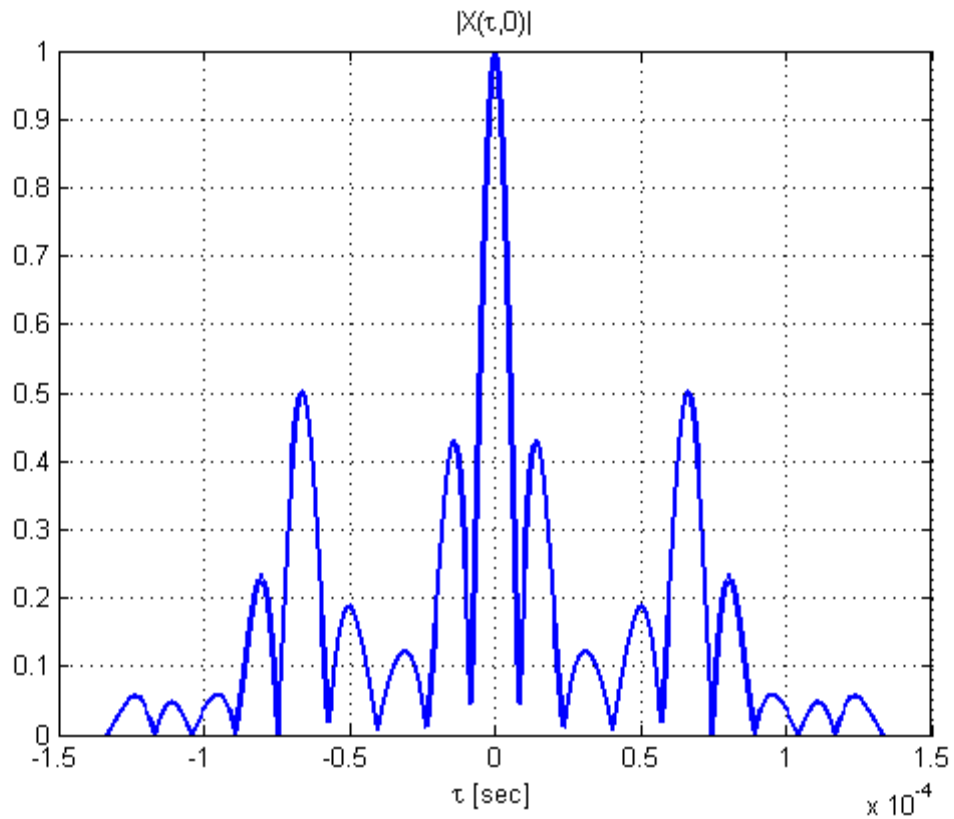


Figure 1.36 - AF of SFM pulse, 0-Doppler Cut. $T=2/f_0$, $f_0=15\text{kHz}$, $\beta=3$, $\varphi=\pi/2$

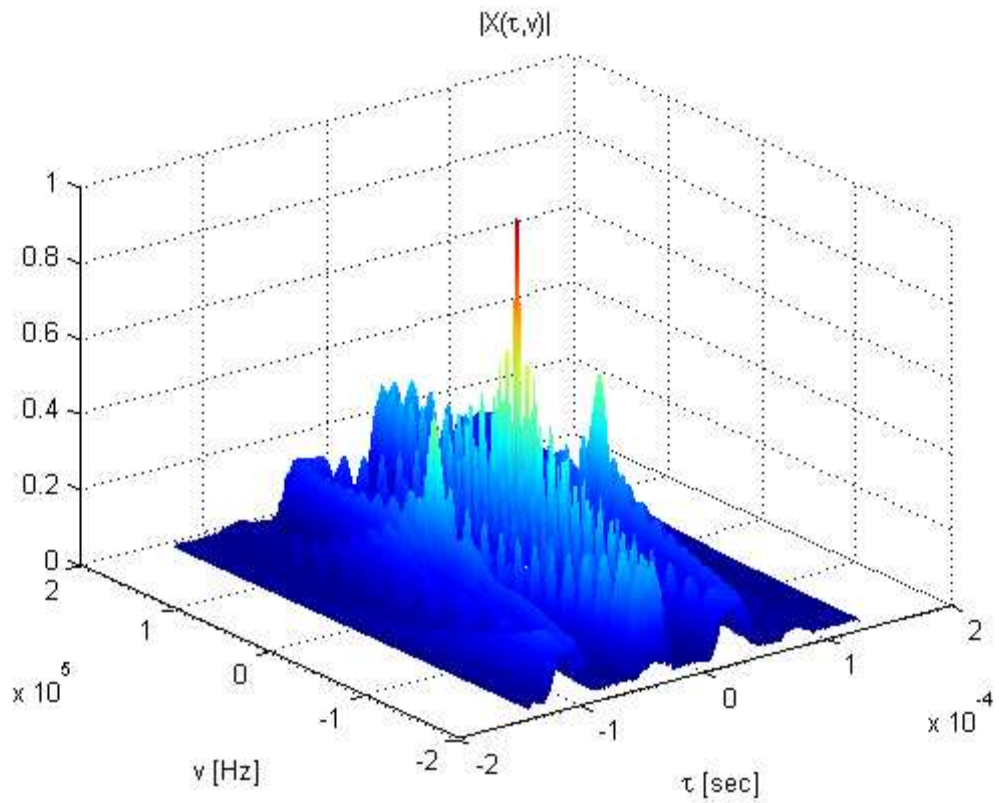


Figure 1.37 - AF of SFM pulse, 3D-graph. $T=2/f_0$, $f_0=15\text{kHz}$, $\beta=7$, $\varphi=\pi/2$

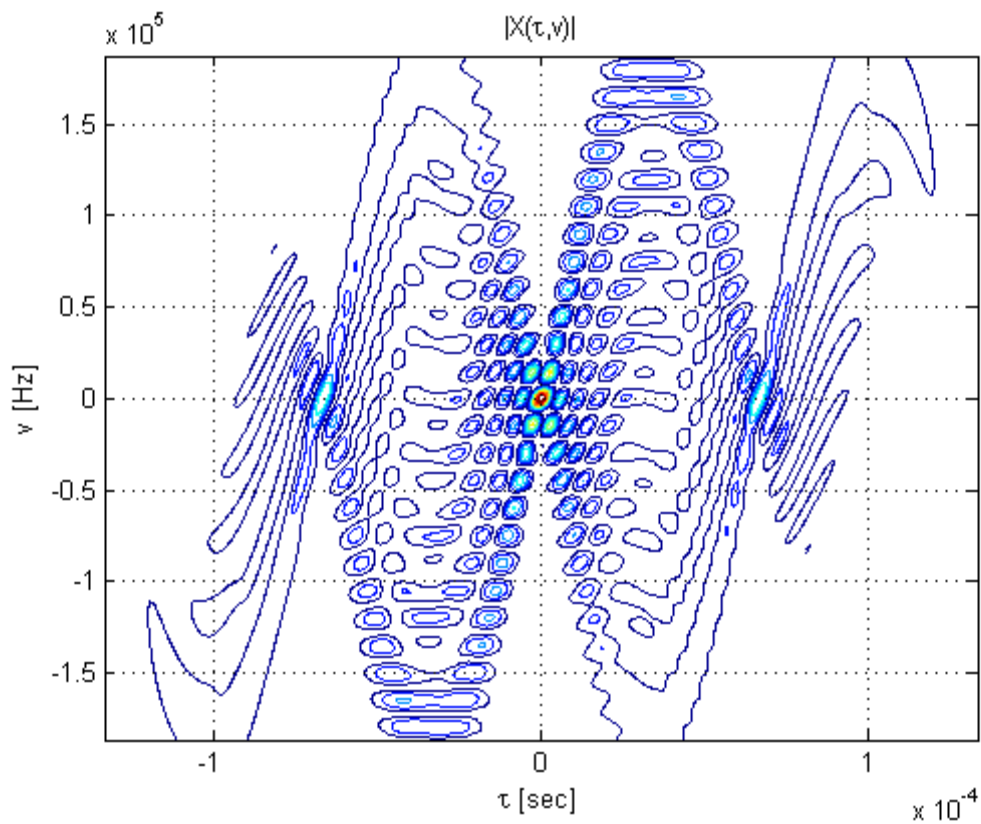


Figure 1.38 - AF of SFM pulse, contour-plot. $T=2/f_0$, $f_0=15\text{kHz}$, $\beta=7$, $\varphi=\pi/2$

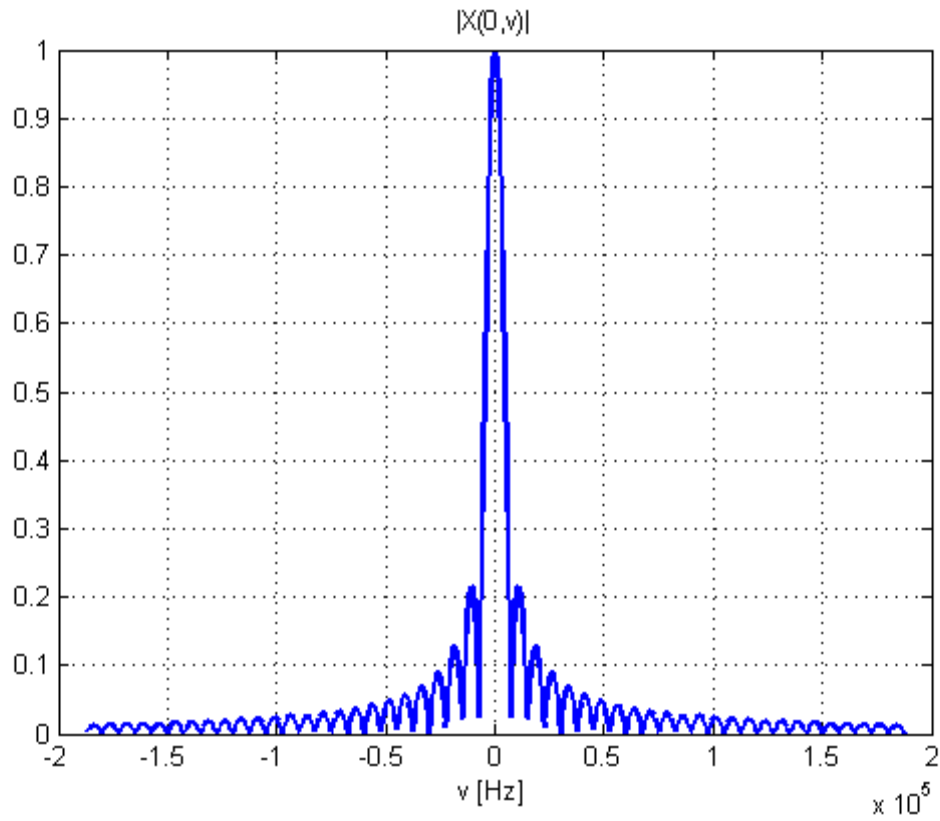


Figure 1.39 - AF of SFM pulse, 0-Delay Cut. $T=2/f_0$, $f_0=15\text{kHz}$, $\beta=7$, $\varphi=\pi/2$

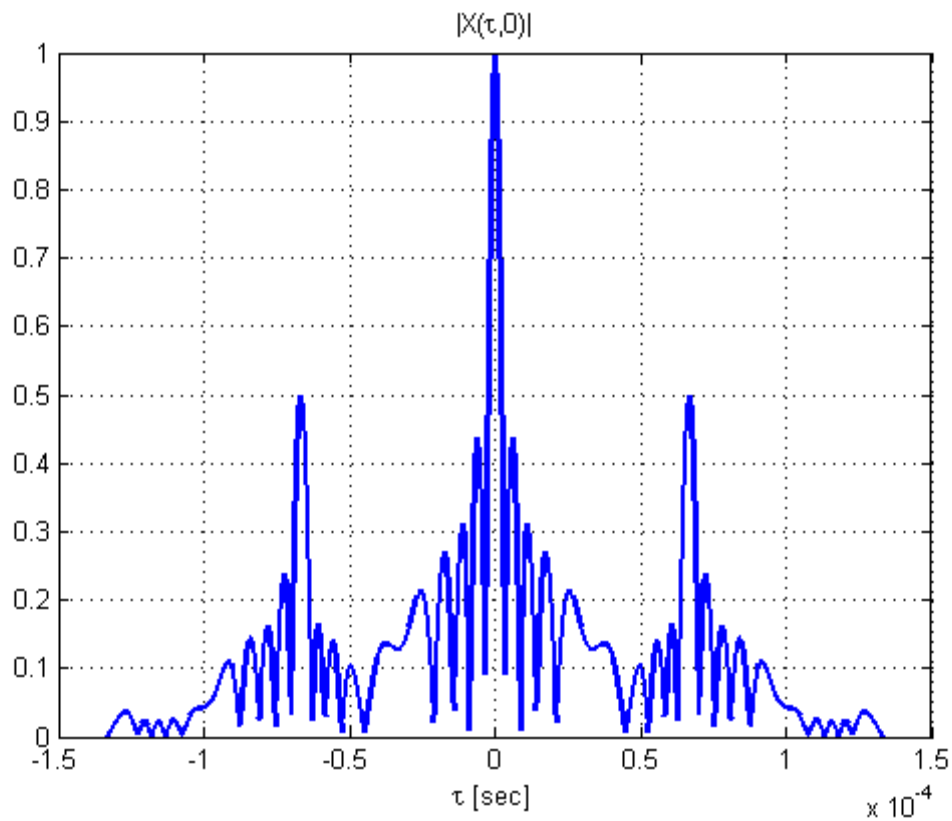


Figure 1.40 - AF of SFM pulse, 0-Doppler Cut. $T=2/f_0$, $f_0=15\text{kHz}$, $\beta=7$, $\varphi=\pi/2$

1.5 Ambiguity Function of a burst of pulses

In a typical radar system, during the *Time on Target (ToT)*, the receiver collects a set of N echoes scattered by the same target. Then, in this section, we evaluate the AF of unitary energy coherent burst of pulses. The pulse burst waveform is defined as

$$u(t) = \frac{1}{\sqrt{N}} \sum_{n=0}^{N-1} u_p(t - nT_R) \quad (1.33)$$

where $u_p(t)$ is a unitary energy pulse of time duration T , N is the number of coherent pulses while and T_R is the pulse repetition interval (PRI).

Using eq. (1.2), it is possible to write the CAF of $u(t)$ as a function of CAF of $u_p(t)$ [Ric05]:

$$X(\tau, \nu) = \frac{1}{N} \sum_{n=-(N-1)}^{N-1} X_p(\tau - nT_R, \nu) \exp(-j\pi\nu(N-1+n)T_R) \frac{\sin(\pi\nu(N-|n|)T_R)}{\sin(\pi\nu T_R)} \quad (1.34)$$

Recalling that $X_p(\tau, \nu)$ is zero for $|\tau| \geq T$, if $T_R > 2T$, which is always the case, the replica of $X_p(\tau, \nu)$ in (1.34) will not overlap, and the magnitude of the sum of the terms will be equal to the sum of the magnitude of the individual terms. The ambiguity function of the pulse burst can then be written as

$$|X(\tau, \nu)| = \frac{1}{N} \sum_{n=-(N-1)}^{N-1} |X_p(\tau - nT_R, \nu)| \cdot \left| \frac{\sin(\pi\nu(N-|n|)T_R)}{\sin(\pi\nu T_R)} \right| \text{ for } T_R > 2T \quad (1.35)$$

1.6 Ambiguity Function of a burst of rectangular pulses

As a first example, let consider a burst of rectangular pulses. The ambiguity function of this waveform is plotted in Figure 1.41 in a 3D plot and in Figure 1.42 in a contour plot. In particular we set $T=0.1$ sec, $T_R=4T$ and $N=5$.

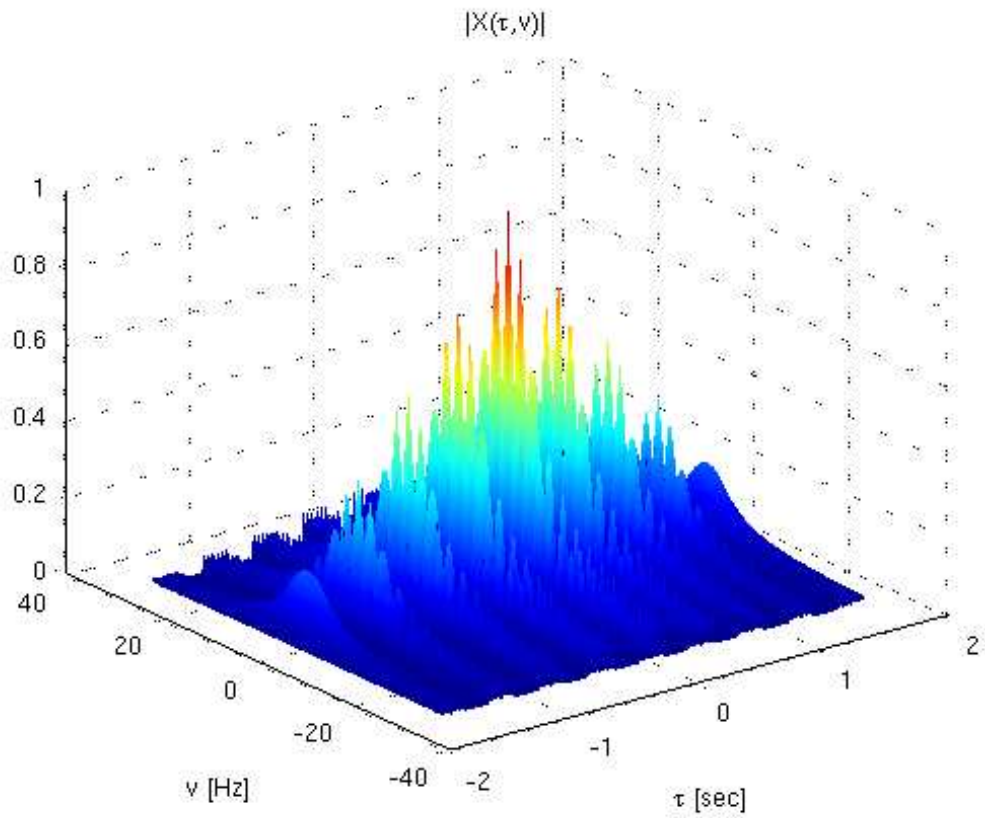


Figure 1.41 – AF of a burst of rectangular pulses, 3D-plot.

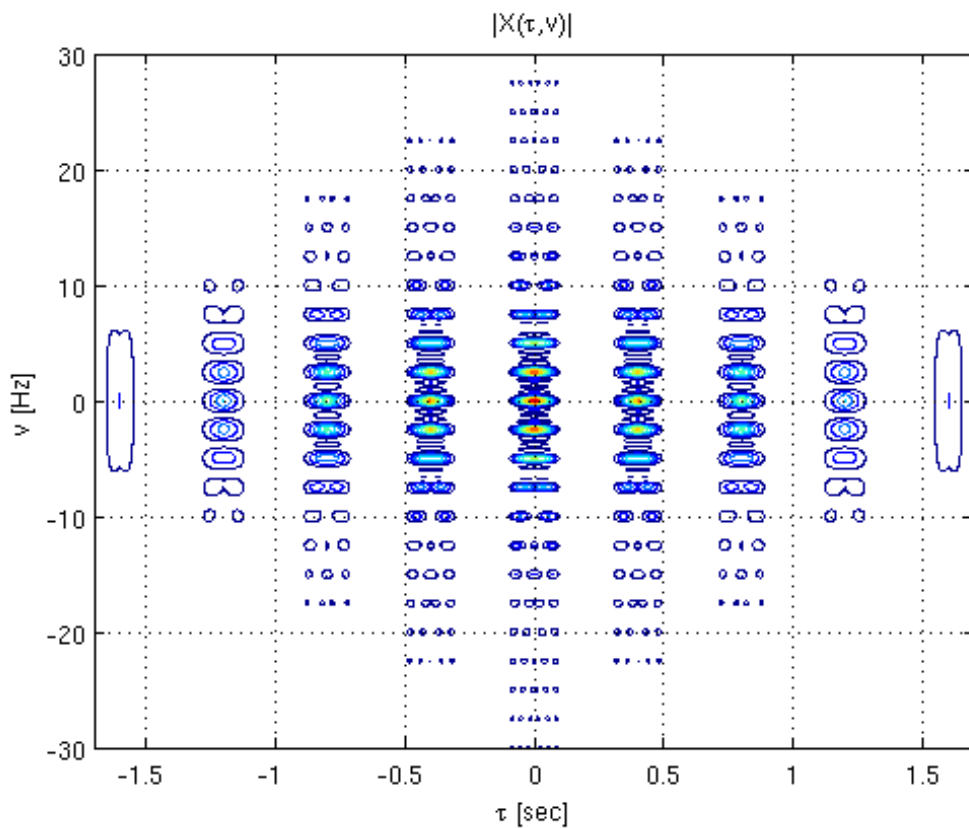


Figure 1.42 - AF of a burst of rectangular pulses, contour plot.

To understand this AF, it is convenient to look at the zero-delay and zero-Doppler sections. The zero-Doppler section is obtained by setting $\nu = 0$ in eq. (1.35) and recalling that $|X_p(\tau, 0)| = 1 - |\tau|/T$, then

$$|X(\tau, 0)| = \begin{cases} \sum_{n=-(N-1)}^{N-1} \left(1 - \frac{|n|}{N}\right) \cdot \left(1 - \frac{|\tau - nT_R|}{T}\right) & |\tau - nT_R| \leq T \\ 0 & \text{elsewhere} \end{cases} \quad (1.36)$$

This function is showed in Figure 1.44. The local peaks that appear every T seconds represent range ambiguities. This phenomenon is a characteristic of a pulse burst waveforms. It is not readily apparent if a peak at the matched filter output is due to a target at the apparent range, or that range plus or minus a multiple of $cT/2$ meters.

The zero-delay section is obtained by setting $\tau = 0$ in eq. (1.35) and recalling that $|X_p(0, \nu)| = |\sin(\pi\nu T)/(\pi\nu T)|$.

$$|X(0, \nu)| = \frac{1}{N} \left| \frac{\sin(\pi\nu T)}{\pi\nu T} \right| \cdot \left| \frac{\sin(\pi\nu NT_R)}{\sin(\pi\nu T_R)} \right| \quad (1.37)$$

The response is a *sinc* function with first zero at $\nu = 1/NT_R$, repeated with a period $1/T_R$. This basic behavior is weighted by a more slowly varying *sinc* function with its first zero at $1/T$. This structure is evident in Figure 1.43 which shows a portion of the zero-delay section.

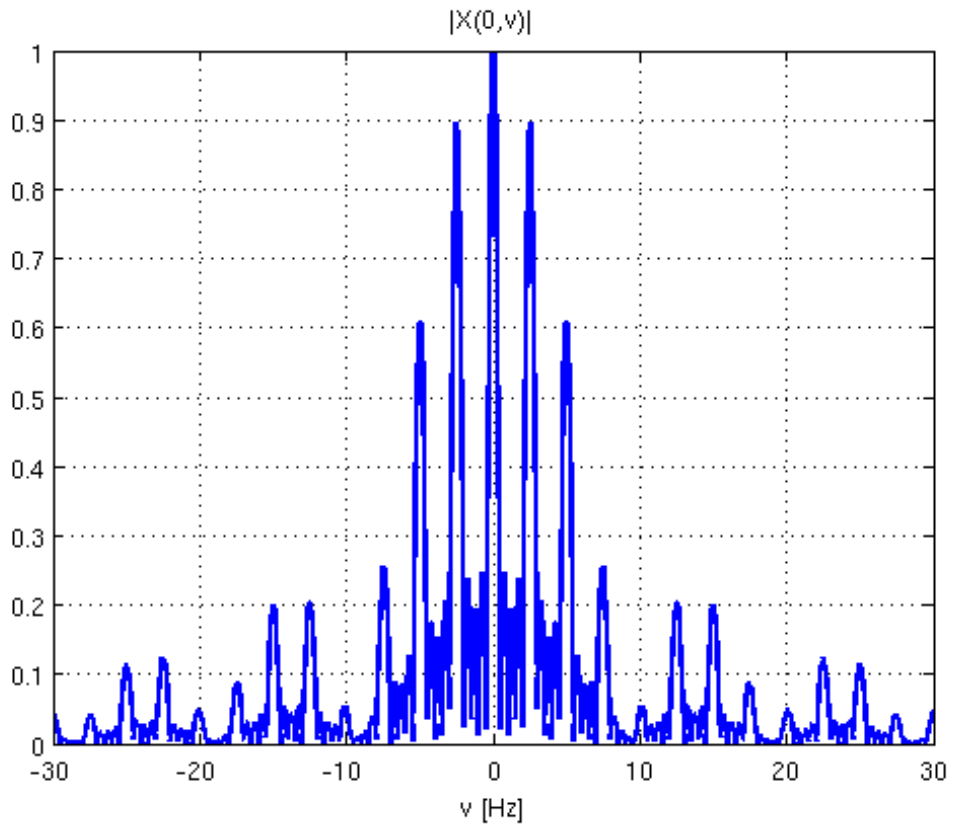


Figure 1.43 - AF of a burst of rectangular pulses, 0-delay section.

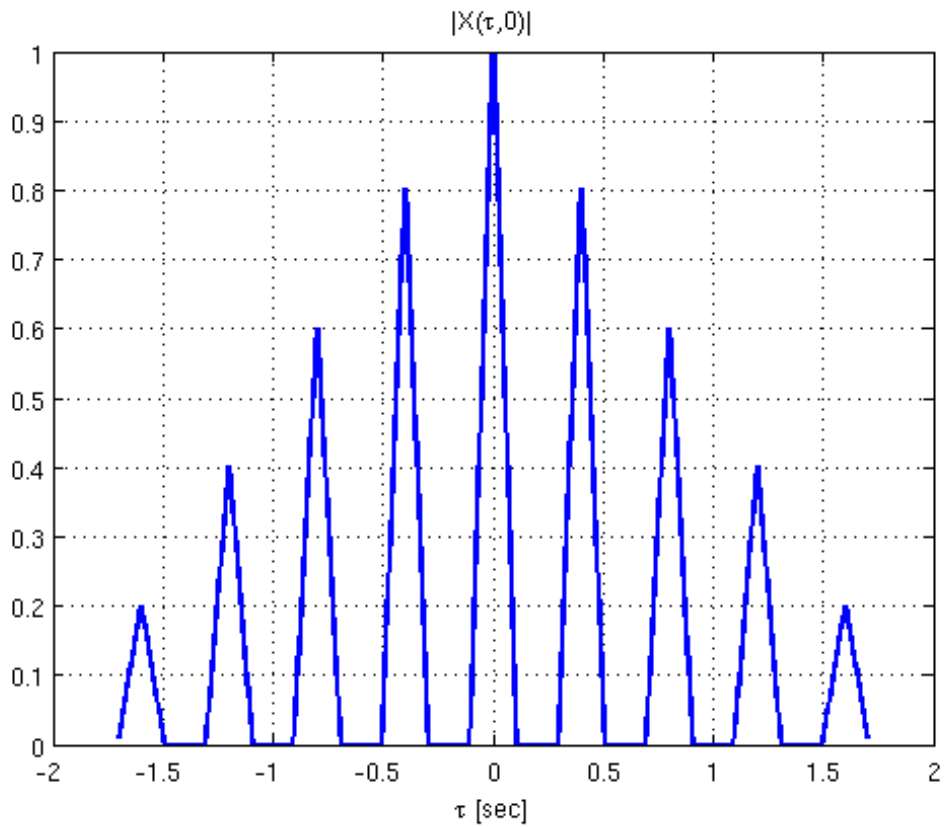


Figure 1.44 - AF of a burst of rectangular pulses, 0-Doppler section.

From Figures 1.41-1.44, it is clear how the various waveform parameters determine the resolution and ambiguities in range and Doppler. The individual pulse length T is chosen to achieve the desired delay resolution while the pulse repetition interval T_R sets the ambiguity interval in both delay and Doppler ($1/T$ hertz). Finally, once the pulse repetition interval is chosen, the number of pulses in the burst determines the Doppler resolution ($1/NT$ hertz).

1.7 Ambiguity Function of a burst of LFM pulses

Let consider now the case that will be useful in next Chapter where the Active Bistatic Radar systems will be analysed. Commonly, the signal transmitted in an active system is a burs of LFM pulses. In this case, the complex envelope of the transmitted unitary power signal is:

$$u(t) = \frac{1}{\sqrt{N}} \sum_{n=0}^{N-1} u_1(t - nT_R) \quad (1.38)$$

where

$$u_1(t) = \begin{cases} \frac{1}{\sqrt{T}} \exp(j\pi kt^2) & 0 \leq t \leq T \\ 0 & elsewhere \end{cases} \quad (1.39)$$

As in the previous sections, N is the number of pulses for each transmitted burst, T_R is the pulse repetition time and T is the duration of each pulse, with $T < T_R/2$. Moreover, $kT^2 = BT$ is the effective time-bandwidth product of the signal and B is the total frequency deviation.

Based upon the definition (1.34), we can calculate the CAF for the signal $u(t)$ in (1.38) and (1.39) as [Lev04]:

$$X(\tau, \nu) = \frac{1}{N} \sum_{n=-(N-1)}^{N-1} \exp(j\pi\nu(N-1+n)T_R) \frac{\sin(\pi\nu(N-|n|)T_R)}{\sin(\pi\nu T_R)} X_1(\tau - nT, \nu) \quad (1.40)$$

where

$$X_1(\tau, \nu) = \frac{\sin(\pi T(\nu - k\tau)(1 - |\tau|/T))}{\pi T(\nu - k\tau)} \text{rect}\left(\frac{\tau}{2T}\right) \quad (1.41)$$

is the Complex Ambiguity Function of a single LFM pulse.

If we limit the delay to the mainlobe area, namely to $|\tau| \leq T$ ($n=0$), the absolute value of eqs. (1.40) and (1.41) reduce to:

$$|X(\tau, \nu)| = \left| \frac{\sin(\pi T(\nu - k\tau)(1 - |\tau|/T))}{\pi T(\nu - k\tau)} \right| \left| \frac{\sin(\pi \nu N T_R)}{N \sin(\pi \nu T_R)} \right| \quad \text{for } |\tau| < T \quad (1.42)$$

The AF of the burst of LFM pulses is showed in Figures 9.2-9.5. In these Figures we fixed $BT=20$, $T_R=1$ s, $T=0.1$ s and $N=8$. For a better visualization, these Figures show only a zoom of the AF around its maximum. The classical structure of bed of nails is well evident.

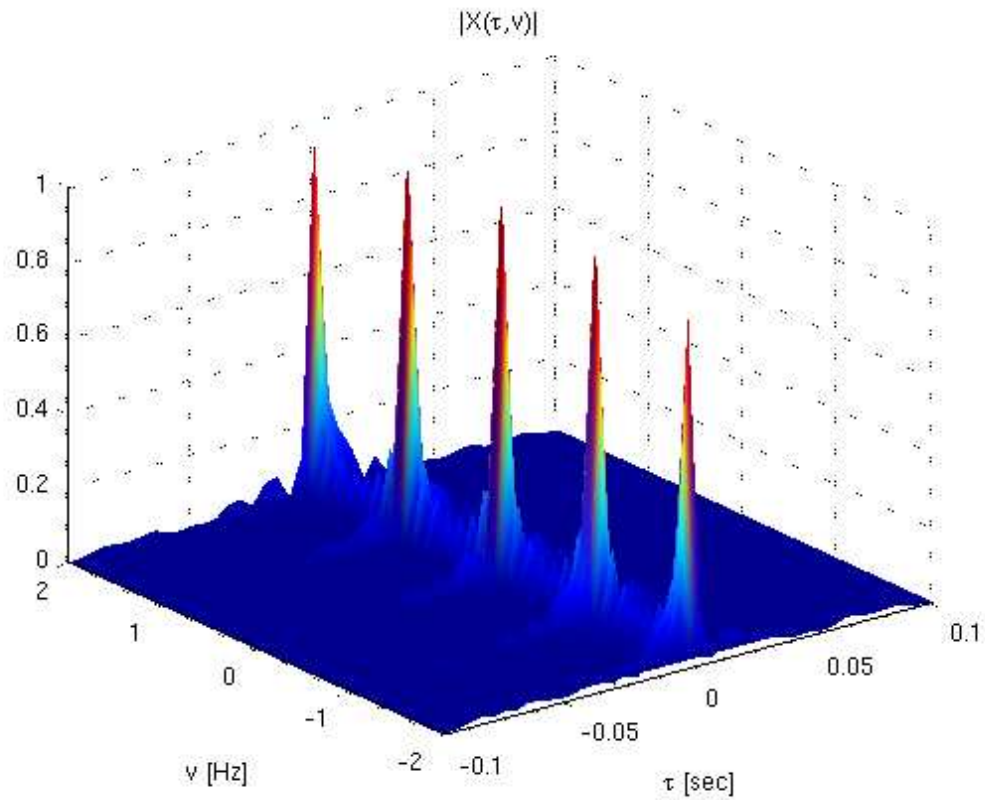


Figure 9.2 – AF of burst of chirps, $BT=20$, $T_R=1$ s, $T=0.1$ s and $N=8$. 3D-plot.

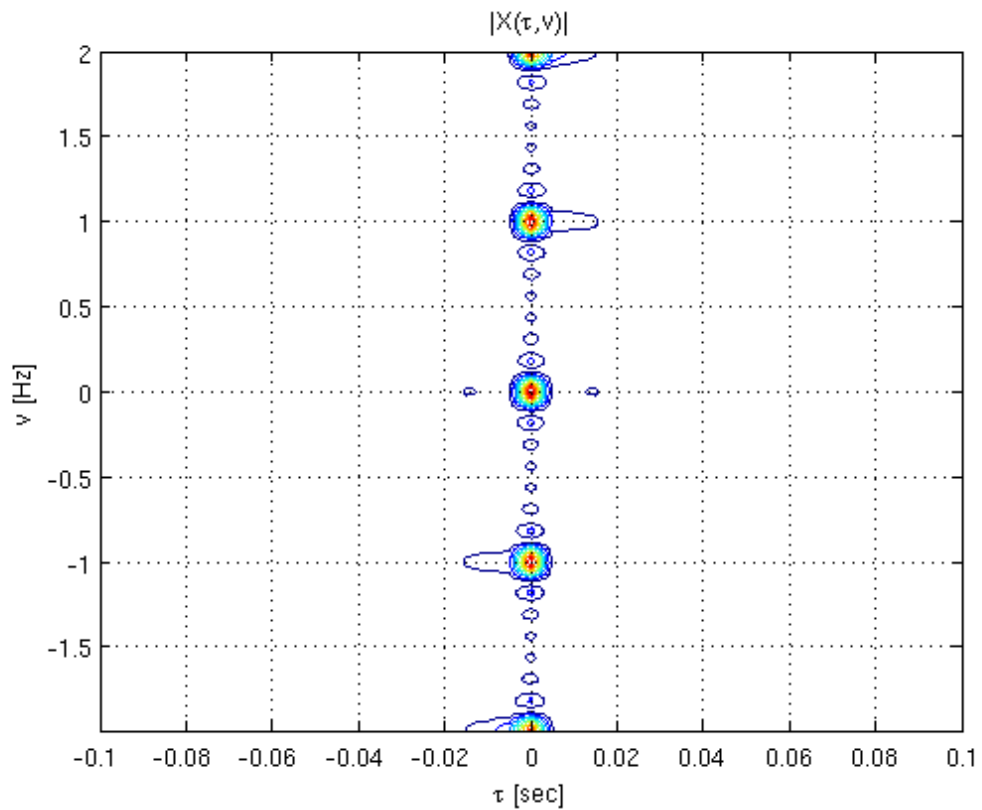


Figure 9.3 – AF of burst of chirps, $BT=20$, $T_R=1$ s, $T=0.1$ s and $N=8$. Contour plot.

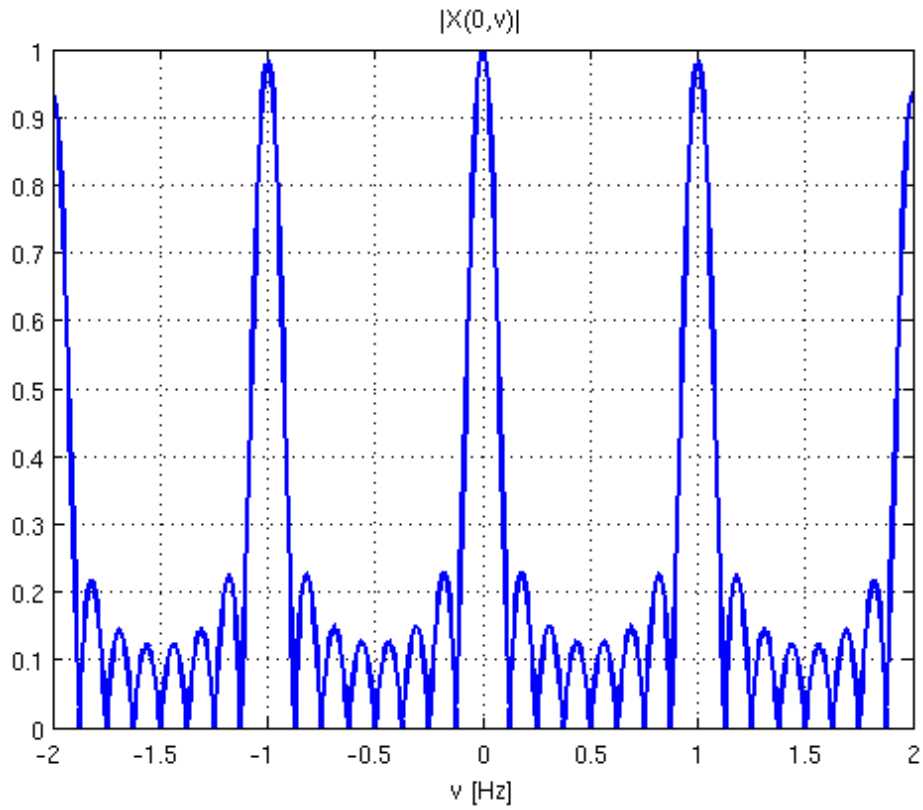


Figure 9.4 – AF of burst of chirps, $BT=20$, $T_R=1$ s, $T=0.1$ s and $N=8$. 0-delay cut.

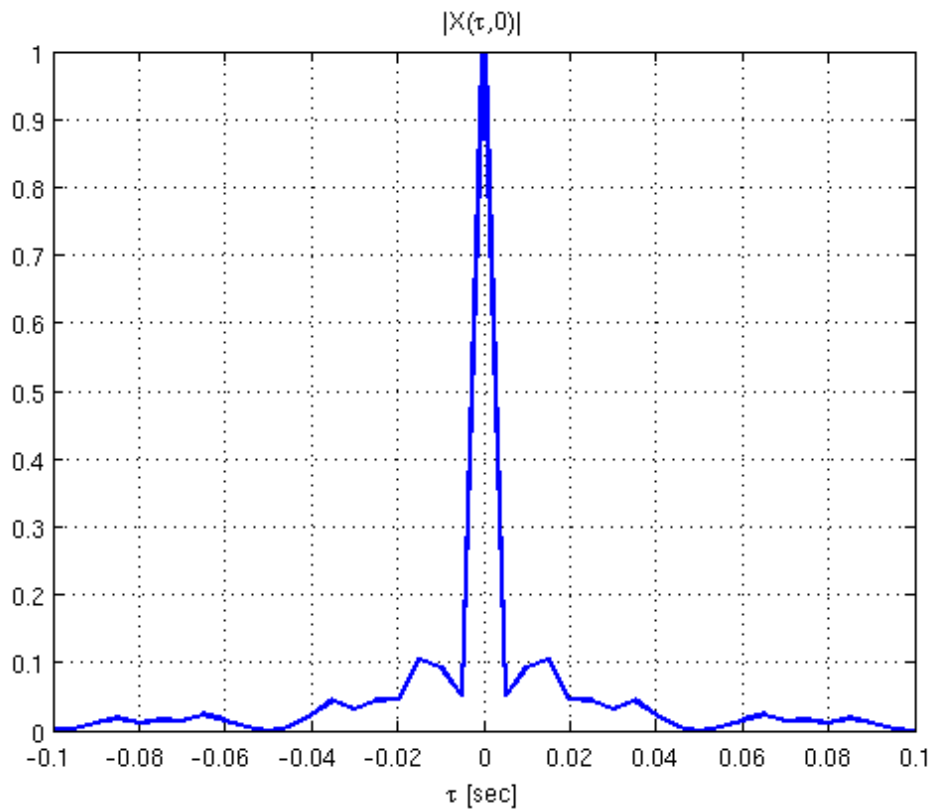


Figure 9.5 – AF of burst of chirps, $BT=20$, $T_R=1$ s, $T=0.1$ s and $N=8$. 0-Doppler cut.

2 Bistatic Radar Systems and Bistatic Ambiguity Function

2.1 Introduction

Bistatic radar may be defined as a radar in which the transmitter and receiver are at separate locations. The very first radars were bistatic, until pulsed waveforms and T/R switches were developed. Since then interest has varied up and down, but is demonstrably now at a high level, with numerous experimental systems being built and the results reported in the literature. Rather fewer operational systems, though, have been deployed.

Bistatic radars can operate with their own dedicated transmitters, which are specially designed for bistatic operation, or with transmitters of opportunity, which are designed for other purposes but found suitable for bistatic operation. When the transmitter of opportunity is from a monostatic radar the bistatic radar is often called a hitchhiker. When the transmitter of opportunity is from a non-radar transmission, such as broadcast, communications or radionavigation signal, the bistatic radar is called Passive Coherent Location (PCL). Finally, transmitters of opportunity in military scenarios can be designated either cooperative or non-cooperative, where cooperative denotes an allied or friendly transmitter and non-cooperative denotes a hostile or neutral transmitter. Passive bistatic radar operations are more restricted when using the latter.

In this Chapter we first define the bistatic parameters and the bistatic coordinate system and then we analyze the Bistatic Ambiguity Function for both the Active and Passive bistatic radars.

2.2 Bistatic Geometry

Before starting, it is necessary to describe the coordinate system used to represent a bistatic radar geometry. Figure 9.1 shows the coordinate system and its parameters. The positions of the TX, RX and of the target are generic. Considering an ordinary Cartesian grid, the TX is located at point T, whose coordinates are (x_T, y_T) , the RX is located at point R in (x_R, y_R) and the target is located at point B, whose coordinates are (x, y) . The triangle formed by the transmitter, the receiver and the target is called the bistatic triangle.

As shown in Figure 9.1, the sides of the bistatic triangle are R_T , R_R and L , where R_T is the range from transmitter to target, R_R is the range from receiver to target and L is the baseline between the transmitter and the receiver. The internal angles of the bistatic triangle, that, without lack of generality, are assumed to be positive, are α , β and γ . In particular, the bistatic angle β is the angle at the apex of the bistatic triangle, at the vertex which represents the target.

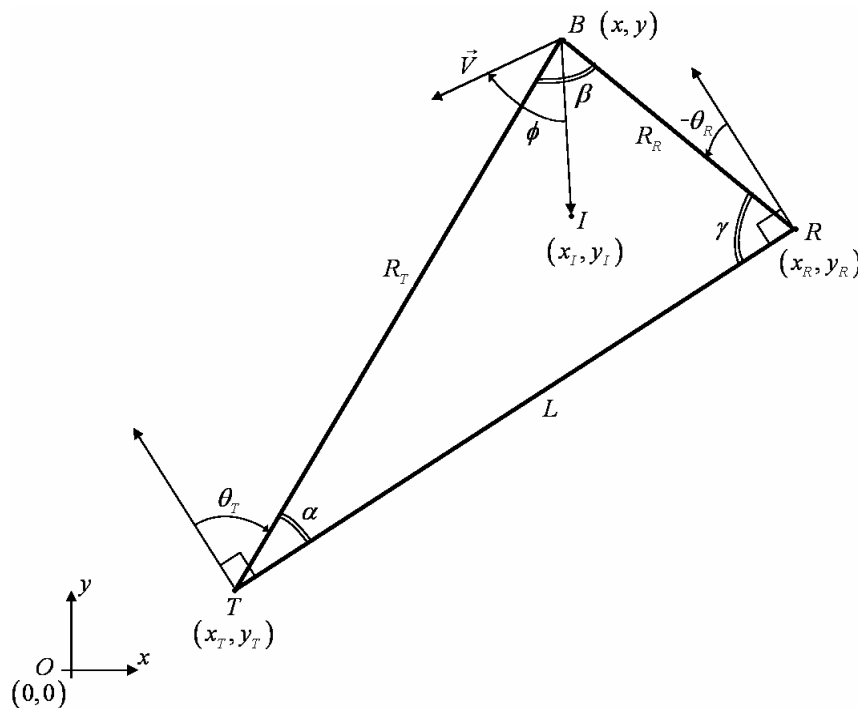


Figure 2.1 – Bistatic geometry

Assuming that the coordinates of the transmitter, the receiver and the target are known, it is possible to calculate all the parameters of the bistatic triangle. θ_T and θ_R are the look angle of the transmitter and the look angle of the receiver, respectively, they are measured positive clockwise from the vector normal to the baseline pointing towards the target.

From Figure 9.1, we have that $\theta_T = 90^\circ - \alpha$, $\theta_R = \gamma - 90^\circ$, $\beta = 180^\circ - \alpha - \gamma = \theta_T - \theta_R$, and from the cosine law we obtain: $R_T^2 = R_R^2 + L^2 + 2R_R L \sin \theta_R$, which gives the range from transmitter to target R_T , as a function of the range from receiver to target R_R and the look angle of the receiver θ_R . Figure 9.1 also shows the target velocity vector \vec{V} ; ϕ is the angle between the target velocity vector and the bistatic bisector, which is measured in a positive clockwise direction from the bisector. In particular the bistatic bisector is represented by the vector \vec{BI} , where I is the incenter of the bistatic triangle, whose coordinates are (x_I, y_I) .

The coordinates of the incenter can be easily obtained as

$$(x_I, y_I) = \frac{L}{L + R_R + R_T}(x, y) + \frac{R_R}{L + R_R + R_T}(x_T, y_T) + \frac{R_T}{L + R_R + R_T}(x_R, y_R). \quad (2.1)$$

In the bistatic geometry, an important parameter is the radial velocity V_a , which is the target velocity component along the bistatic bisector. From the observation of Figure 9.1, we obtain $V_a = \vec{V} \cdot \vec{BI} / |\vec{BI}| = |\vec{V}| \cos \phi$. Using the notation $\vec{V} = V_x \cdot \vec{x} + V_y \cdot \vec{y}$, it is easy to verify that:

$$V_a = \frac{(x_I - x)V_x + (y_I - y)V_y}{\sqrt{(x_I - x)^2 + (y_I - y)^2}}. \quad (2.2)$$

The bistatic radar geometry can be completely specified in terms of any three of the five parameters, θ_T , θ_R , L , R_R and R_T . In this chapter we will use θ_R , L , and R_R that can be obtained using the following equations:

$$L = \sqrt{(x_T - x_R)^2 + (y_T - y_R)^2}, \quad (2.3)$$

$$R_R = \sqrt{(x - x_R)^2 + (y - y_R)^2}, \quad (2.4)$$

$$R_T = \sqrt{(x - x_T)^2 + (y - y_T)^2}, \quad (2.5)$$

$$\vartheta_R = \cos^{-1} \left(\frac{R_R^2 + L^2 - R_T^2}{2R_R L} \right) - \frac{\pi}{2}. \quad (2.6)$$

2.3 Bistatic Ambiguity Function

As showed in Chapter 1, the mathematical definition of the Ambiguity Function is:

$$\left| X(\tau_H, \tau_a, \nu_H, \nu_a) \right| = \left| \int_{-\infty}^{+\infty} u(t - \tau_a) u^*(t - \tau_H) \exp(-j2\pi(\nu_H - \nu_a)t) dt \right| \quad (2.7)$$

where $u(t)$ is the complex envelope of the transmitted signal, τ_a and ν_a are the actual delay and Doppler frequency of the radar target respectively and τ_H and ν_H are the hypothesized delay and frequency. The AF in (2.7) can be also expressed as a function of τ and ν , where $\tau = \tau_H - \tau_a$ and $\nu = \nu_H - \nu_a$.

As known, in the monostatic case there is a linear relationship between τ_a and ν_a , and the range position R_a and radial velocity V_a of the target, more specifically $\tau_a = 2R_a/c$ and $\nu_a = -2V_a f_c/c$. Similar relations hold for τ_H and ν_H . Due to this linear relationship, the AF in the range – velocity plane has the same behaviour of the one expressed as a function of τ and ν , except for a scale factor. Therefore, in the monostatic configuration, the information about the target delay and the target Doppler shift directly provides information about the target range and the target velocity. This is different in the bistatic case, where the relation between time delay and Doppler frequency, and target distance and velocity is not linear.

Referring to the bistatic geometry of Figure 2.1, for obtain the expression of the bistatic ambiguity function, we must replace in (2.7) the relations [Tsa97]:

$$\tau_H(R_R, \theta_R, L) = \frac{R_R + \sqrt{R_R^2 + L^2 + 2R_R L \sin \theta_R}}{c}, \quad (2.8)$$

$$\nu_H(R_R, V_B, \theta_R, L) = 2 \frac{f_c}{c} V_B \sqrt{\frac{1}{2} + \frac{R_R + L \sin \theta_R}{2\sqrt{R_R^2 + L^2 + 2R_R L \sin \theta_R}}}. \quad (2.9)$$

Similar relations hold for τ_H and ν_H ⁴. It is clearly apparent from equations (2.8) and (2.9) that in the bistatic case, the Doppler shift and the delay depends on the geometry of the bistatic triangle and the relation between time delay and Doppler frequency, and target distance and velocity is not linear. Due to the non linear equations (2.8) and (2.9), it is apparent that the

⁴ Note that R_a and V_a are the actual range and bistatic velocity, while R_T and $V_B = V \cos \varphi$ are the hypothesized range and bistatic velocity

Bistatic Ambiguity Function depends also on the bistatic geometry parameters, i.e. the target direction of arrival, the bistatic baseline length and the distance between the target and the receiver. This dependence is very strong and can be appreciated later with an illustrative example. considering the case of a target close to the baseline joining the transmitter and receiver.

2.4 Active Bistatic Radar Systems: Burst of LFM pulses

In active bistatic radar systems, the transmitter is specially designed for bistatic operation. For this reason here we assume that the transmitted waveform is a sequence of linear frequency modulated (LFM) pulses or chirps. As showed in the previous Chapter, the CAF in the delay-Doppler plane can be expressed as:

$$X(\tau, \nu) = \frac{1}{N} \sum_{n=-(N-1)}^{N-1} \exp(j\pi\nu(N-1+n)T_R) \frac{\sin(\pi\nu(N-|n|)T_R)}{\sin(\pi\nu T_R)} X_1(\tau-nT, \nu) \quad (2.10)$$

where

$$X_1(\tau, \nu) = \frac{\sin(\pi T(\nu - k\tau)(1 - |\tau|/T))}{\pi T(\nu - k\tau)} \text{rect}\left(\frac{\tau}{2T}\right) \quad (2.11)$$

is the Complex Ambiguity Function of a single LFM pulse.

Moreover, if we limit the delay to the mainlobe area, namely to $|\tau| \leq T$, the AF reduces to:

$$|X(\tau, \nu)| = \left| \frac{\sin(\pi T(\nu - k\tau)(1 - |\tau|/T))}{\pi T(\nu - k\tau)} \right| \left| \frac{\sin(\pi\nu N T_R)}{N \sin(\pi\nu T_R)} \right| \quad \text{for } |\tau| < T \quad (2.12)$$

To link eqs. (2.11) and (2.12) to the bistatic geometry of Figure 2.1 and to obtain the expression of the Bistatic AF (BAF), we must replace in (2.11) and (2.12) the relations $\tau = \tau_H - \tau_a$ and $\nu = \nu_H - \nu_a$ calculated using (2.8)-(2.9).

The contour plot of the BAF is illustrated in Figure 2.1 in the plane R_R - V_B with $V_B = V \cos \phi$, $V_a = 600\text{m/s}$ and $R_a = 20\text{Km}$ and $L = 50\text{Km}$. The presence of discrete peaks (nails) is evident even in the bistatic plane, even if they are not symmetrically distributed. The main peak corresponds to $V_a = 600\text{m/s}$ and $R_a = 20\text{Km}$.

The shape of the bistatic function strongly depends on the target angle θ_R , particularly for high values of BT . To highlight this phenomenon, in Figures 2.3-2.6 we show the zero-delay and zero-Doppler slices of the ambiguity function for different values of θ_R and BT . Both cuts are maximum for values of range and target velocity corresponding to the true values $V_a=600\text{m/s}$ and $R_a=20\text{Km}$. For values of θ_R close to $-\pi/2$ the bistatic AF presents multiple peaks. The worst case is for $\theta_R = -\pi/2$, that is, when the target is on the baseline. If the target is between the transmitter and the receiver, the AF is flat and the range and velocity resolutions are completely lost. For values of θ_R far from $-\pi/2$ the shape of the bistatic ambiguity function is practically the same (see, for instance, $\theta_R = -\pi$, and $\theta_R = \pi/6$ in Figs. 4-7). For increasing values of N the range resolution improves, but many peaks appear in the bistatic AF shape.

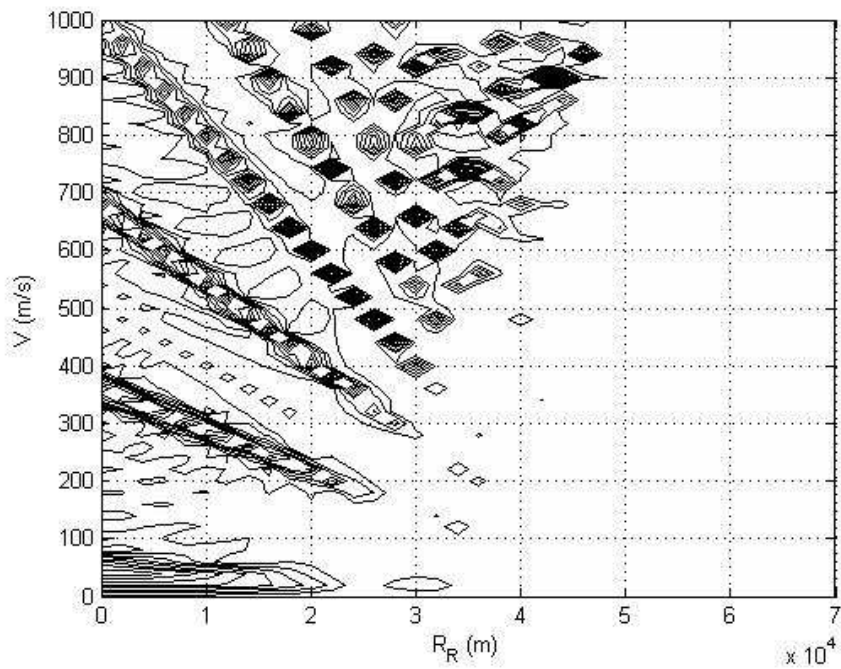


Figure 2.2 – BAF of a burst of Linear Frequency Modulated pulses, $BT=250$, $T_R=1\text{ms}$, $T=250\mu\text{s}$, $N=8$, $\theta_R=-0.47\pi$, $L=50\text{Km}$, $V_a=600\text{m/s}$, $R_a=20\text{Km}$.

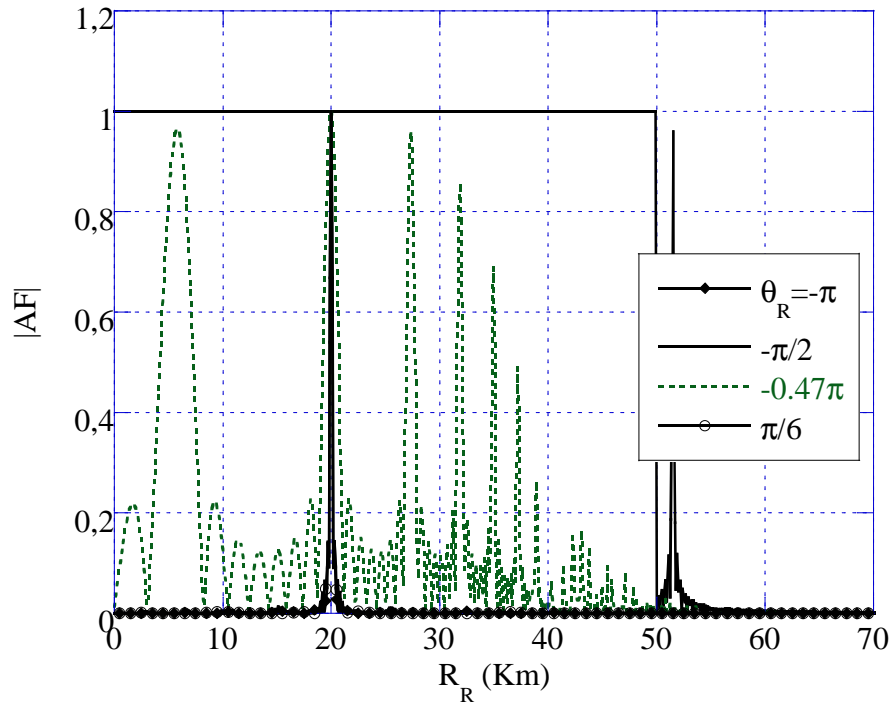


Figure 2.3 – BAF of a burst of Linear Frequency Modulated pulses; Zero-Doppler cut, $BT=20$, $T_R=1\text{ms}$, $T=250\mu\text{s}$, $N=8$, $L=50\text{Km}$, $V_a=600\text{m/s}$, $R_a=20\text{Km}$.

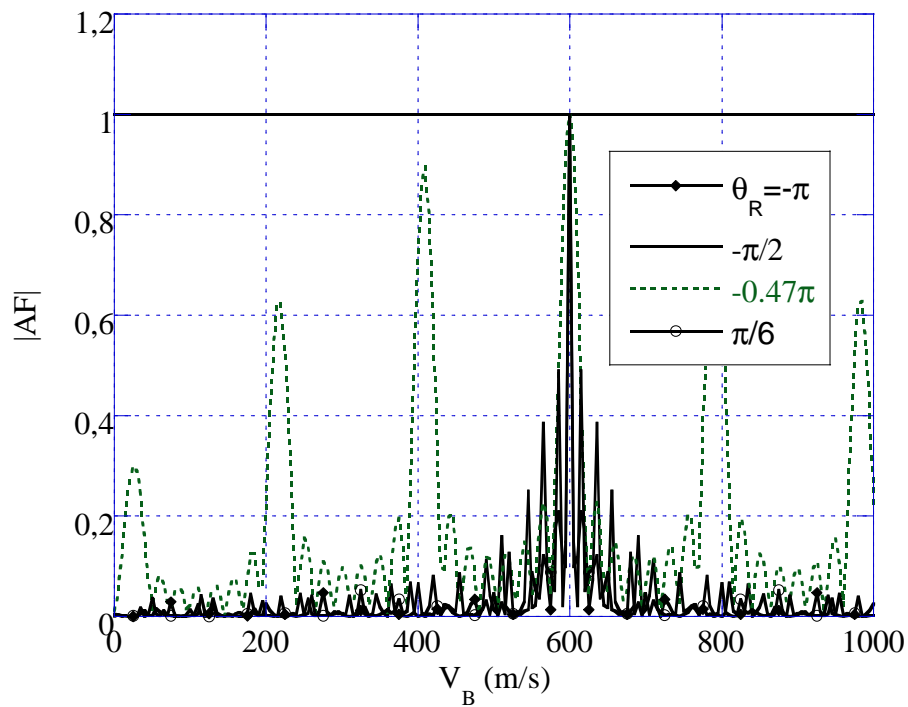


Figure 2.4 – BAF of a burst of Linear Frequency Modulated pulses; Zero-delay cut, $BT=20$, $T_R=1\text{ms}$, $T=250\mu\text{s}$, $N=8$, $L=50\text{Km}$, $V_a=600\text{m/s}$, $R_a=20\text{Km}$.

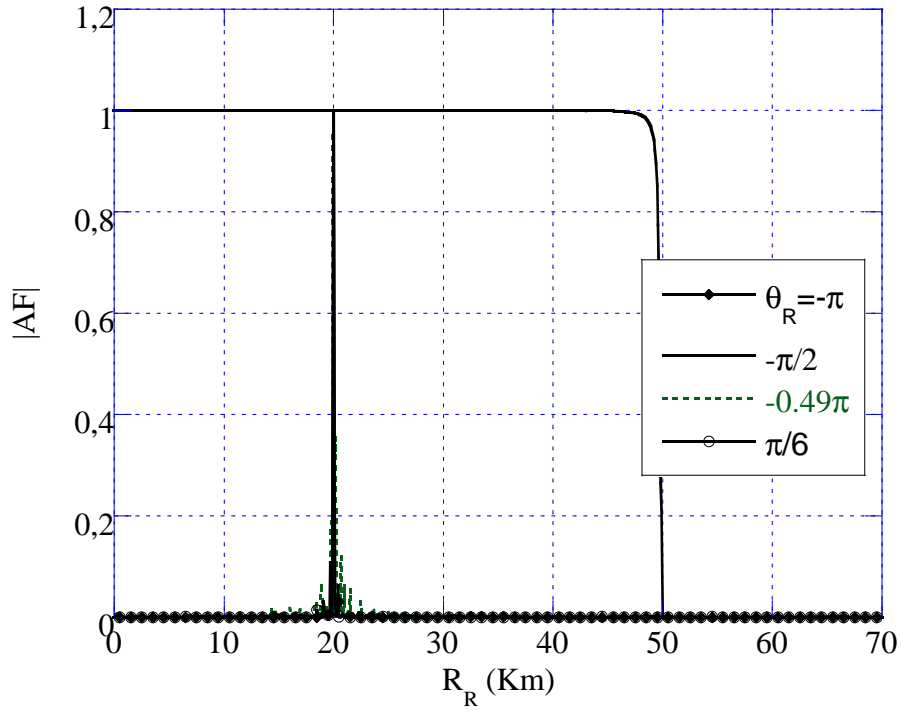


Figure 2.5 – BAF of a burst of Linear Frequency Modulated pulses; Zero-Doppler cut, $BT=250$, $T_R=1\text{ms}$, $T=250\mu\text{s}$, $N=8$, $L=50\text{Km}$, $V_a=600\text{m/s}$, $R_a=20\text{Km}$.

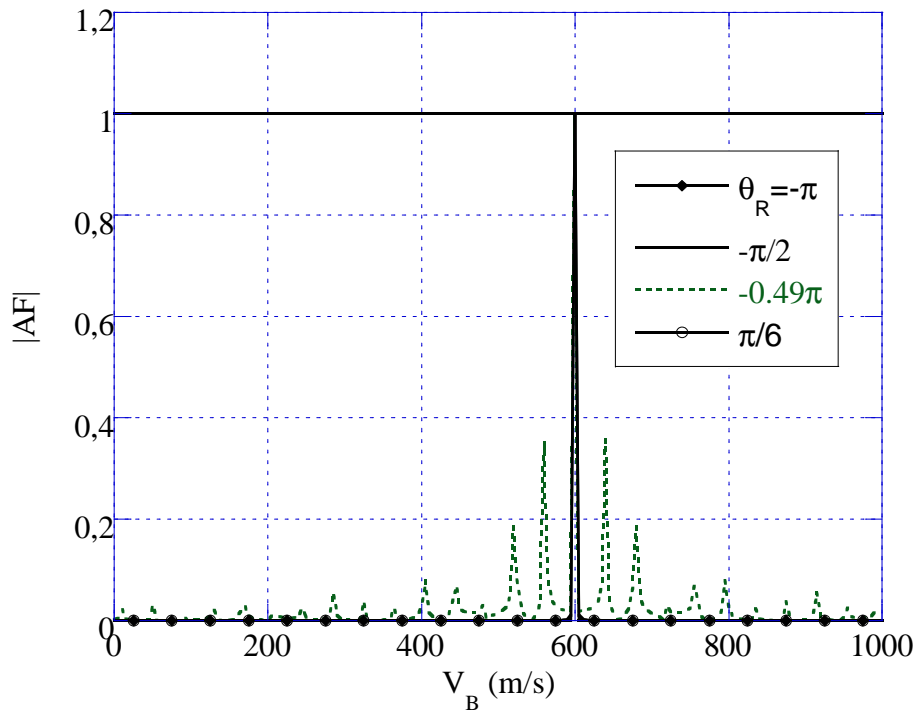


Figure 2.6 – BAF of a burst of Linear Frequency Modulated pulses; Zero-delay cut, $BT=250$, $T_R=1\text{ms}$, $T=250\mu\text{s}$, $N=8$, $L=50\text{Km}$, $V_a=600\text{m/s}$, $R_a=20\text{Km}$.

2.5 Passive Bistatic Radar Systems: SFM pulse

In the context of bistatic radar system, great interest has been devoted to systems making use of illuminators of opportunity, such as broadcast or communications signals, tracking targets by range and Doppler information. These techniques have become known as Passive Coherent Location (PCL), and have the advantage that the receivers do not need any transmitter hardware of their own, and are completely passive, and hence undetectable. Of all the transmitters of opportunity available in the environment, broadcast transmitters represent some of the most attractive for surveillance purposes, owing to their high powers and excellent coverage. Moreover, PCL systems can allow the use of parts of the RF spectrum (VHF and UHF) that are not usually available for radar operation, and which may offer a counterstealth advantage, since stealth treatments designed for microwave radar frequencies may be less effective at VHF and UHF.

This Section deals with the Bistatic Ambiguity Function of a Sinusoidal Frequency Modulated Pulse, which models the signal transmitted by a non co-operative Frequency Modulated (FM) commercial radio station.

As showed in the previous Chapter, we suppose that the complex envelope of the signal transmitted by the transmitter of opportunity is the unitary power pulse given by:

$$u(t) = \begin{cases} \frac{1}{\sqrt{T}} e^{j\beta \sin(2\pi f_0 t + \varphi)} & |t| \leq \frac{T}{2} \\ 0 & elsewhere \end{cases} \quad (2.13)$$

That is a pulse which instantaneous frequency is a sinusoidal oscillation. In particular, T is the observation time, β is the modulation index and $1/f_0$ is the period of the instantaneous frequency. In other words, we assumed that, during the observation time, the modulating signal transmitted by a radio station can be approximated by a sinusoidal oscillation.

This can be justified considering that in a typical FM radio, the program content is speech and/or music, which are often modelled as periodic vibrations.

Moreover, the chosen signal is a mathematically tractable model that makes it feasible to study the analyzed scenario rigorously.

In Chapter 1 we calculated the CAF of a SFM pulse in the delay-Doppler plane. In particular, we found that:

$$X(\tau, \nu) = \sum_n \sum_k e^{j(n-k)\varphi} J_n(\beta) J_k(\beta) e^{+j2\pi k f_0 \tau} X_1(\tau, \nu - (n-k)f_0) \quad (2.14)$$

where

$$X_1(\tau, \nu) = e^{-j\pi\nu\tau} \frac{\sin(\pi\nu(T - |\tau|))}{\pi\nu T} \quad (2.15)$$

for $|\tau| \leq T$ and 0 elsewhere, where we set $\tau = \tau_H - \tau_a$, $\nu = \nu_H - \nu_a$ and $J_n(\beta)$ is the n^{th} order Bessel function of the first kind.

To link eqs. (2.14) and (2.15) to the bistatic geometry of Figure 2.1 and to obtain the expression of the BAF, we must replace in (2.14) and (2.15) the relations $\tau = \tau_H - \tau_a$ and $\nu = \nu_H - \nu_a$ calculated using (2.8)-(2.9). Figures 2.7-2.18 show the BAF obtained by setting $f_0=15\text{kHz}$, $T=20/f_0$, $\beta=5$, $R_R=30\text{km}$ and $V_B=250\text{m/sec}$.

We fixed the values of f_0 and β considering that the signal emitted by a FM commercial radio station is an audible signal (speech and/or music), therefore the frequency of the modulating signal f_0 have to belong to the range of audible frequency, whose accepted standard range is from 20Hz to 20kHz. Moreover, FM commercial radio stations use bandwidth of about 150kHz, therefore, according to Carson's rule⁵, we fixed $f_0=15\text{kHz}$ and $\beta=5$.

As previously shown, the BAF heavily depends on the baseline length L and the receiver look angle θ_R . We analyzed the case $L=50\text{km}$, $L=20\text{km}$, $\theta_R=0$ and $\theta_R=-\pi/2$. It is interesting to observe the case when $R_R \leq L$ and the receiver look angle θ_R is $-\pi/2$. In this case the target is in the baseline, the resulting delay is L/c and the radial component of the velocity V_B is zero, and therefore resolution is totally lost.

⁵ The Carson's bandwidth is the approximate bandwidth of a frequency (or phase) modulated signal. Carson's bandwidth rule is expressed by the relation $B_C = 2(\Delta f + B)$ where Δf is the peak frequency deviation, and B is the bandwidth of the modulating signal. In our case, it is easy to demonstrate that $B_C \approx 2\beta f_0$. Carson's rule does not apply well when the modulating signal contains discontinuities, such as a square wave.

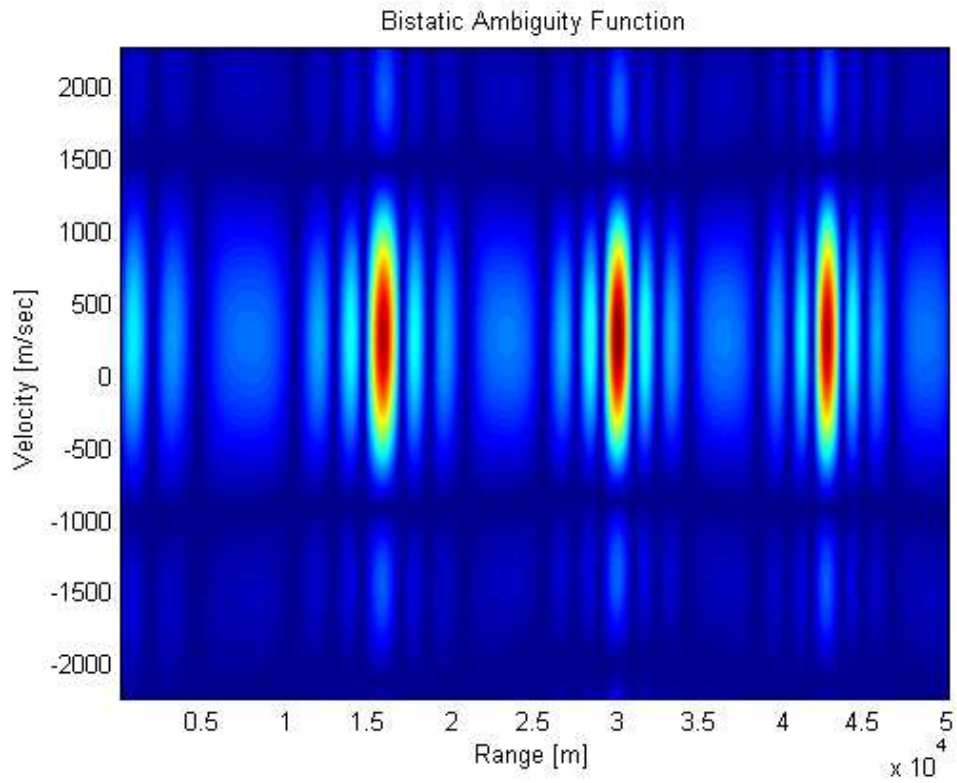


Figure 2.7 – BAF of a SFM pulse, contour plot. $L=50\text{km}$, $\theta_R=0$.

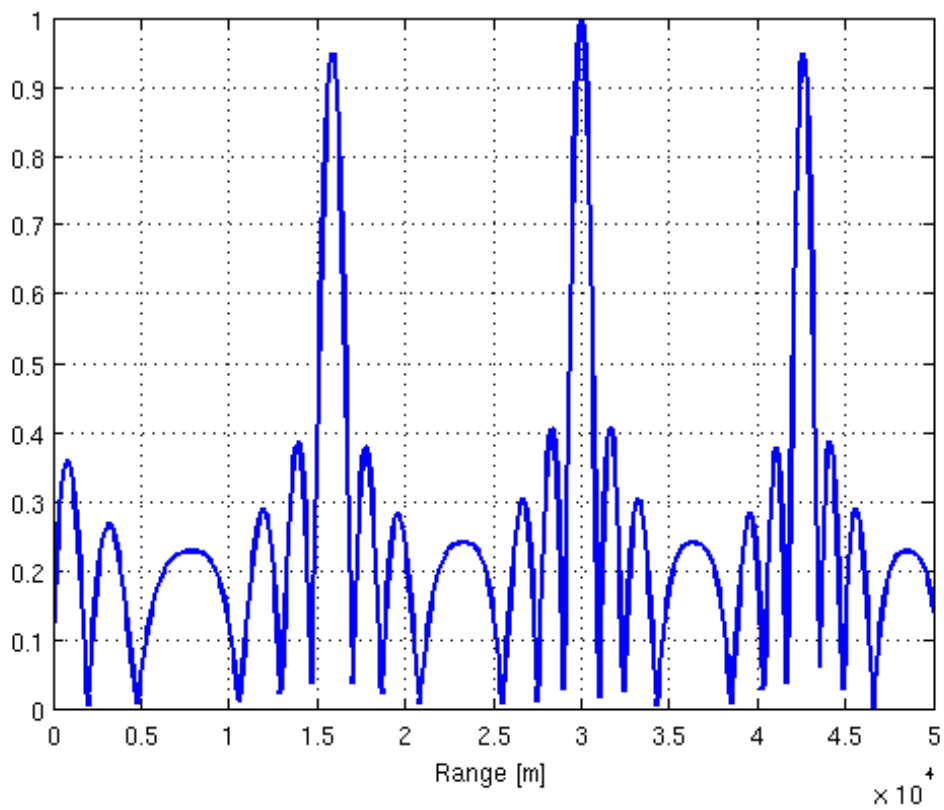


Figure 2.8 – BAF of a SFM pulse, 0-Doppler Cut, $L=50\text{km}$, $\theta_R=0$.

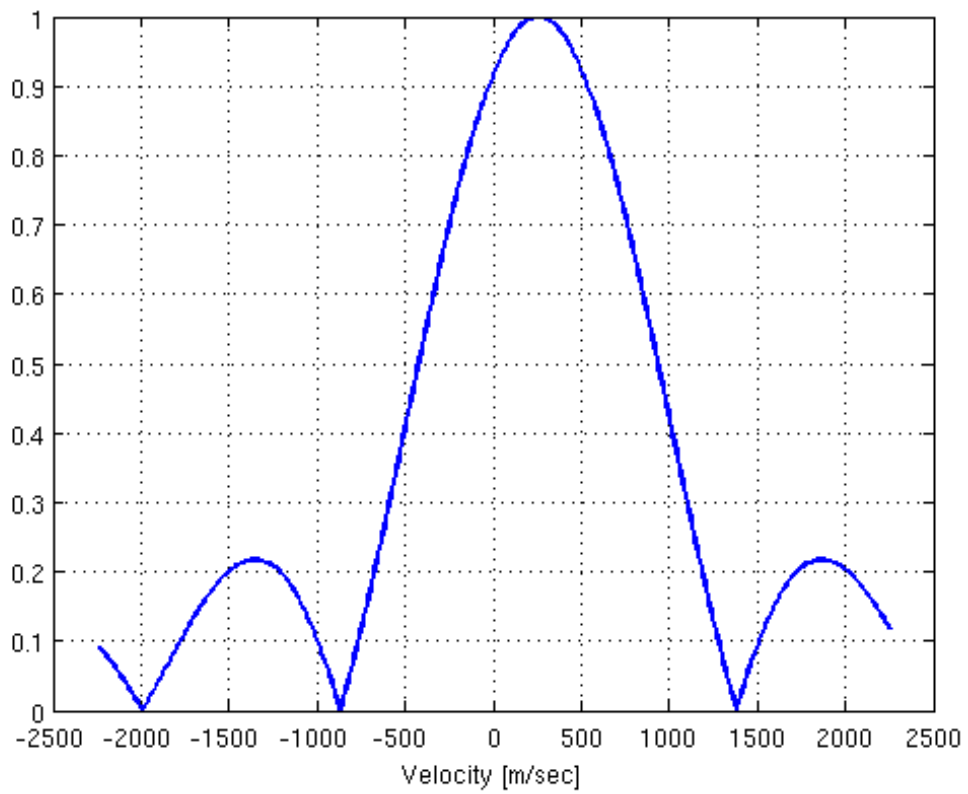


Figure 2.9 – BAF of a SFM pulse, 0-Delay cut, $L=50\text{km}$, $\theta_R=0$.

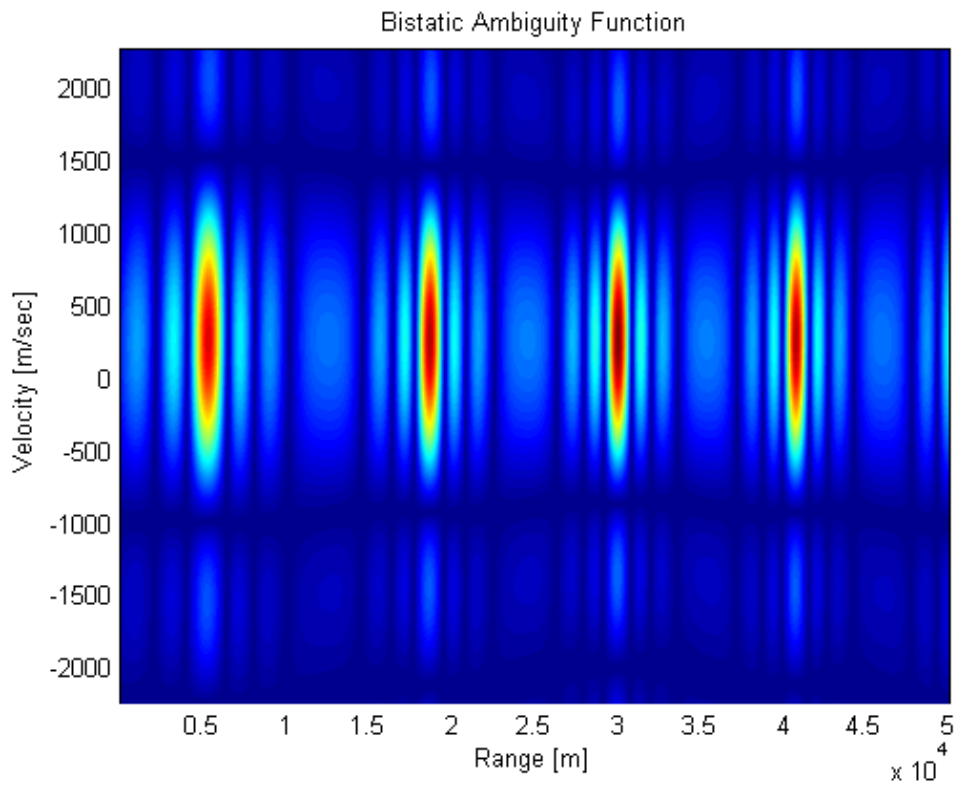


Figure 2.10 – BAF of a SFM pulse, contour plot. $L=20\text{km}$, $\theta_R=0$.

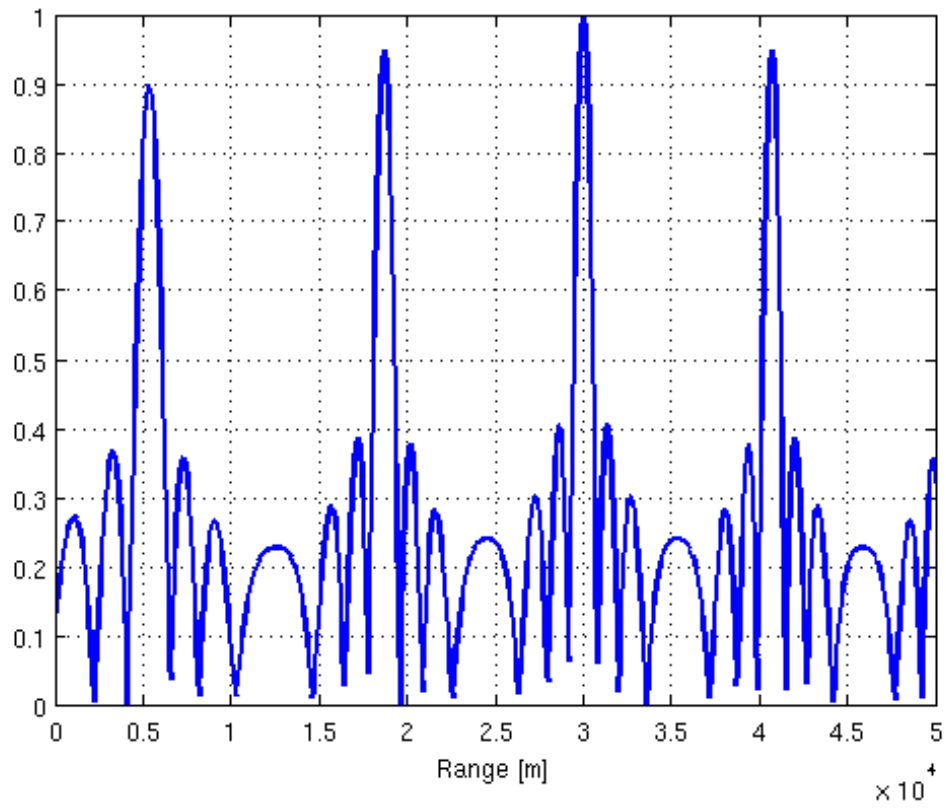


Figure 2.11 – BAF of a SFM pulse, 0-Doppler Cut, $L=20\text{km}$, $\theta_R=0$.

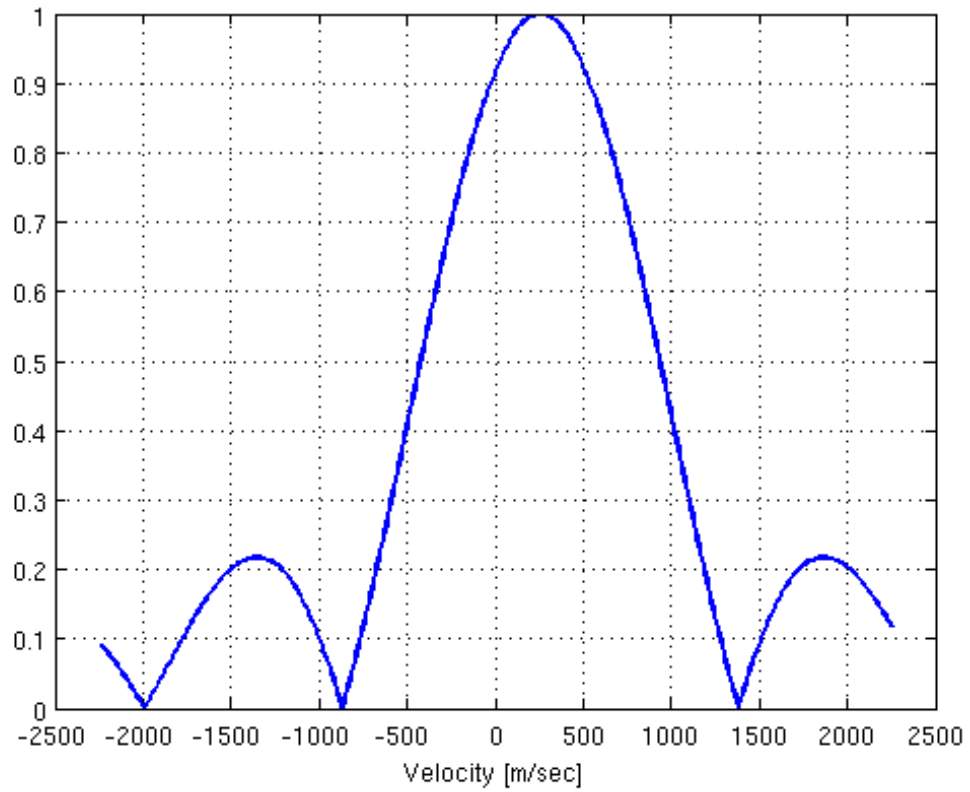


Figure 2.12 – BAF of a SFM pulse, 0-Delay cut, $L=20\text{km}$, $\theta_R=0$.

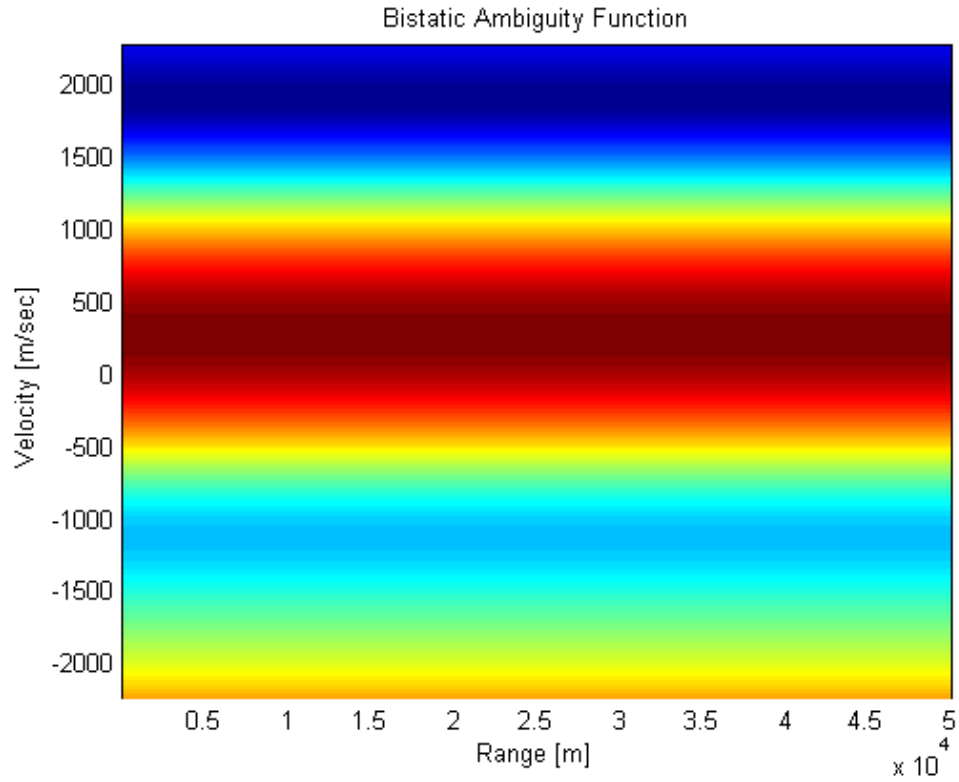


Figure 2.13 – BAF of a SFM pulse, contour plot. $L=50\text{km}$, $\theta_R=-\pi/2$.

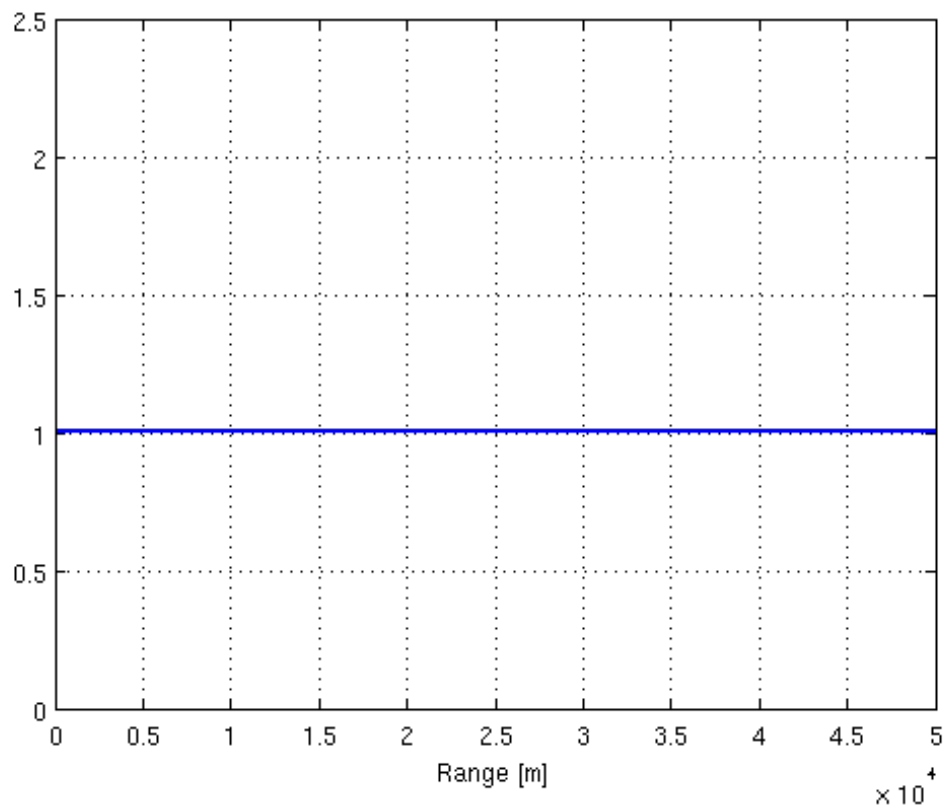


Figure 2.14 – BAF of a SFM pulse, 0-Doppler Cut, $L=50\text{km}$, $\theta_R=-\pi/2$.

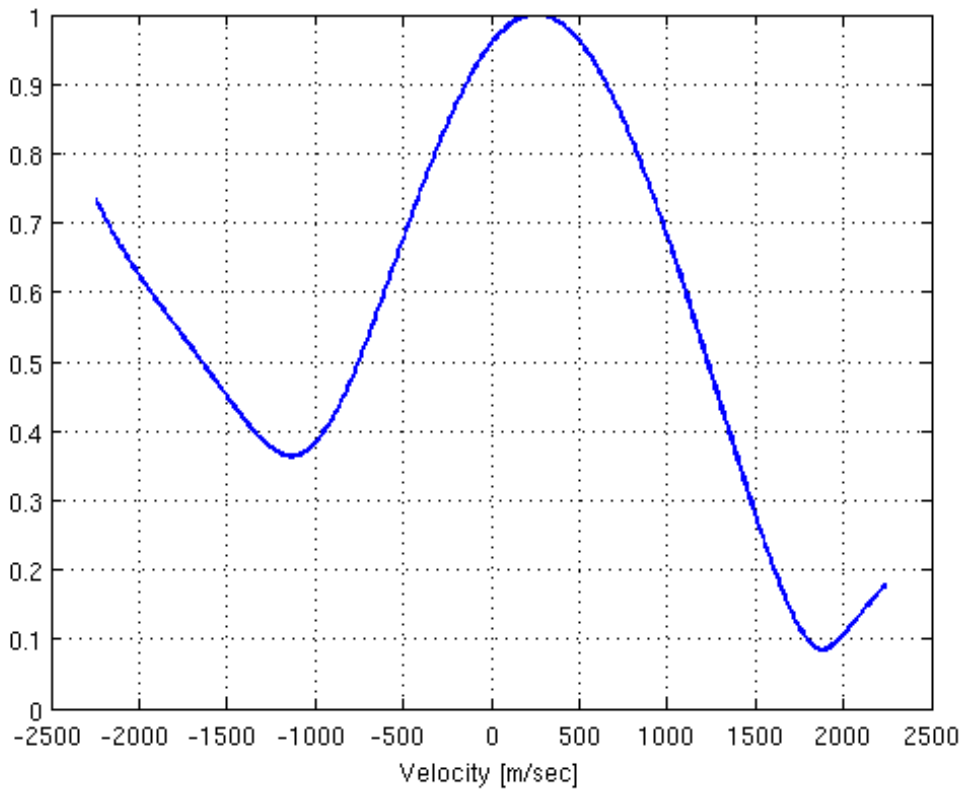


Figure 2.15 – BAF of a SFM pulse, 0-Delay cut, $L=50\text{km}$, $\theta_R=-\pi/2$.

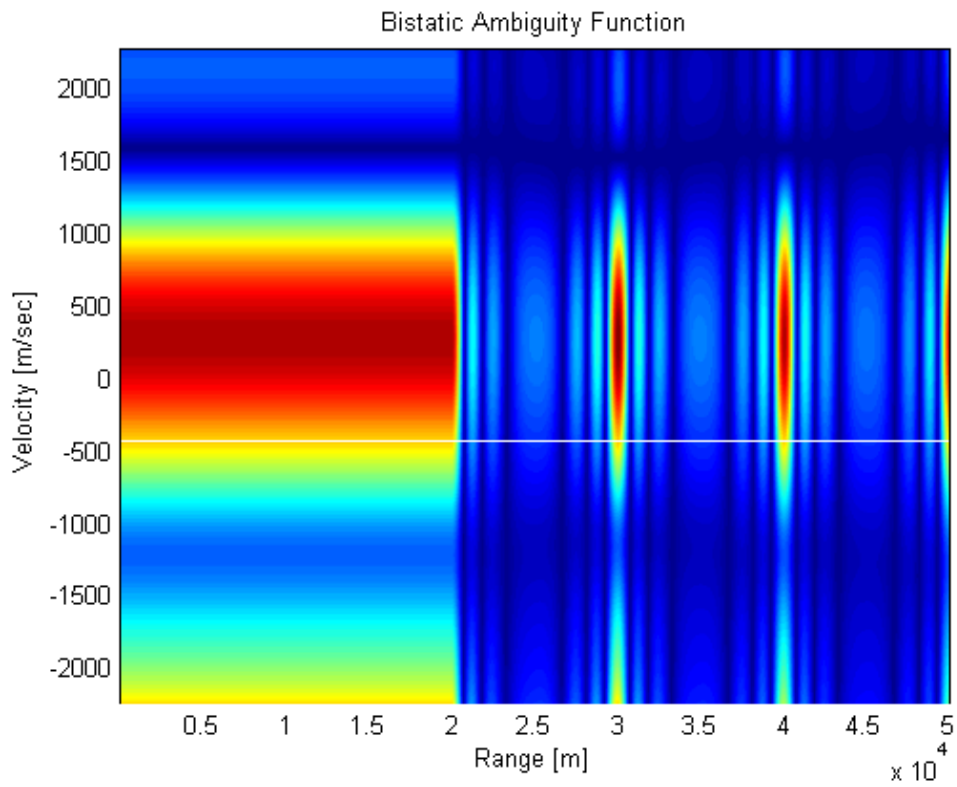


Figure 2.16 – BAF of a SFM pulse, contour plot. $L=20\text{km}$, $\theta_R=-\pi/2$.

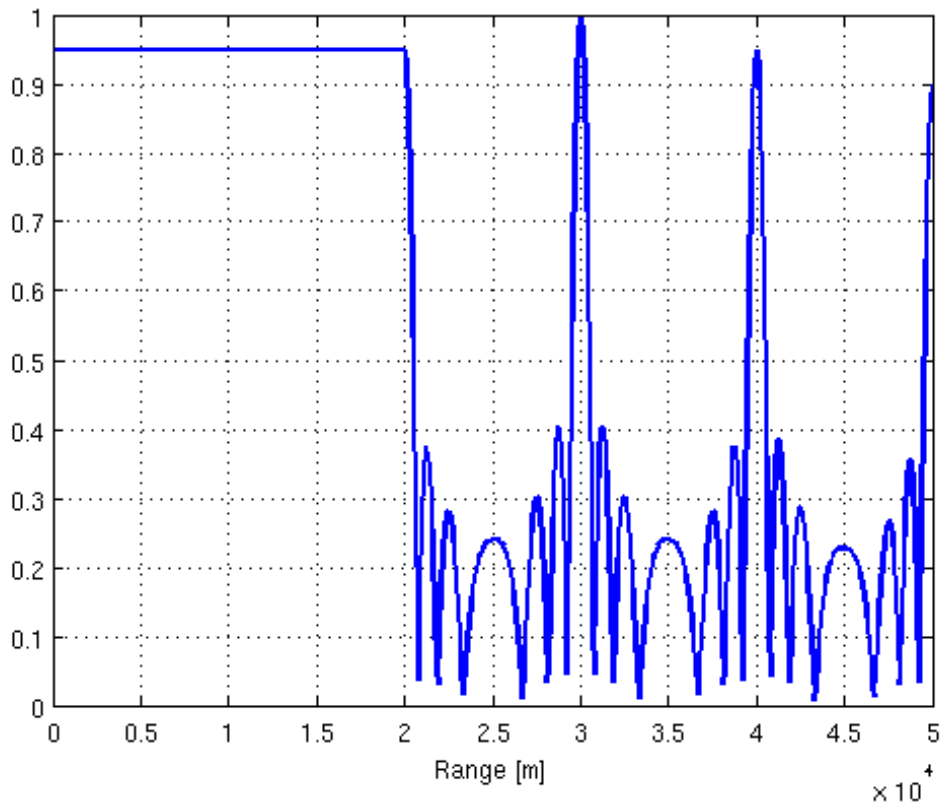


Figure 2.17 – BAF of a SFM pulse, 0-Doppler Cut, $L=20\text{km}$, $\theta_R=-\pi/2$.

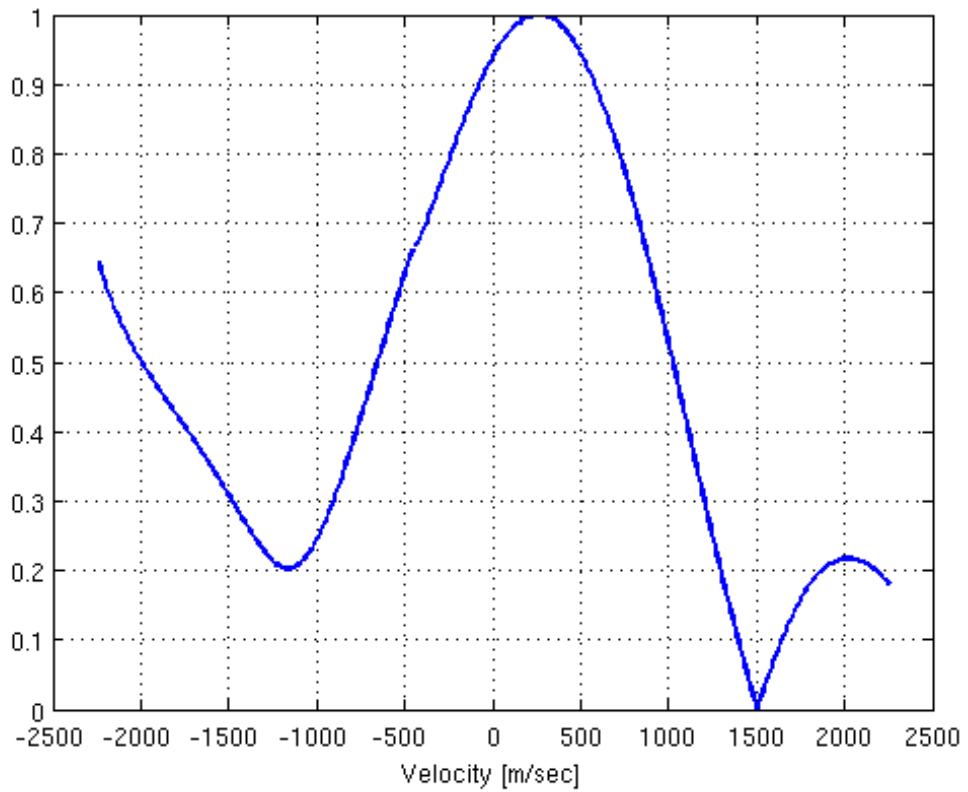


Figure 2.18 – BAF of a SFM pulse, 0-Delay cut, $L=20\text{km}$, $\theta_R=-\pi/2$.

3 Channel Performance Evaluation in a Bistatic Radar System

3.1 Bistatic Cramér-Rao Lower Bounds

The AF directly determines the capability of a system to resolve two targets that exist at different ranges from the radar and have different radial velocities. When the receiver signals from the target have similar energy, the resolution is equal to the half power width of the AF mainlobe. The AF is also related to the accuracy with which the range and the velocity of a given target can be estimated. When the Signal to Noise power Ratio (*SNR*) is high, the CRLBs on estimation accuracy are dependent on both the *SNR* and the second derivatives of the AF, that is, the sharpness of the AF mainlobe. Unlike the ambiguity function which provides information on the global resolution, the CRLBs are a local measure of estimation accuracy. Anyway, both can be used to assess the error properties of the estimates of the signal parameters. In [Van71] the author derived a relationship between CRLB and ambiguity function, which has been successfully used in the analysis of passive and active arrays [Dog01]. In the monostatic configuration, [Van71] claims that for the Fisher Information Matrix (FIM) the following relationship holds (for more details see Appendix A):

$$\mathbf{J}_M(\tau, \nu) = -2SNR \left[\begin{array}{cc} \frac{\partial^2 \Theta(\tau, \nu)}{\partial \tau^2} & \frac{\partial^2 \Theta(\tau, \nu)}{\partial \tau \partial \nu} \\ \frac{\partial^2 \Theta(\tau, \nu)}{\partial \nu \partial \tau} & \frac{\partial^2 \Theta(\tau, \nu)}{\partial \nu^2} \end{array} \right]_{\tau=0, \nu=0} = -2SNR \mathbf{J}_{M_n} \quad (3.1)$$

where $\Theta(\tau, \nu) = |X(\tau, \nu)|^2$ and *SNR* is the signal-to-noise power ratio at the receiver. The AF is the heart of this expression since it is the log-likelihood function excluding the effect of signal attenuation and clutter. In Appendix A we report the proof of relation (3.1). The property in (3.1) does not depend on the choice of the parameters of the ambiguity function, then it holds for both monostatic and bistatic case. From (3.1) the CRLBs follow: $\text{CRLB}(\tau_a) = [\mathbf{J}_M(\tau_a, \nu_a)]_{1,1}^{-1}$ and $\text{CRLB}(\nu_a) = [\mathbf{J}_M(\tau_a, \nu_a)]_{2,2}^{-1}$. In the bistatic configuration we

should write the ambiguity function in terms of the bistatic $\tau(R_R, \theta_R, L)$ and $\nu(R_R, V_B, \theta_R, L)$ and derive it with respect to the useful parameters R_R and V_B . Then

$$\mathbf{J}_B(R_R, V_B) = -2SNR \left[\begin{array}{cc} \frac{\partial^2 \Theta(R_R, V_B)}{\partial R_R^2} & \frac{\partial^2 \Theta(R_R, V_B)}{\partial R_R \partial V_B} \\ \frac{\partial^2 \Theta(R_R, V_B)}{\partial V_B \partial R_R} & \frac{\partial^2 \Theta(R_R, V_B)}{\partial V_B^2} \end{array} \right]_{R_R=R_a, V_B=V_a} \quad (3.2)$$

For the calculation of the CRLBs in the bistatic domain we can partially use the results of the monostatic domain. Following the ‘‘chain rule’’ (see Appendix D for details) of the derivative we can prove that:

$$\begin{aligned} \frac{\partial^2 \Theta(R_R, V_B)}{\partial R_R^2} &= [\mathbf{J}_{M_n}]_{1,1} \left(\frac{\partial \tau}{\partial R_R} \right)^2 + 2[\mathbf{J}_{M_n}]_{1,2} \frac{\partial \tau}{\partial R_R} \frac{\partial \nu}{\partial R_R} + [\mathbf{J}_{M_n}]_{2,2} \left(\frac{\partial \nu}{\partial R_R} \right)^2 \\ &+ \frac{\partial \Theta(\tau, \nu)}{\partial \tau} \frac{\partial^2 \tau}{\partial R_R^2} + \frac{\partial \Theta(\tau, \nu)}{\partial \nu} \frac{\partial^2 \nu}{\partial R_R^2} \end{aligned} \quad (3.3)$$

$$\begin{aligned} \frac{\partial^2 \Theta(R_R, V_B)}{\partial V_B^2} &= [\mathbf{J}_{M_n}]_{1,1} \left(\frac{\partial \tau}{\partial V_B} \right)^2 + 2[\mathbf{J}_{M_n}]_{1,2} \frac{\partial \tau}{\partial V_B} \frac{\partial \nu}{\partial V_B} + [\mathbf{J}_{M_n}]_{2,2} \left(\frac{\partial \nu}{\partial V_B} \right)^2 \\ &+ \frac{\partial \Theta(\tau, \nu)}{\partial \tau} \frac{\partial^2 \tau}{\partial V_B^2} + \frac{\partial \Theta(\tau, \nu)}{\partial \nu} \frac{\partial^2 \nu}{\partial V_B^2} \end{aligned} \quad (3.4)$$

$$\begin{aligned} \frac{\partial^2 \Theta(R_R, V_B)}{\partial V_B \partial R_R} &= \frac{\partial^2 \Theta(R_R, V_B)}{\partial R_R \partial V_B} = [\mathbf{J}_{M_n}]_{1,1} \frac{\partial \tau}{\partial V_B} \frac{\partial \tau}{\partial R_R} + [\mathbf{J}_{M_n}]_{1,2} \frac{\partial \tau}{\partial R_R} \frac{\partial \nu}{\partial V_B} + \frac{\partial \Theta(\tau, \nu)}{\partial \tau} \frac{\partial^2 \tau}{\partial R_R \partial V_B} \\ &+ [\mathbf{J}_{M_n}]_{1,2} \frac{\partial \tau}{\partial V_B} \frac{\partial \nu}{\partial R_R} + [\mathbf{J}_{M_n}]_{2,2} \frac{\partial \nu}{\partial R_R} \frac{\partial \nu}{\partial V_B} + \frac{\partial \Theta(\tau, \nu)}{\partial \nu} \frac{\partial^2 \nu}{\partial V_B \partial R_R} \end{aligned} \quad (3.5)$$

From equations (2.8)-(2.9) we have:

$$\frac{\partial \nu}{\partial R_R} = \frac{f_c}{2c} V_B \frac{L^2 \cos^2 \theta_R}{(R_R^2 + L^2 + 2R_R L \sin \theta_R)^{3/2} \sqrt{\frac{1}{2} + \frac{R_R + L \sin \theta_R}{2\sqrt{R_R^2 + L^2 + 2R_R L \sin \theta_R}}} \quad (3.6)$$

$$\frac{\partial \nu}{\partial V_B} = \frac{2f_c}{c} \sqrt{\frac{1}{2} + \frac{R_R + L \sin \theta_R}{2\sqrt{R_R^2 + L^2 + 2R_R L \sin \theta_R}}} \quad (3.7)$$

$$\frac{\partial \tau}{\partial R_R} = \frac{1}{c} \left(1 + \frac{R_R + L \sin \theta_R}{\sqrt{R_R^2 + L^2 + 2R_R L \sin \theta_R}} \right) \quad (3.8)$$

$$\frac{\partial^2 \nu}{\partial R_R \partial V_B} = \frac{1}{V_B} \frac{\partial \nu}{\partial R_R} \quad (3.9)$$

$$\frac{\partial^2 \tau}{\partial R_R^2} = \frac{L^2 \cos^2 \theta_R}{c (R_R^2 + L^2 + 2R_R L \sin \theta_R)^{3/2}} \quad (3.10)$$

$$\frac{\partial^2 \nu}{\partial R_R^2} = \frac{- \left[6 (R_R^2 + L^2 + 2R_R L \sin \theta_R)^{1/2} (R_R + L \sin \theta_R) + (R_R^2 + L^2 + 2R_R L \sin \theta_R) + 5 (R_R + L \sin \theta_R)^2 \right]}{4c (\sqrt{2} f_c V_B L^2 \cos^2 \theta_R)^{-1} (R_R^2 + L^2 + 2R_R L \sin \theta_R)^{9/4} \left[(R_R^2 + L^2 + 2R_R L \sin \theta_R)^{1/2} + (R_R + L \sin \theta_R) \right]^{3/2}} \quad (3.11)$$

$$\frac{\partial \tau}{\partial V_B} = \frac{\partial^2 \tau}{\partial R_R \partial V_B} = \frac{\partial^2 \tau}{\partial V_B^2} = \frac{\partial^2 \nu}{\partial V_B^2} = 0 \quad (3.12)$$

If the derivative of the modulus of the ambiguity function is continuous with respect to τ and ν , then $\frac{\partial \Theta(\tau, \nu)}{\partial \tau} = 0$ and $\frac{\partial \Theta(\tau, \nu)}{\partial \nu} = 0$ in their maximum. Therefore, taking into account also eq. (3.12) we can write

$$\frac{\partial^2 \Theta(R_R, V_B)}{\partial R_R^2} = [\mathbf{J}_{M_n}]_{1,1} \left(\frac{\partial \tau}{\partial R_R} \right)^2 + 2 [\mathbf{J}_{M_n}]_{1,2} \frac{\partial \tau}{\partial R_R} \frac{\partial \nu}{\partial R_R} + [\mathbf{J}_{M_n}]_{2,2} \left(\frac{\partial \nu}{\partial R_R} \right)^2 \quad (3.13)$$

$$\frac{\partial^2 \Theta(R_R, V_B)}{\partial V_B^2} = [\mathbf{J}_{M_n}]_{2,2} \left(\frac{\partial \nu}{\partial V_B} \right)^2 \quad (3.14)$$

$$\frac{\partial^2 \Theta(R_R, V_B)}{\partial V_B \partial R_R} = \frac{\partial^2 \Theta(R_R, V_B)}{\partial R_R \partial V_B} = [\mathbf{J}_{M_n}]_{1,2} \frac{\partial \tau}{\partial R_R} \frac{\partial \nu}{\partial V_B} + [\mathbf{J}_{M_n}]_{2,2} \frac{\partial \nu}{\partial R_R} \frac{\partial \nu}{\partial V_B} \quad (3.15)$$

Or, in the more compact form:

$$\mathbf{J}_B(R_R, V_B) = \mathbf{P} \mathbf{J}_M(\tau, \nu) \mathbf{P}^T \quad (3.16)$$

where

$$\mathbf{P} = \begin{bmatrix} \frac{\partial \tau}{\partial R_R} & \frac{\partial \nu}{\partial R_R} \\ \frac{\partial \tau}{\partial V_B} & \frac{\partial \nu}{\partial V_B} \end{bmatrix} \quad (3.17)$$

The relationship showed in eq. (3.16) is very interesting because the two effects that describe the Bistatic FIM are separated. In particular, the matrix \mathbf{P} takes into account only the effect of the bistatic geometry while $\mathbf{J}_M(\tau, \nu)$ takes into account only the effect of the transmitted waveform.

The Cramér-Rao lower bounds are given by the inverse of the Fisher Information Matrix, therefore

$$\text{CRLB}(R_R) = \frac{[\mathbf{J}_B]_{2,2}}{[\mathbf{J}_B]_{1,1}[\mathbf{J}_B]_{2,2} - [\mathbf{J}_B]_{1,2}^2} \quad (3.18)$$

$$\text{CRLB}(V_B) = \frac{[\mathbf{J}_B]_{1,1}}{[\mathbf{J}_B]_{1,1}[\mathbf{J}_B]_{2,2} - [\mathbf{J}_B]_{1,2}^2} \quad (3.19)$$

From the last equation it is clearly apparent that the local accuracy in the bistatic case depends not only on the transmitted waveform but also on the bistatic geometry [Rih69], [Tsa97].

It is important to observe that the SNR at the receiver takes into account the energy loss due to propagation:

$$\text{SNR} \propto \frac{1}{R_R^2 R_T^2} \quad (3.20)$$

where $R_T = \sqrt{R_R^2 + L^2 + 2R_R L \sin \theta_R}$ is the range from transmitter to target.

It is clear that for $L=0$ the transmitter and the receiver are co-located and, from the last equations, it is clear that in this case the bistatic FIM coincides with the monostatic FIM.

The results derived in this Chapter can be used for defining a tool for evaluate the performance of a given monostatic or bistatic channel of the multistatic system and for design multistatic weighting coefficients for the detection process that will be described in the next Chapter.

3.2 Bistatic Cramér-Rao Lower Bounds for a burst of LFM pulses

Using equations (3.2) and the results showed in Section 1.7, after some algebra, it is possible to verify that, in the monostatic configuration, the FIM of a burst of LFM pulses is given by [Far09]

$$\mathbf{J}_M(\tau, \nu) = -2SNR \begin{bmatrix} -\frac{k^2 \pi^2 T^2}{3} & \frac{k \pi^2 T^2}{3} \\ \frac{k \pi^2 T^2}{3} & -\frac{\pi^2 T^2}{3} + \frac{\pi^2 T_R^2 (1 - N^2)}{3} \end{bmatrix} \quad (3.21)$$

Inverting (3.21), the monostatic CRLBs for the delay and the Doppler are given by:

$$\text{CRLB}(\tau) = \frac{3}{2\pi^2 T^2 k^2 SNR} \left[1 + \left(\frac{T}{T_R} \right)^2 \frac{1}{N^2 - 1} \right] \quad (3.22)$$

and

$$\text{CRLB}(\nu) = \frac{3}{2\pi^2 T_R^2 SNR (N^2 - 1)} \quad (3.23)$$

These results are in agreement with those obtained in [Dog07].

Using this result, combined with (3.16), it is possible to compare the monostatic and the bistatic Root Cramér-Rao Lower Bounds (RCRLBs). Figures 3.1-3.3 show the RCRLBs of range and velocity, both in the monostatic and bistatic case, obtained selecting $T=250\mu\text{sec}$, $T_R=1\text{msec}$, $B=1\text{MHz}$, $f_C=10\text{GHz}$ and $N=8$. In particular, Figure 3.1 shows the RCRLBs as a function of the receiver to target range R_R when $\theta_R=0$. While Figure 3.2 shows the results obtained choosing $\theta_R = -0.49\pi$. Figure 3.3 shows the RCRLBs as a function of the receiver look angle θ_R , both in the case of $R_R < L$ and $R_R > L$. All these figures have been obtained choosing $V_B=250\text{ m/sec}$, $L=50\text{km}$ and holding constant the SNR to 0dB. It is evident that, for all the parameter values we tested, the bistatic RCRLBs are always higher than the monostatic RCRLBs. Anyway when the distance from receiver to the target increases, the bistatic system behaves more and more as the monostatic one. As apparent from Figure 3.2, the effects of geometry are prominent where the target approaches the baseline, that is when $R_R \leq L$ and θ_R approaches $-\pi/2$. When the target is on the baseline, the RCRLBs tend to infinity.

In this case, the resulting delay is L/c and the radial velocity is zero, therefore resolution is totally lost and the RCRLBs tend to infinity. This can be appreciated by realizing that the echo arrives at the receiver at the same instant as the direct signal, independent of the target location, and the Doppler shift of a target crossing the bistatic baseline must be zero, because the transmitter-to-target range changes in an equal and opposite way to the target-to-receiver range, independent of the magnitude and direction of the target velocity. However, the effects of the bistatic geometry are less prominent when the distance to the target increases; in this case the bistatic system behaves more and more as a monostatic system.

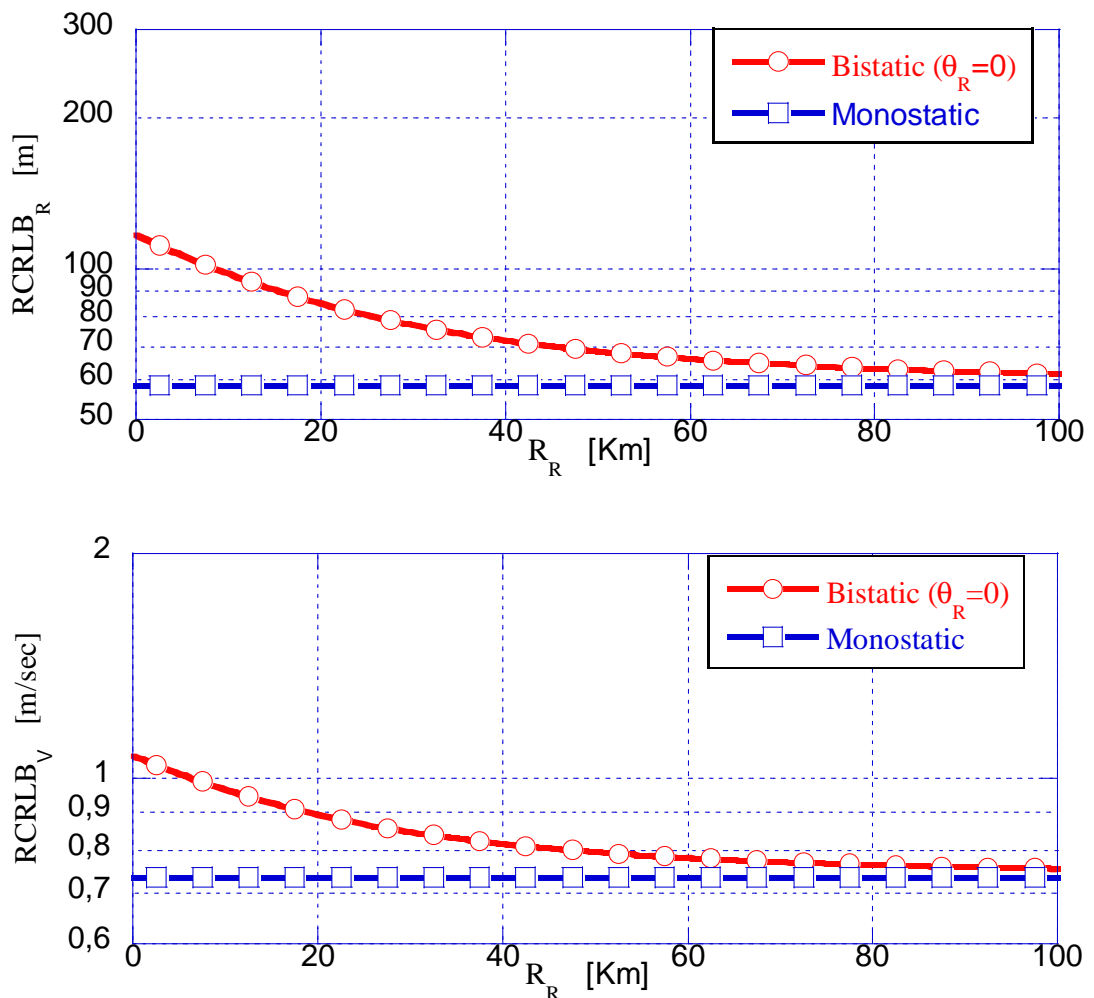


Figure 3.1 - RCRLB of Range and Velocity as a function of receiver to target range R_R , $\theta_R=0$; $L=50\text{km}$, $\text{SNR}=0\text{dB}$. The transmitted signal is a burst of LFM pulses.

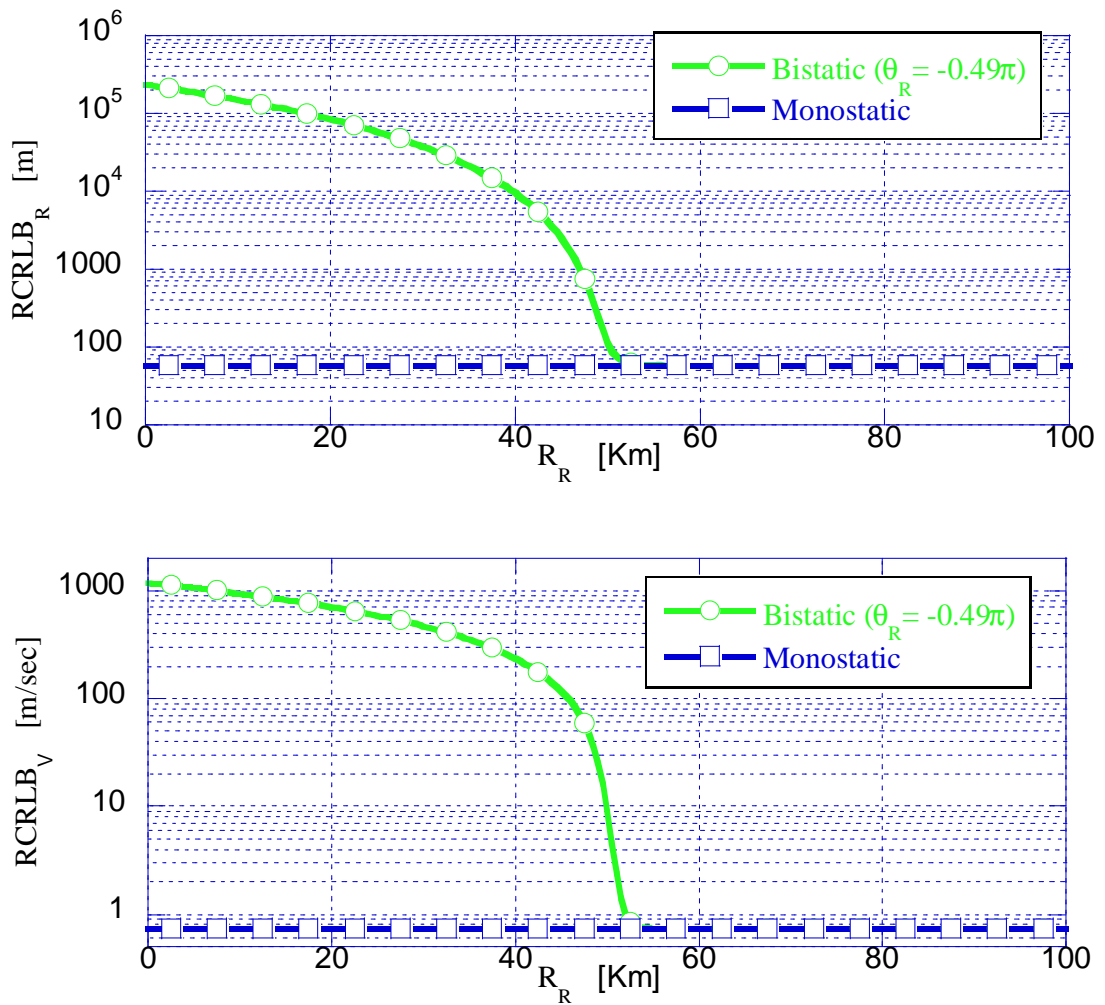


Figure 3.2 - RCRLB of Range and Velocity as a function of receiver to target range R_R , $\theta_R = -0.49\pi$; $L=50$ km, SNR=0dB. The transmitted signal is a burst of LFM pulses.

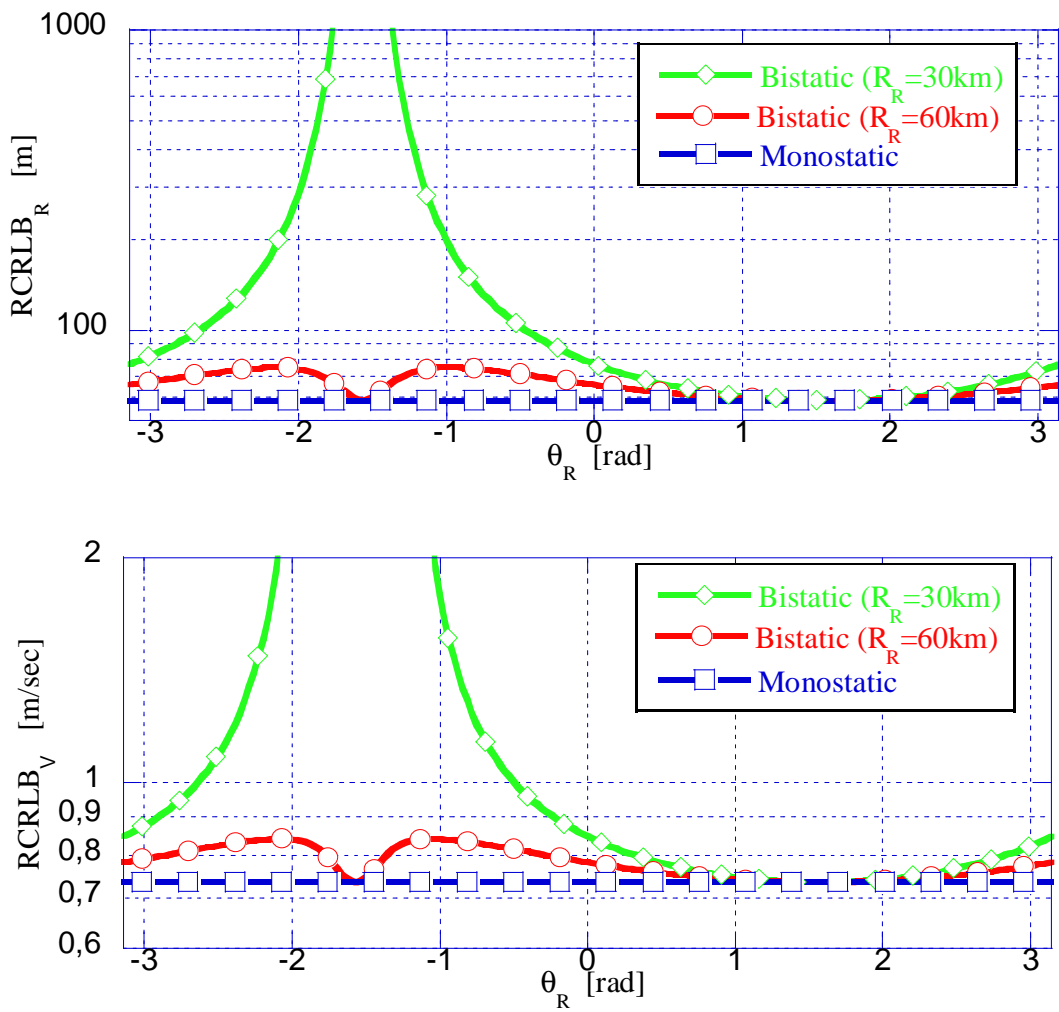


Figure 3.3 - RCRLB of Range and Velocity as a function of receiver look angle θ_R ; $L=50\text{km}$, $\text{SNR}=0\text{dB}$. The transmitted signal is a burst of LFM pulses.

3.3 Bistatic Cramér-Rao Lower Bounds for a SFM pulse

Exploiting the relation between the Ambiguity Function of a SFM pulse derived in Section 1.4 and the FIM in equation (3.2), it is possible to verify that the elements of the monostatic FIM are given by (see Appendix C for more details):

$$[\mathbf{J}_M]_{1,1} = 2SNR \frac{\beta^2 2\pi f_0}{T} [2\pi f_0 T + \sin(2\pi f_0 T) \cos(2\varphi)] \quad (3.24)$$

$$[\mathbf{J}_M]_{2,2} = 2SNR \frac{\pi^2 T^2}{3} \quad (3.25)$$

$$[\mathbf{J}_M]_{1,2} = [\mathbf{J}_M]_{2,1} = -2SNR \frac{2\beta \sin(\varphi)}{Tf_0} [\pi f_0 T \cos(\pi f_0 T) - \sin(\pi f_0 T)] \quad (3.26)$$

In the case $T = k/f_0$ ($k \in \mathbb{N}$) and considering that $\pi^2 k^2 / 3 \gg \sin^2(\varphi)$, the Root-CRLBs are approximated by

$$\text{RCRLB}(\tau) = \sqrt{\text{CRLB}(\tau)} \approx \frac{1}{\sqrt{2SNR}} \frac{1}{\pi B_c} \quad (3.27)$$

$$\text{RCRLB}(v) = \sqrt{\text{CRLB}(v)} \approx \frac{1}{\sqrt{2SNR}} \frac{\sqrt{3}}{T} \quad (3.28)$$

where $B_c \approx 2\beta f_0$ is the Carson's Bandwidth of $u(t)$. It is interesting to observe that, as of the burst of LFM pulses, $\text{RCRLB}(v)$ is inversely proportional to the time duration of the reference signal, while $\text{RCRLB}(\tau)$ is inversely proportional to its bandwidth. From this result it is interesting to observe that the best performance is obtained with modulating signals with high spectral content, such as rock music, and poorest performance is obtained with slow varying modulating signals, such as speech modulation.

As in the previous section, Figures 3.4 and 3.5 highlight the differences between monostatic and bistatic RCRLBs. In this case the RCRLBs are plotted as a function of the baseline length L and the angle θ_R .

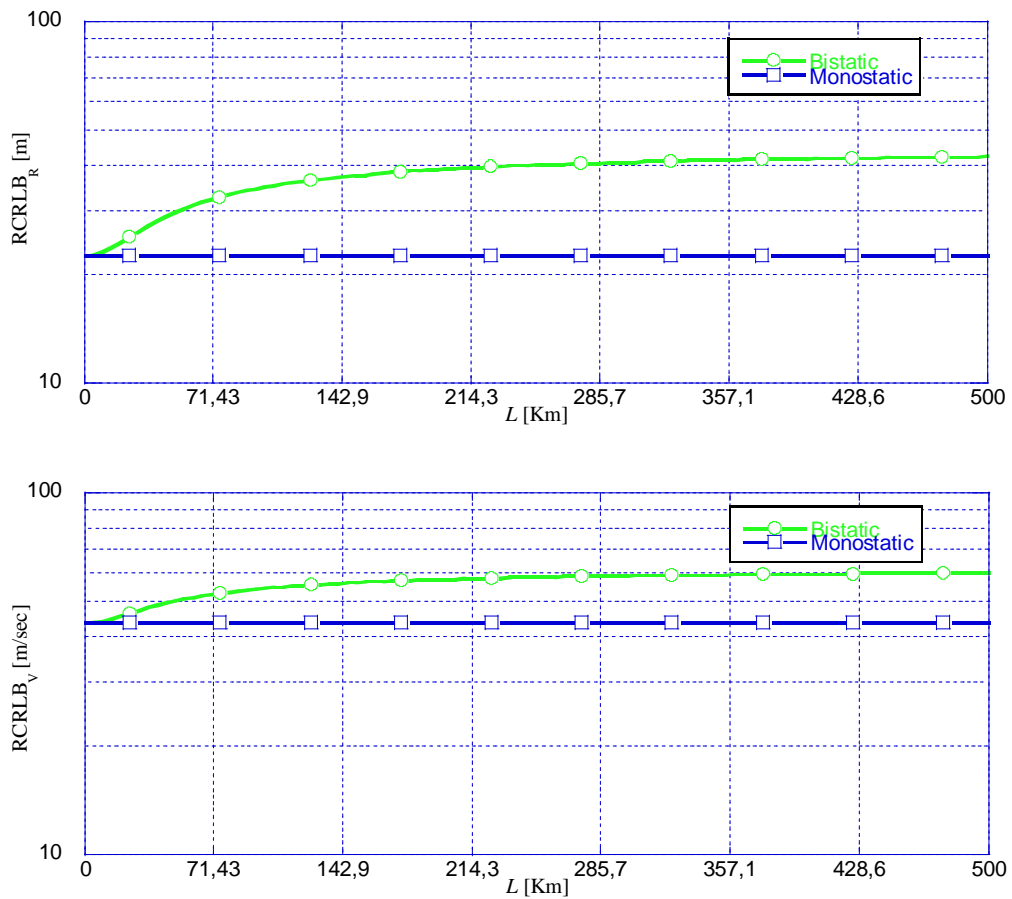


Figure 3.4 - RCRLBs as a function of the look angle θ_R ; $L=50\text{km}$, $R_R=30\text{Km}$, $V_B=250\text{m/sec}$. Sinusoidal Frequency Modulated Pulse, $f_0=15\text{kHz}$, $\beta=5$, $T=20/f_0$, $\varphi=\pi/2$, $f_C=100\text{MHz}$, $SNR=20\text{dB}$.

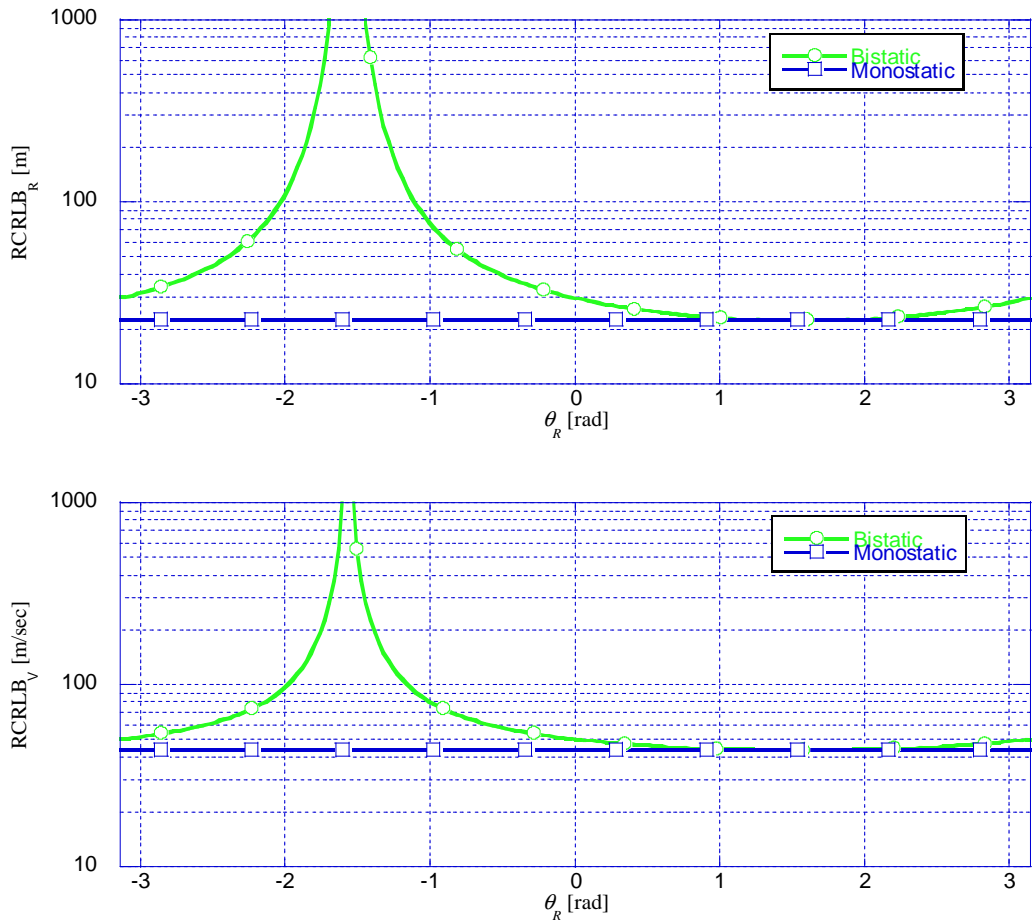


Figure 3.5 - RCRLBs as a function of the look angle θ_R ; $L=50\text{km}$, $R_R=30\text{Km}$, $V_B=250\text{m/sec}$, Sinusoidal Frequency Modulated Pulse, $f_0=15\text{kHz}$, $\beta=5$, $T=20/f_0$, $\varphi=\pi/2$, $f_C=100\text{MHz}$, $SNR=20\text{dB}$.

4 Multistatic Radar Systems

4.1 Introduction

Multistatic radars utilize multiple transmitters and receivers. Such systems differ from typical modern active radars since they consist of several different monostatic and bistatic channels of observation. Due to this spatial diversity, these systems present challenges in managing their operation as well as in usefully combining the data from multiple sources of information on a particular area of surveillance. The information gain, obtained through this spatial diversity, combined with some level of data fusion, can give rise to a number of advantages over both the individual monostatic and bistatic cases for typical radar functions, such as detection, parameter estimation, tracking and identification. As showed in the previous Chapters, the performance of each channel of the multistatic system heavily depends on the transmitted waveform and on the geometry of the scenario, that is, the position of receivers and transmitters with respect to the position of the target.

Exploiting the Monostatic and the Bistatic Cramér-Rao Lower Bounds, it is possible to calculate the channel performance of each TX-RX pair as a function of the target kinematic parameters. In particular, in Chapter, we exploit the results obtained in Chapter 3 to select the best channels of the multistatic system and to compute the rules for selecting the best weighting coefficients for fusing the signals from multiple receivers in order to improve the detection performance and the estimation accuracy of the kinematic parameters of the target.

We also introduce an optimization methodology for selecting only some channels for the network, independent of the adopted fusion rule. All the techniques described in this Chapter depend on the Fisher Information Matrix (FIM) which is itself dependent on the SNR, the AF and therefore on the geometry and the transmitted waveform. The described technique can serve as a guideline for future multistatic fusion rule development.

4.2 Optimal channel selection in a multistatic radar system

The CRLB study carried out on the bistatic geometry can be applied for the selection of the transmitter-receiver (TX-RX) pair in a multistatic radar system. We have seen that the

performance of each bistatic channel heavily depends upon the geometry of the scenario and the position of the target with respect to each receiver and transmitter. In this section we investigate the problem of optimally selecting the TX-RX pair, based on the information provided by the CRLB for the bistatic geometry of each bistatic channel. The best pair is defined as that exhibiting the lowest bistatic CRLB for the target velocity or range (or a combination of the two). These results can be used for the dynamical selection of the TX-RX signals for the tracking of a radar target moving along a trajectory in a multistatic scenario.

In our scenario we considered an area of dimension $L_x=20\text{km}$ and $L_y=20\text{km}$ and we placed 5 transmitters and 4 receivers in this area. In particular, we placed the transmitters at coordinates

$$\begin{aligned}
T^{(1)} &= (x_T^{(1)}, y_T^{(1)}) = (5\text{km}, 15\text{km}) \\
T^{(2)} &= (x_T^{(2)}, y_T^{(2)}) = (15\text{km}, 15\text{km}) \\
T^{(3)} &= (x_T^{(3)}, y_T^{(3)}) = (10\text{km}, 10\text{km}) \\
T^{(4)} &= (x_T^{(4)}, y_T^{(4)}) = (5\text{km}, 5\text{km}) \\
T^{(5)} &= (x_T^{(5)}, y_T^{(5)}) = (15\text{km}, 5\text{km})
\end{aligned} \tag{4.1}$$

and the receivers at coordinates

$$\begin{aligned}
R^{(1)} &= (x_R^{(1)}, y_R^{(1)}) = (5\text{km}, 10\text{km}) \\
R^{(2)} &= (x_R^{(2)}, y_R^{(2)}) = (10\text{km}, 15\text{km}) \\
R^{(3)} &= (x_R^{(3)}, y_R^{(3)}) = (10\text{km}, 5\text{km}) \\
R^{(4)} &= (x_R^{(4)}, y_R^{(4)}) = (15\text{km}, 10\text{km})
\end{aligned} \tag{4.2}$$

Therefore, there are $N_T \times N_R = 5 \times 4 = 20$ TX-RX pairs that we consider as independent bistatic channels. The 20 resulting pairs are listed and numbered in Table 4.1. We assume that each transmitter sends a burst of $N=8$ chirp pulses with a compression ratio $BT=250$ and a PRI of $T_R=10^{-3}$ sec. The carrier frequency of the system is $f_C=3 \cdot 10^8 / 2\pi$ Hz, as in the previous analysis. For each location in the analyzed area and for each of the 20 bistatic systems we calculated the RCRLBs of the target range and target velocity. In particular, we assumed that, in each point of the analyzed area, the target has a velocity vector aligned to the x axis and with intensity of 500 m/sec. The RCRLBs of the target range and target velocity are function

of the range from receiver to target R_R , the baseline L , the look angle of the receiver θ_R , the radial velocity V_a and the SNR . All these parameters depend on the configuration of the bistatic triangle, that is, on the coordinates of the target, the transmitter and the receiver. Bistatic geometry also affects the received echo power, because the path loss factor in this case is $(R_T R_R)^2$ [Sko01]. In particular the SNR can be written as

$$SNR = \frac{SNR_C \cdot (L_x^2 + L_y^2)^2}{(R_T R_R)^2} = \frac{SNR_C \cdot L^2}{(R_T R_R)^2} \quad (4.3)$$

where SNR_C is a constant parameter, i.e. the SNR in a reference point of the space. We assumed that $SNR_C=10\text{dB}$, that is, we assumed that if both the transmitter and the receiver are located in $(0, 0)$ and the target is located in (L_x, L_y) , then $SNR=10\text{dB}$.

Figures 4.1-4.4 are colour coded maps representing the $RCRLB_B$ of the target range and of the target velocity in each point of the analyzed area. In particular, Figs. 4.1 and 4.3 represent the $RCRLB_B$ of the target range, measured in dB, for the first and 5th bistatic systems; while Figures 4.2 and 4.4 represent the $RCRLB_B$ of the target velocity, in dB, for the same bistatic systems. As apparent from the results, the $RCRLB$ of each bistatic channel is strongly related to the bistatic geometry. It is clear that the effects of geometry factors are more prominent as the target approaches the baseline, that is, when $R_R \leq L$ and the receiver look angle θ_R approaches $-\pi/2$. The effects of the bistatic geometry are less noticeable when the distance to the target increases; in this case the bistatic system behaves more and more as a monostatic system. Therefore, the performance of each bistatic system is strongly related to the configuration of the bistatic triangle, that is, to the positions of the transmitter, the receiver and the target. It is clear that using different transmitting and receiving systems, the target can be seen by different bistatic configurations; therefore, knowing the coordinates of each transmitter and each receiver of the whole system, it is possible to calculate, for each point of the analyzed area, which is the transmitter-receiver pair having the best performances, that is the minimum $CRLB_B$.

Figures 4.5 and 4.6 show the transmitter-receiver pair which has the minimum $RCRLB_B$ for each point of the analyzed area for range and velocity estimation respectively. The scale of these figures is quantized into 20 levels, each of which is associated with one of the 20 bistatic systems listed in Table 1. Figures 4.7 and 4.8 show the minimum $RCRLB$ of the

target range and the target velocity, respectively, that is the value of the RCRLB which is provided by the transmitter-receiver pair which has the minimum RCRLB.

It is useful to observe that the values of the CRLBs depend on the true values of SNR , but the choice of the best channel does not. It depends only on the variation of the SNR as function of the geometry. Similar conclusions can be drawn on the target velocity V_B , supposed that it is the same in each point of the considered area.

Pair 1	$T^{(1)}-R^{(1)}$	Pair 11	$T^{(3)}-R^{(3)}$
Pair 2	$T^{(1)}-R^{(2)}$	Pair 12	$T^{(3)}-R^{(4)}$
Pair 3	$T^{(1)}-R^{(3)}$	Pair 13	$T^{(4)}-R^{(1)}$
Pair 4	$T^{(1)}-R^{(4)}$	Pair 14	$T^{(4)}-R^{(2)}$
Pair 5	$T^{(2)}-R^{(1)}$	Pair 15	$T^{(4)}-R^{(3)}$
Pair 6	$T^{(2)}-R^{(2)}$	Pair 16	$T^{(4)}-R^{(4)}$
Pair 7	$T^{(2)}-R^{(3)}$	Pair 17	$T^{(5)}-R^{(1)}$
Pair 8	$T^{(2)}-R^{(4)}$	Pair 18	$T^{(5)}-R^{(2)}$
Pair 9	$T^{(3)}-R^{(1)}$	Pair 19	$T^{(5)}-R^{(3)}$
Pair 10	$T^{(3)}-R^{(2)}$	Pair 20	$T^{(5)}-R^{(4)}$

Table 4.1 - Analyzed bistatic systems.

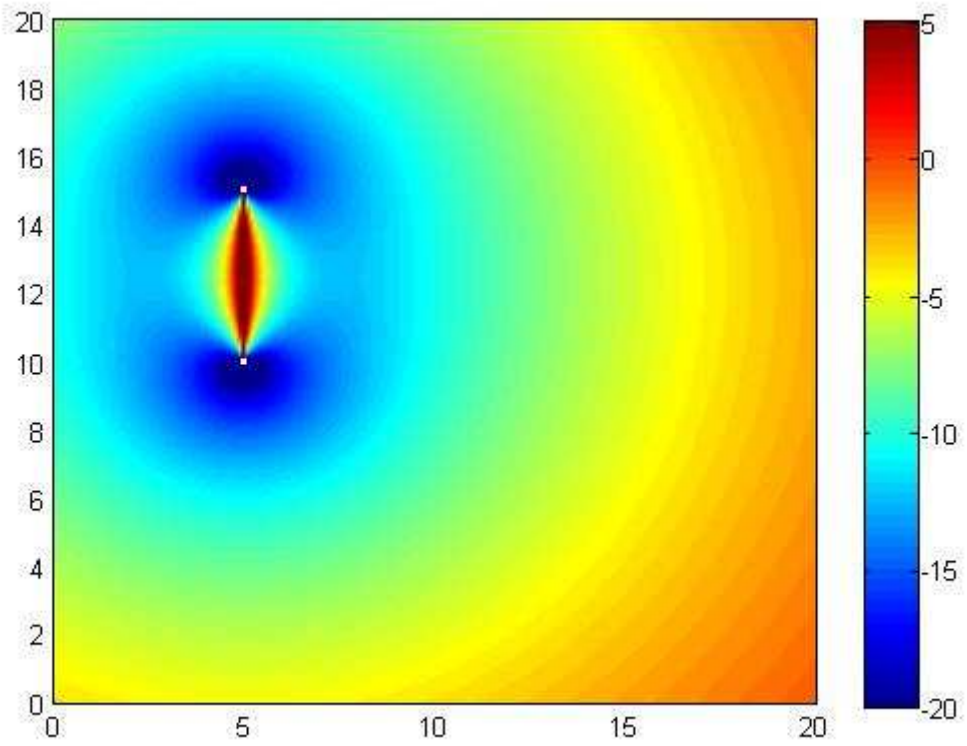


Figure 4.1 - Bistatic RCRLB of the target range [dBm]. *Pair 1.*

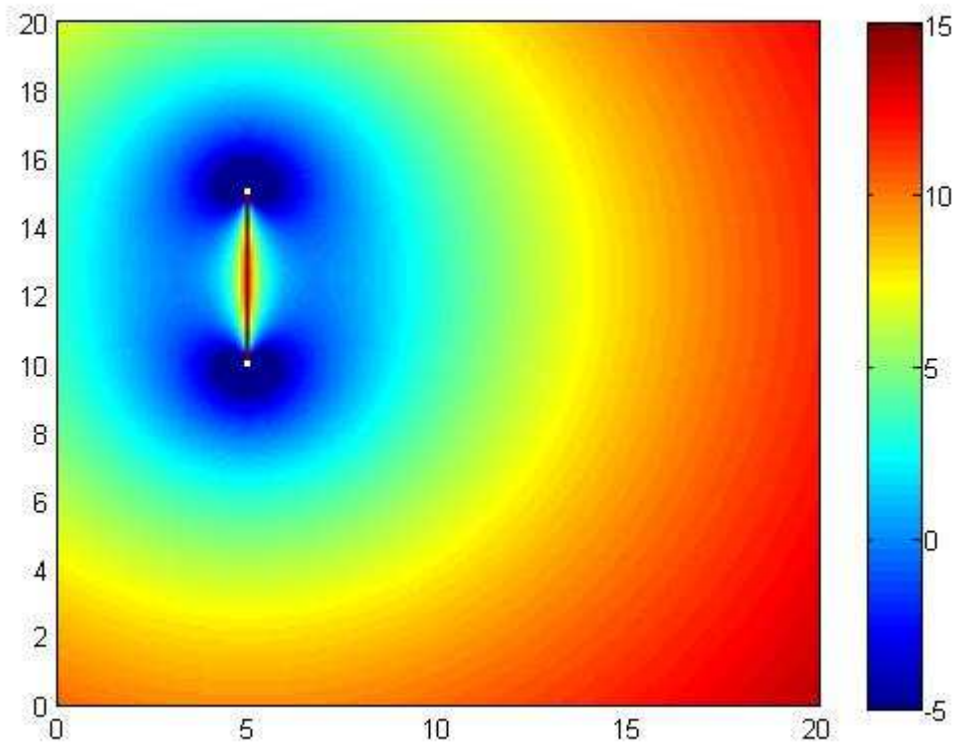


Figure 4.2 - Bistatic RCRLB of the target velocity [dBm/sec]. *Pair 1.*

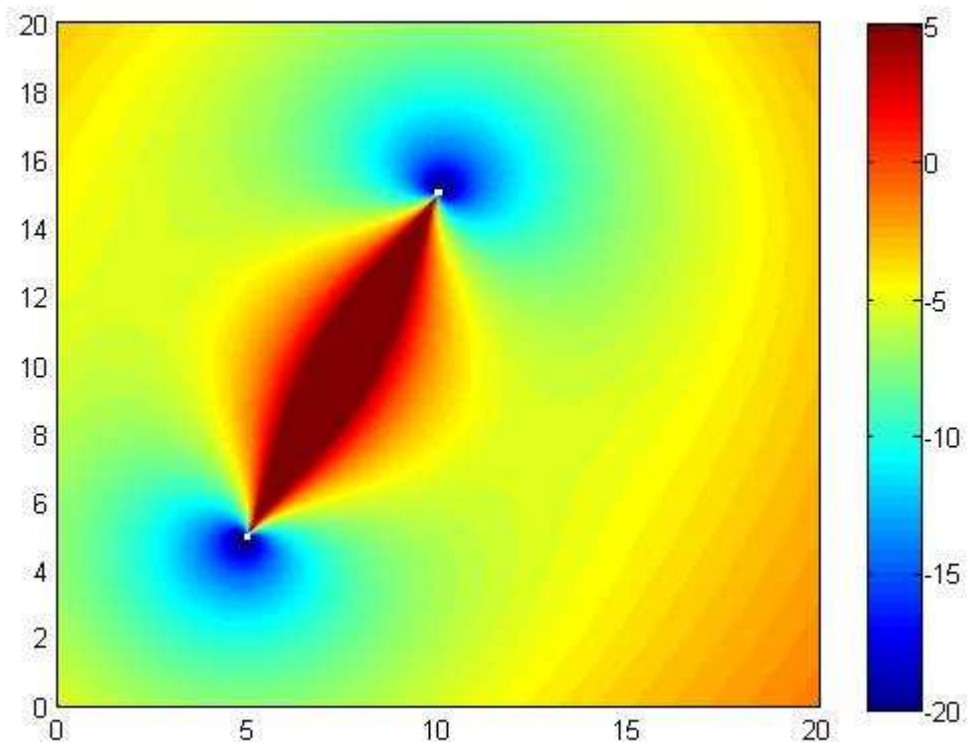


Figure 4.3 - Bistatic RCRLB of the target Range [dBm]. *Pair 5*.

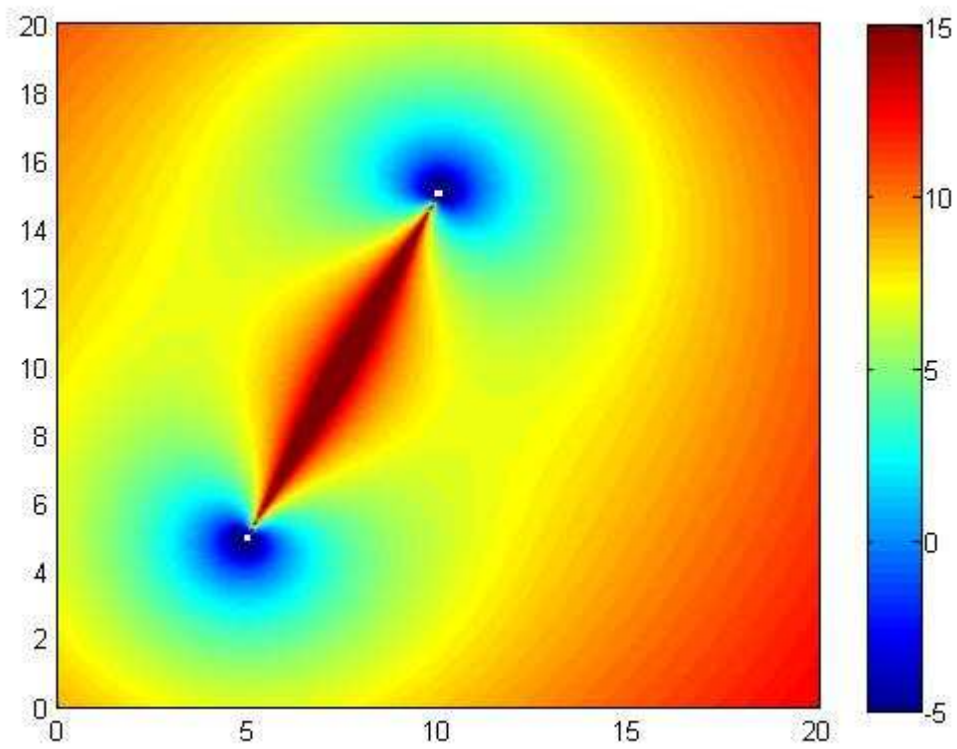


Figure 4.4 - Bistatic RCRLB of the target velocity [dBm/sec]. *Pair 5*.

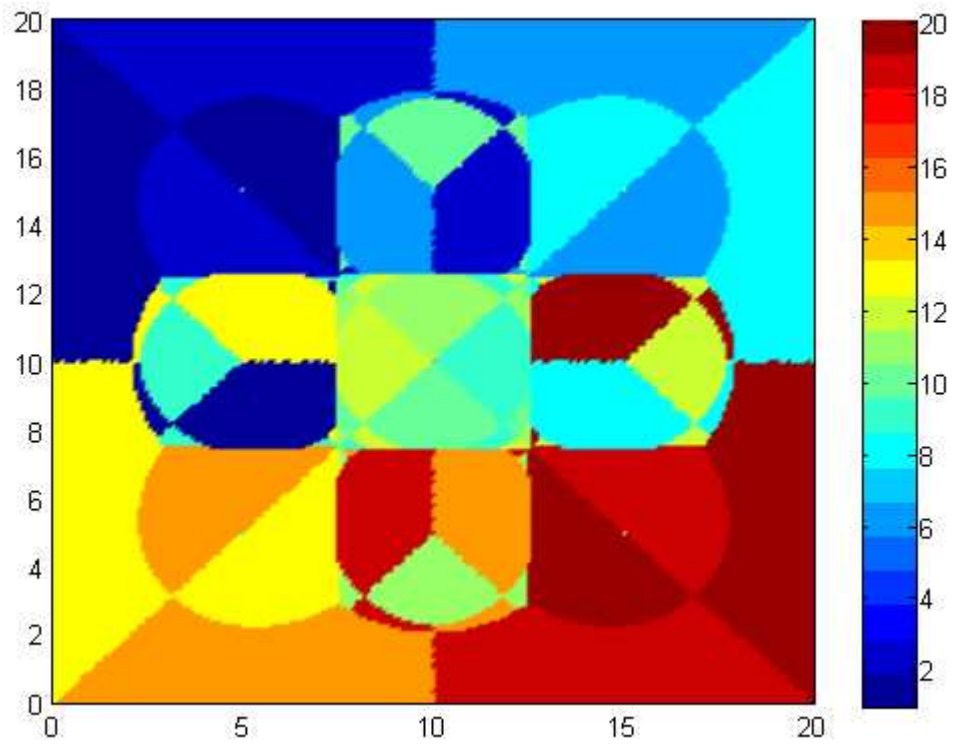


Figure 4.5 - Optimum pair map for target range estimation.

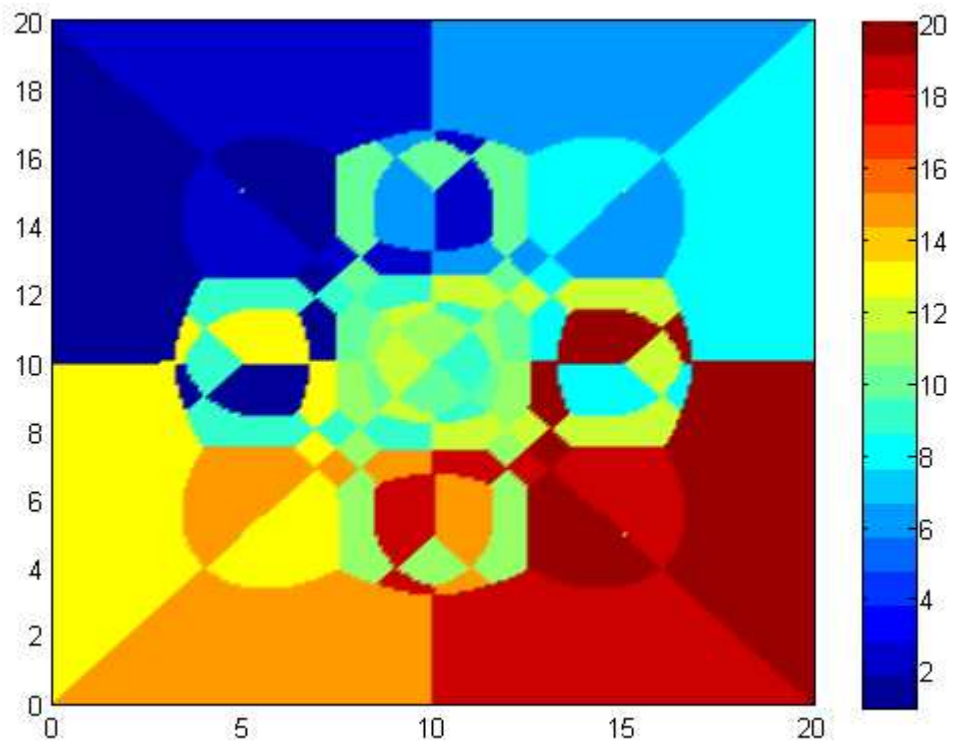


Figure 4.6 - Optimum pair map for target velocity estimation.

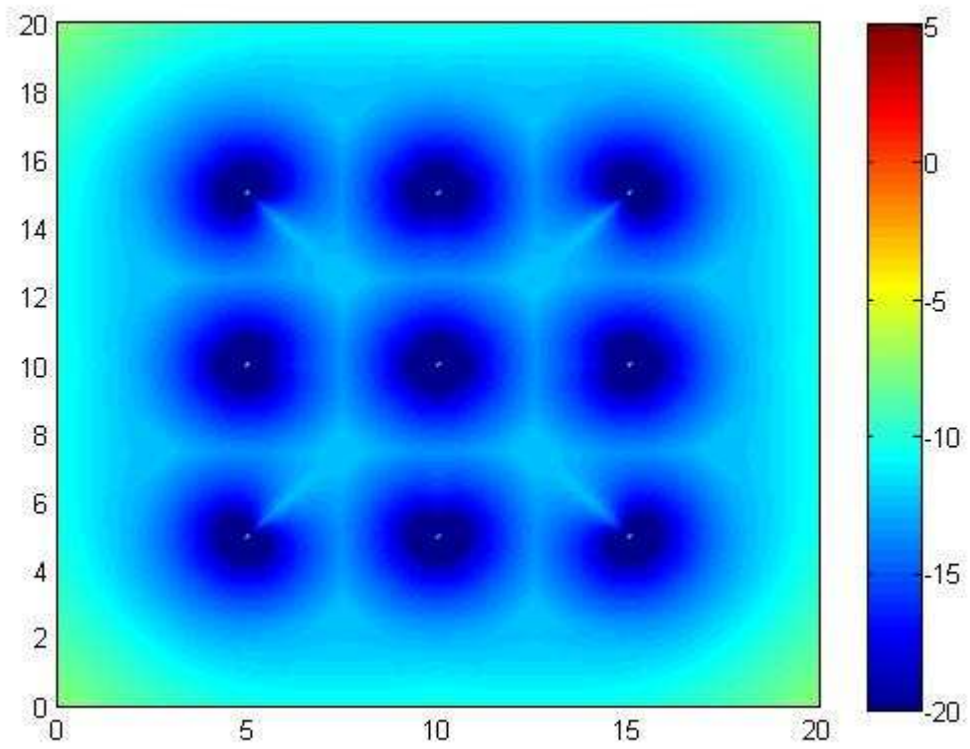


Figure 4.7 - Minimum RCRLB of the target range [dBm].

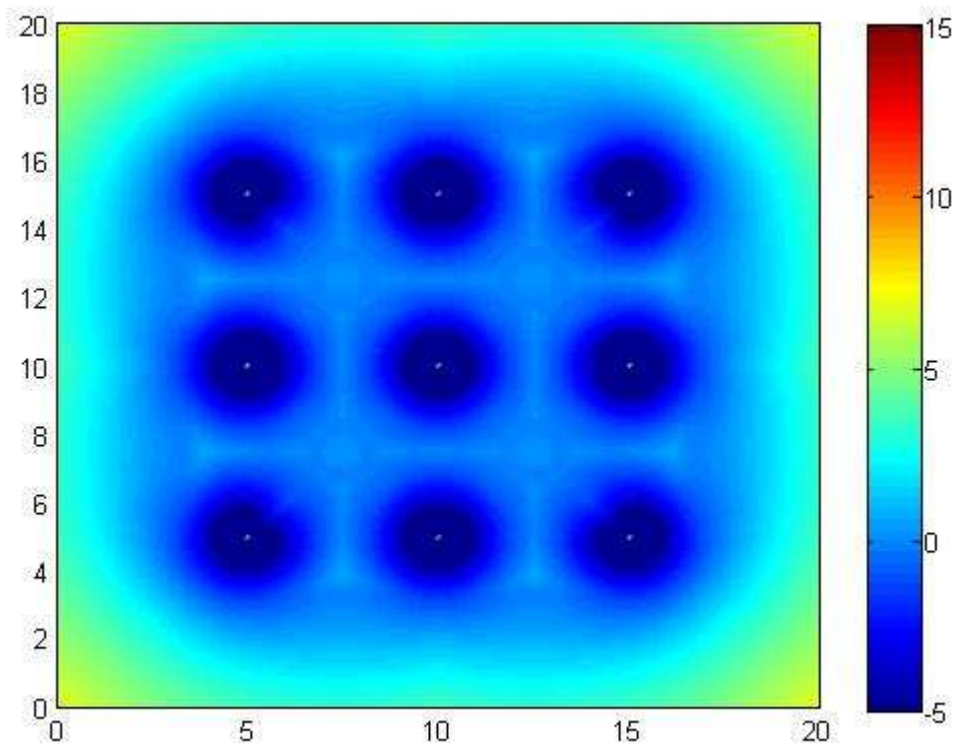


Figure 4.8 - Minimum RCRLB of the target velocity [dBm/sec].

4.3 Optimization algorithm

The optimal approach for a multistatic radar system would be central-level track processing, that is, to send all observations from the sensors to a fusion centre, where the observations are jointly processed.

This approach has two major disadvantages:

- 1) the amount of input measurement data to the fusion centre may be very high;
- 2) the observations from the sensors with the worst accuracy and resolution can significantly degrade the resolution of the whole systems.

This second problem is maybe the most important. There are studies that show that the best performance of the fused estimate in a multisensor system occurs when the sensors have similar accuracy and resolution [Azi07].

If accuracy and resolution vary widely, there is a risk that the fused track performs only marginally better, or even worse, than the track with the best quality estimate.

As an example, let consider the case of a target which is close to the baseline joining one of the transmitter and one of the receiver of the multistatic system.

In this case the range and Doppler resolution can be badly degraded, no matter what the radar waveform is. This can be appreciated by realising that the echo arrives at the receiver at the same instant as the direct signal, independent of the target location, and the Doppler shift of a target crossing the bistatic baseline must be zero, because the transmitter-to-target range changes in an equal and opposite way to the target-to-receiver range, independent of the magnitude and direction of the target velocity. In this case, resolution is totally lost and therefore the observation from this transmitter-receiver pair could hardly degrade the resolution of the whole multistatic radar system [Azi07], [Gre10].

This section proposes an optimization algorithm that, in a generic multistatic scenario and independent of the adopted fusion technique, specifies what channels should be discarded and what channels should be considered during the fusion process.

Using this algorithm, only a subset of data are communicated to the fusion centre, more specifically only from those sensors exhibiting the best performance in terms of estimation accuracy of the target parameters.

In the most general case, the multistatic scenario is the one pictorially depicted in Figure 4.9, where there are M transmitter and N receivers, co-located or not, surveying a common coverage area. It is supposed that a set of orthogonal waveform is transmitted, where

orthogonality is assumed to be maintained for any Doppler-delay shift. With proper design, transmit-receive paths can be separated, so that each sensor can receive echoes due the signals generated by all the transmitters and can select the transmitted signal of interest. In this way, the multistatic system can be considered as consisting of NM different monostatic and bistatic channels of observation.

The proposed optimization algorithm exploits the results obtained in the previous Chapter to approach the problem of optimally selecting the channels to be used by the fusion process. This algorithm is divided in two steps. In the first step, each of the N receivers of the network selects one of the M transmitters in order to obtain the best performances in terms of estimation accuracy of the target range and/or velocity. While, in the second step, after ranking the so obtained N channels from the worst to the best, where the best is the one that exhibits the lowest bistatic CRLB, only the first $N' \leq N$ are selected for the fusion process.

In the following, with the help of an illustrative example, we describe in detail how the optimization algorithm works. In the first step of the optimization process, each receiver selects the best transmitter on its own. In a multistatic network consisting of M transmitters and N receivers for each receiver there are M different channels. In the case that the considered receiver is colocated with one of the transmitter, there are $M-1$ bistatic channels and 1 monostatic channel.

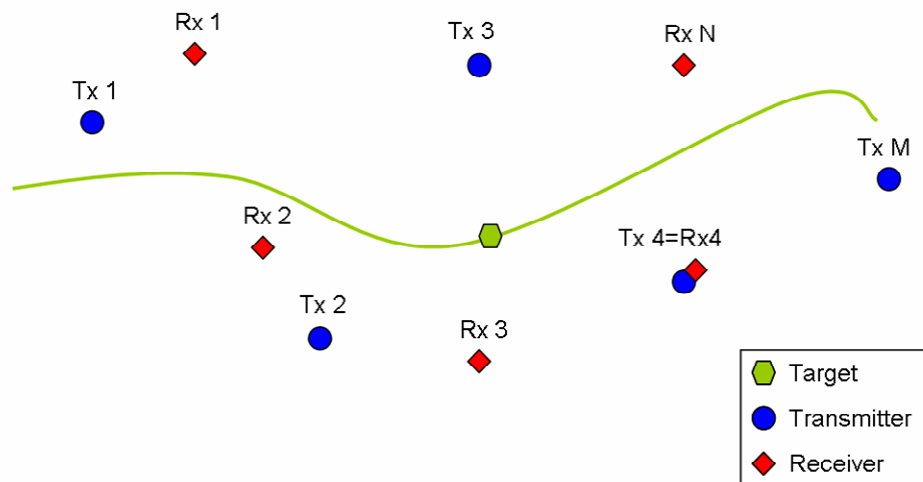


Figure 4.9 - Generic Multistatic Scenario

As an example, let consider a surveillance map of dimension $L_x=20\text{km}$ and $L_y=20\text{km}$ where there are seven transmitters placed at coordinates $T^{(1)}=(13.9 \text{ km},15.9 \text{ km})$, $T^{(2)}=(6.3 \text{ km}, 3.7 \text{ km})$, $T^{(3)}=(19 \text{ km},9.8 \text{ km})$, $T^{(4)}=(0.7 \text{ km},8.9 \text{ km})$, $T^{(5)}=(8.8 \text{ km}, 12.9 \text{ km})$, $T^{(6)}=(7.6 \text{ km}, 14.2 \text{ km})$, $T^{(7)}=(15.3 \text{ km}, 15.1 \text{ km})$ and the receiver is co-located with the first transmitter. In this example it is supposed that the transmitters send orthogonal signals with the same power and characterized by the same AF. Therefore, the different performances among the channels depend only on the propagation path loss and the configuration of the bistatic geometry. For each point of the analysed area, evaluating the performance of each bistatic channel, it is possible to select the transmitter with the best performance, that is, the one with the lowest CRLB on the target range and velocity estimation accuracy.

Figures 4.10 (a) and (b) show, in a colour coded map, the transmitter to be selected in order to provide the minimum CRLB for each point of the analysed area for range and velocity estimation, respectively. The color-map of these figures is clustered into 7 colours, each of which is associated with one of the 7 transmitters. It is apparent, that the results are very similar, but it is also possible to build a cost function using a weighted combination of the two CRLB. Figures 4.11 (a) and (b) show the minimum Root of the CRLB (RCRLB) of the target range and the target velocity, respectively, that is the value of the RCRLB which is provided by the transmitter-receiver pair which has the minimum RCRLB.

From this example, it is apparent that each receiver knows, for each point of the surveillance map, which is the transmitter to be selected in order to meet the best performance. Therefore, as pictorially shown in Figure 4.12, based upon the actual estimate of the target position, each receiver can dynamically select the signal of the best transmitter and discard the signals transmitted by the other sensors. Doing so, only N of the MN possible channels are selected for the fusion process.

Even so, from Figures 4.11 (a) and (b) it is apparent that, for some points of the surveillance map, the best performance that a receiver can achieve could be poor. This is only due to the geographical distribution of the sensors in the multistatic system but, for the reasons previously described, this could be a problem for the fusion process.

This problem can be solved by selecting a subset of channels among the N previously obtained. In particular, in the second step of the optimization algorithm, the N channels are ranked from the worst to the best and only the first N' are selected for the fusion process. The number N' could be also dynamically changed by the fusion process in order to meet pre-specified performance goals.

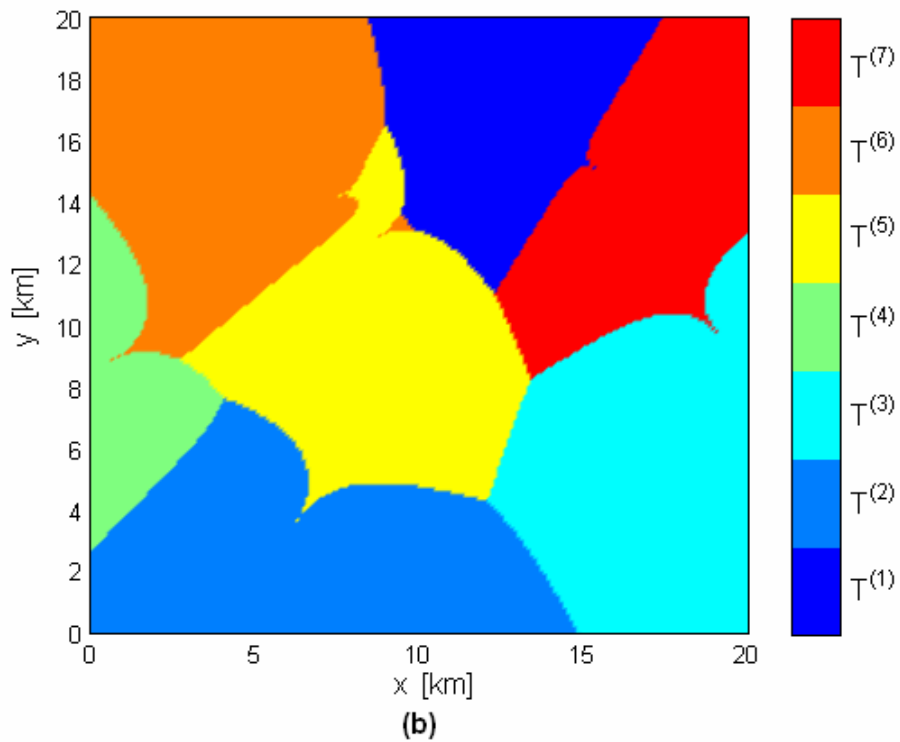
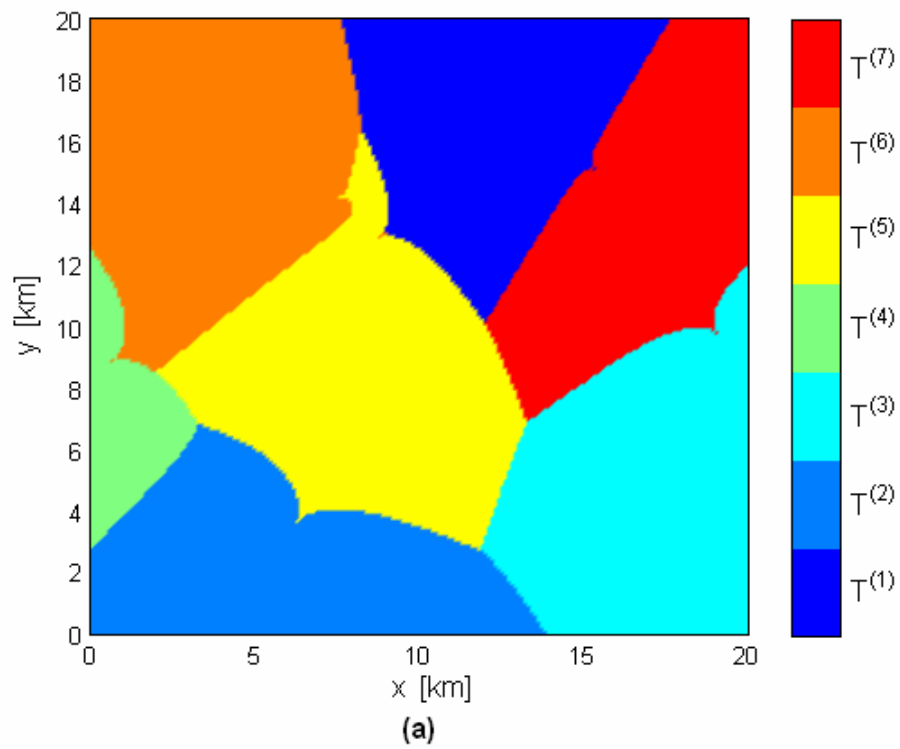


Figure 4.10 - (a) Optimum Transmitter for target range estimation; (b) Optimum Transmitter for target velocity estimation. The receiver is co-located with $T^{(1)}$.

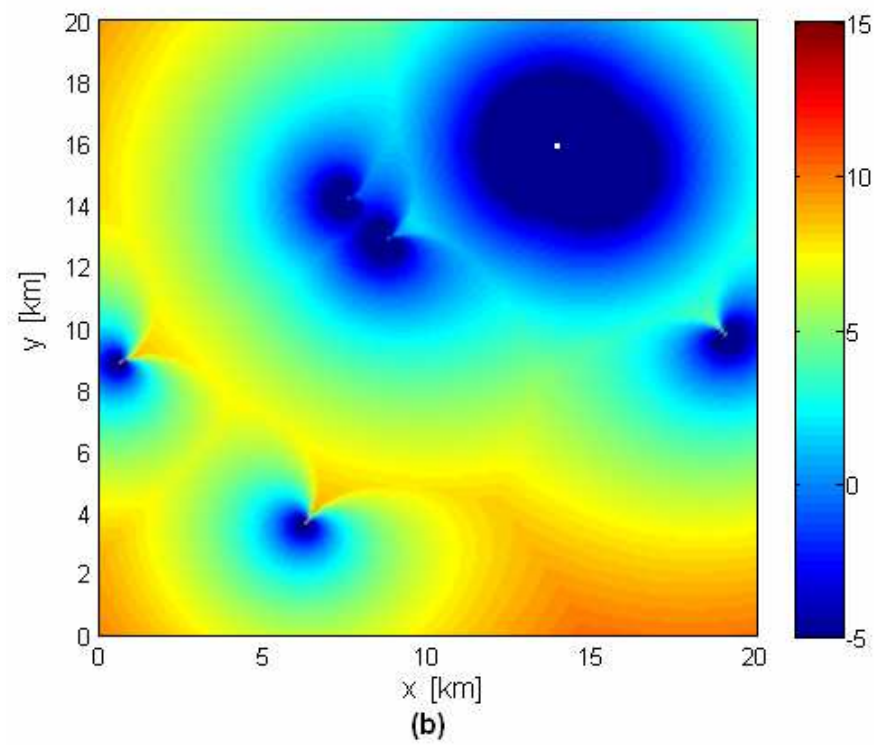
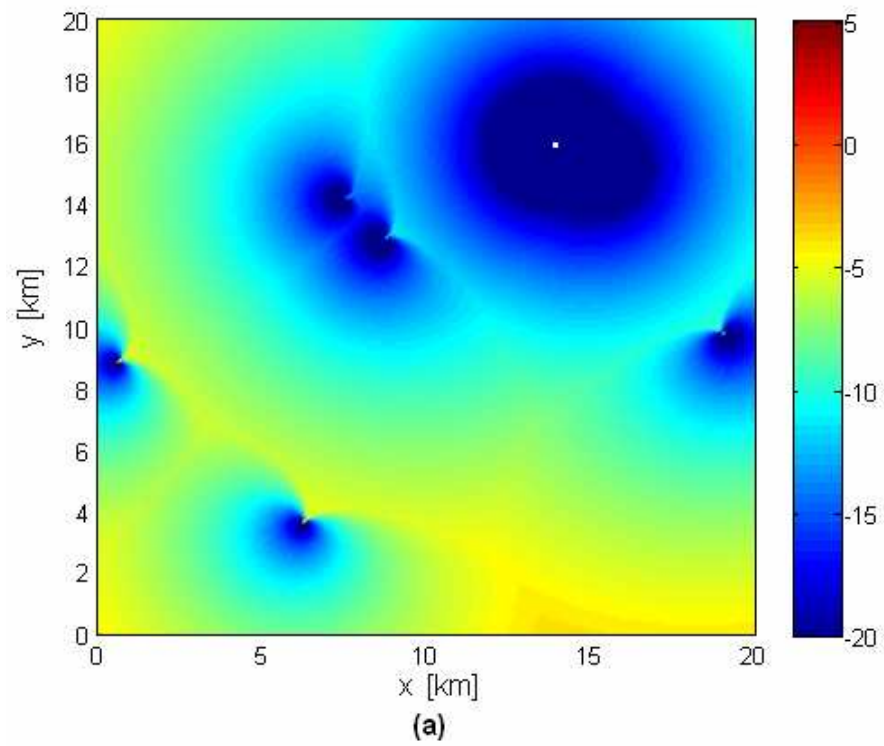


Figure 4.11 - (a) Minimum RCRLB of the target range [dBm]; (b) Minimum RCRLB of the target velocity estimation [dBm/sec].

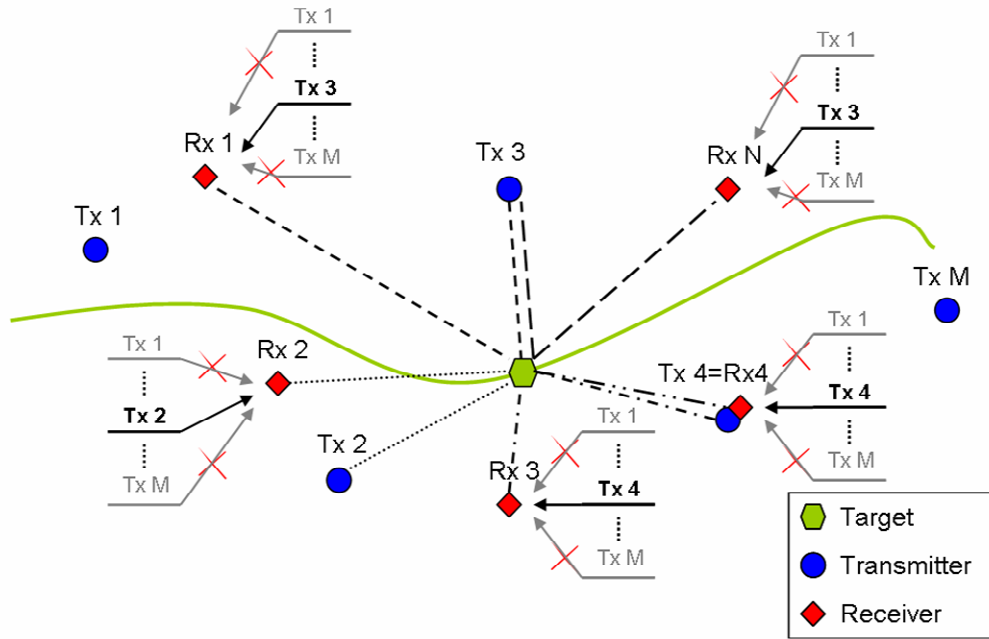


Figure 4.12 - Optimum transmitter selection.

4.4 Optimum weighting rule for multistatic detection

This section deals with the description of a coherent multistatic system where the rule for selecting the weighting coefficients is computed exploiting the results obtained in Chapter 3. For ease of notation, the described system is composed of one transmitter and N receivers. In the case of multiple transmitters, it is supposed that it is possible to separate each transmitter-receiver path so that each receiver can select the transmitted signal of interest. In this way, the multistatic system is composed by MN channels of observation, where M is the number of transmitters. The only difference with the case of a single transmitter is only on the number of channels, but the algorithm remains the same. The multistatic receiver that will be implemented refers to a centralized nomenclature where the data at each receiver are first collected by a central processor and then jointly combined for the detection.

In particular, the central processing of the analyzed system will exploit part of the results described in Section 4.3. In particular, the optimization algorithm described in Section 4.3 can be viewed as a fusion algorithm that uses hard weighting coefficients, that is, weights that can assume only two values: zero in the case of a bad channel and 1 in the other case. On the other hand, the weighting coefficients of the central processor described in this section are soft, that

is they can assume values that belongs to the range $[0,1]$ depending on the information gained by the Fisher Information Matrix as described in Chapter 3.

Figures 4.13 and 4.14 show the block diagram of the multistatic receiver that will be described in this Section. From Figure 4.13, it is apparent how the detection processing is divided in two parts: the local processing at each receiver and the central processing at the central processor. Figure 4.14 shows the flow diagram of the signal processing at the central processor. As showed in Figure 4.13, the flow diagram of each receiver of the multistatic network is the most adopted in modern coherent radar system where, after the classical processing to down-shift the received signal to the base band, the receiver performs a range – Doppler matched filtering. In the case of multiple transmitters, the range – Doppler matched filtering consists in a bank of filters, each of which is matched to the waveform emitted by each transmitter.

As previously discussed, the performance of each receiver depends on the transmitted waveform but unfortunately is also heavily sensitive to the geometry, that is, the position of the receiver and the transmitter with respect to the position of the target. Using the results of Chapter 3 and for a fixed geometry of the simulated scenario, it is possible to derive easily the CRLBs of each channel and therefore its performance. Moreover, it is clear that, each receiver of the multistatic system has its own local geometry, that is, each receiver knows at what range from its location there is a target and the target speed straight towards or away from the receiver. The role of the central processor is therefore to exploit the information gained by the knowledge of the geometry of the network (the position of each transmitter and each receiver) to convert the local coordinates of the receivers into global coordinates.

The information about range and radial velocity from each receiver are therefore converted into information about the target state, that is, the real position of the target and the velocity components along the axes of the reference coordinates system. Moreover, another important role of the central processor is to evaluate for each point of the global surveillance map, that is for each cell (x,y,V_x,V_y) , the performance that can be gained for each path of the multistatic system. Therefore the role of the central processor is to generate a global coordinates detection map exploiting the information about the geometry of the multistatic network.

Let's describe now each block of the flow diagram of Figure 21.

The block buffer indicates that, for each scan, the central processor stores the local range-Doppler maps of each receiver. In particular, each local map can be viewed as a two dimensional matrix whose elements are the samples at the output of the matched filter of each receiver.

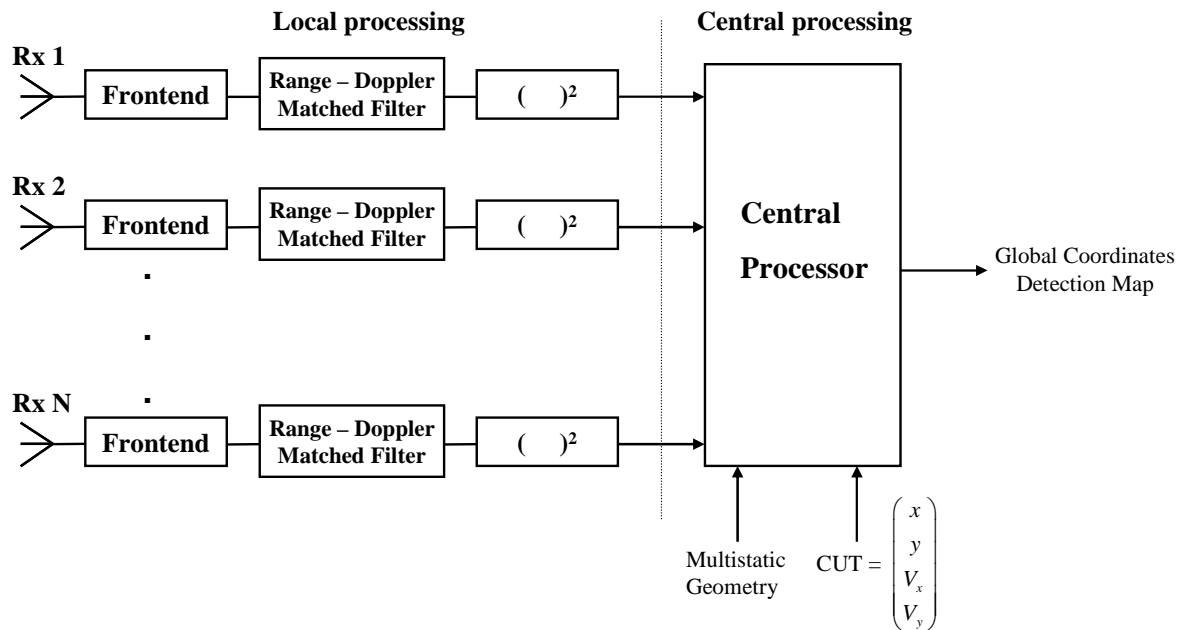


Figure 4.13 - Flow Diagram of the multistatic detector.

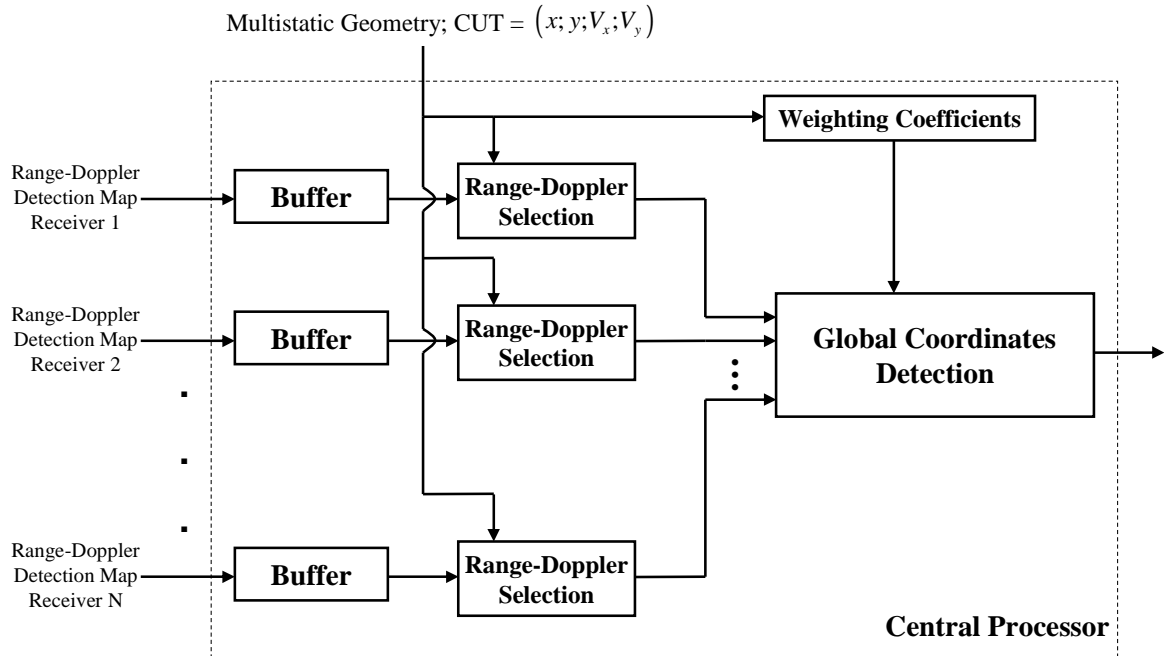


Figure 4.14 - Flow Diagram of the Central Processor.

The central processor scans each point of the global surveillance area, that is each value that can be assumed by the vector (x, y, V_x, V_y) .

Once fixed the cell under test, that is the vector (x, y, V_x, V_y) , and knowing the geometry of the multistatic system, the role of the block range-Doppler selection is to select the corresponding range-Doppler cell of each receiver.

In particular, let indicate with

$$\mathbf{x} = (x, y) \quad (4.4)$$

the global coordinates of the target that is supposed to be detected and with

$$\mathbf{V} = (V_x, V_y) \quad (4.5)$$

the vector of its possible velocity components.

Indicating with

$$\mathbf{x}_T = (x_T, y_T) \quad (4.6)$$

the global coordinates of the transmitter and with

$$\mathbf{x}_R^{(i)} = (x_R^{(i)}, y_R^{(i)}) \quad i=1, \dots, N \quad (4.7)$$

the global coordinates of the i-th receiver it is easy to verify that the range cell to be probed for the i-th receiver is

$$R_R^{(i)} = |\mathbf{x} - \mathbf{x}_R^{(i)}| \quad (4.8)$$

while the Doppler cell to be probed is

$$V_B^{(i)} = \frac{\mathbf{x}_I^{(i)} \mathbf{V}^T}{|\mathbf{x}_I^{(i)}|} \quad (4.9)$$

where

$$\mathbf{x}_I^{(i)} = \frac{L^{(i)} \mathbf{x} + R_R^{(i)} \mathbf{x}_T + R_T \mathbf{x}_R^{(i)}}{L^{(i)} + R_R^{(i)} + R_T} - \mathbf{x} \quad (4.10)$$

$$L^{(i)} = |\mathbf{x}_T - \mathbf{x}_R^{(i)}| \quad (4.11)$$

$$R_T = |\mathbf{x} - \mathbf{x}_T| \quad (4.12)$$

$$\vartheta_R^{(i)} = \cos^{-1} \left(\frac{(R_R^{(i)})^2 + (L^{(i)})^2 - (R_T)^2}{2R_R^{(i)}L} \right) - \frac{\pi}{2} \quad (4.13)$$

Using equations (4.8) and (4.9), for each point (x, y, V_x, V_y) of the surveillance map, the central processor is able to select the corresponding range-velocity cell of each receiver.

Thus, the problem of detecting a target signal in a fixed resolution cell of the surveillance map can be posed in terms of the following binary hypotheses test:

$$\begin{cases} r_i = \alpha_i c_i + n_i & H_1 \\ r_i = n_i & H_0 \end{cases} \quad i=1, \dots, N \quad (4.14)$$

where the sample r_i is the output of the filter matched to the normalized transmitted signal for the i -th receiver in the range-velocity cell corresponding to the point (x, y, V_x, V_y) .

Note that if the transmitted signal is a burst of pulses, the sample r_i is the output of the filter matched to the entire burst. In the signal model in eq. (4.14), n_i is the additive noise at the i -th sensor; it is modelled as a zero-mean complex Gaussian variable, in short $n_i \sim CN(0, \sigma^2)$. The samples n_i are assumed to be independent from channel to channel and identically distributed. The parameter α_i accounts for the channel propagation effect and the target radar cross section. We considered the case in which the amplitude α_i is a random variable. It depends on the target bistatic RCS of the i -th bistatic angle. This, together with the mentioned features of the multistatic geometry, justifies the assumption that the α_i s are mutually independent random quantities. With regard to the marginal PDFs, α_i is a zero-mean complex Gaussian variable with variance σ_i^2 varying from path to path $\alpha_i \sim CN(0, \sigma_i^2)$. In particular the Signal to Noise power Ratio at the input of the i -th channel is defined as

$$SNR_i = \frac{\sigma_i^2}{\sigma^2} = \frac{Const}{(R_T^{(i)} R_R^{(i)})^2} \quad (4.15)$$

and, as mentioned, is inversely proportional to the path loss factor $(R_T^{(i)} R_R^{(i)})^2$ due to propagation where, $R_T^{(i)}$ and $R_R^{(i)}$ are the range from transmitter to target and the range from receiver to target for the i -th channel, respectively. The parameter c_i , that appears in eq. (4.14) is a complex number whit absolute value lower than or equal to one which accounts for the other effects of propagation and scattering along the i -th path. The meaning of c_i will be discussed later on, for the moment let consider the case in which $c_i=1$. Under this assumption and considering that the amplitude α_i and the noise n_i are independent, the observation r_i is a zero-mean complex Gaussian variable under both hypotheses. Therefore, it is possible to write:

$$\begin{cases} r_i \sim CN(0, \sigma_i^2 + \sigma^2) & H_1 \\ r_i \sim CN(0, \sigma^2) & H_0 \end{cases} \quad i=1, \dots, N \quad (4.16)$$

Hence, by exploiting the independence of individual likelihoods in each channel, it is possible to verify that the Neyman-Pearson decision test develops into the following form [Dad86],[Con83]:

$$\sum_{i=1}^N p_i |r_i|^2 \underset{H_1}{\overset{H_0}{\leq}} \lambda \quad (4.17)$$

where

$$p_i = \frac{SNR_i}{1 + SNR_i} \quad (4.18)$$

Note that the weight p_i are non negative and are an increasing function of SNR_i , therefore the central processor emphasizes those channels along which the SNR s are the highest. Note that the receiver to implement the given test, depending on cell under test of the surveillance map, needs to continually update the weights, which are themselves dependent, through SNR_i , on the distances from the transmitter to the target and from the target to the receiver.

Consider now the case in which, under the H_1 hypothesis, c_i in eq. (4.14) is a complex random variable. This simple assumption has been done in order to model the effects of the bistatic geometry along the i -th path. In particular we generated c_i as

$$c_i = X(\tau_i, \nu_i) \quad (4.19)$$

where $\tau_i = \tau_{Hi} - \tau_a$ and $\nu_i = \nu_{Hi} - \nu_a$ are the delay and Doppler shift for the i -th path obtained using the CAF definition in equations (1.1) and by random generating the estimates of the range and velocity as

$$\hat{R}_R^{(i)} \sim N(R_R^{(i)}, \text{CRLB}_R^{(i)}) \quad (4.20)$$

$$\hat{V}_B^{(i)} \sim N(V_B^{(i)}, \text{CRLB}_V^{(i)}) \quad (4.21)$$

where $R_R^{(i)}$ and $V_B^{(i)}$ are the actual range and bistatic velocity of the target, while $\text{CRLB}_R^{(i)}$ and $\text{CRLB}_V^{(i)}$ are the Cramér-Rao lower bounds of range and velocity in the i -th path.

By random generating $R_R^{(i)}$ and $V_B^{(i)}$, the value of c_i takes into account the miss-matching at the i -th receiver, moreover, due the geometry dependent non linear transformation of equations (2.8) and (2.9), that gives the delay and the doppler as a function of the range and the bistatic velocity, the value of c_i takes also into account the effects of the distortion of the Ambiguity Function due to the bistatic geometry.

As an example, let consider the case in which $\text{CRLB}_R^{(i)}$ and $\text{CRLB}_V^{(i)}$ are low, in this case the values assumed by $R_R^{(i)}$ and $V_B^{(i)}$ are near the actual range and velocity, therefore the values assumed by τ_i and ν_i are almost zero, and hence the value assumed by c_i is near the maximum that is 1. On the other hand, for a bad bistatic geometry, the values assumed by $\text{CRLB}_R^{(i)}$ and $\text{CRLB}_V^{(i)}$ are very high, therefore there is a high probability that also τ_i and ν_i are high and hence the value assumed by them is almost zero and the observed signal is only noise. In other words, by generating in this way the value of c_i , the signal model in eq (4.14) is now dependent on the sharpness of the CAF around its maximum and to the distortion of its behaviour due to the bistatic geometry. It is clearly apparent that it is very difficult to derive the PDF of c_i and hence it is difficult to derive the Neyman-Pearson decision test. By the way, our approach is to use the same receiver of eq. (4.17) but choosing the weights p_i in a different manner. In fact, the weights in eq. (4.18) depends only on the energy path loss and they do not take into account the other effects due to the bistatic geometry. As an example, let consider the case of a target is in the baseline between the transmitter and the i -th receiver. When the

distance between the transmitter and i -th receiver is low, the expected signal to noise ratio is high and therefore the central processor using the weights in (4.18) tends to emphasize this path during the detection process. As showed, in this case the resolution is totally lost and therefore the observations from this path can significantly degrade the performance of the whole system. Therefore, the rule for selecting the weighting coefficients should be different. In particular, the weights should be highlight those channels that exhibit the best performance in terms of estimation accuracy of the target parameters instead of emphasizes those along which the $SNRs$ are the highest. In this work we propose the following weighting rule

$$p_i = \frac{\text{Trace}\{\mathbf{J}_B^{-1}(R_R^{(i)}, V_B^{(i)})\}^{-1}}{\gamma + \text{Trace}\{\mathbf{J}_B^{-1}(R_R^{(i)}, V_B^{(i)})\}^{-1}} \quad (4.22)$$

where $\text{Trace}\{\cdot\}$ is the trace operator and γ is a constant that we fixed equal to the inverse of the sum of the CRLBs of range and velocity in the monostatic case when $SNR=0\text{dB}$. In this way the weighting coefficients depend on the SNR and the normalization constraint can be viewed as a terms of comparison of the performance of the bistatic channel. That is, a channel can be considered a good channel if $\text{trace}\{\mathbf{J}_B^{-1}\}$ is lower than γ^{-1} , while a channel is bad if $\text{trace}\{\mathbf{J}_B^{-1}\}$ is greater than γ^{-1} . It is important to recall that $R_R^{(i)}$ and $V_B^{(i)}$ are the actual range and velocity of the target. Therefore, depending on the cell (x,y,V_x,V_y) under test, the central processor can easily calculate these two values for each channel knowing the position of each sensor of the multistatic system.

As apparent in eq. (4.22), the weights p_i depend on the inverse of the bistatic Fisher Information Matrix which is dependent on the energy path loss through SNR_i , on the geometry and also on the transmitted waveform. This is also important in the case of a multistatic system where multiple transmitters are used. Using the weights in (4.22) the central processor emphasizes those channels that exhibit the best performance in terms of estimation accuracy and is also able to discard those channels where the resolution is totally lost. In this case the trace of the inverse of the bistatic FIM tends to infinity and the therefore the weight p_i tends to zero. This is evident from Figure 4.15, where we plotted the weighting coefficient p_i as a function of $1/\text{trace}\{\mathbf{J}_B^{-1}\}$ for different values of the normalization constraint γ .

The value of γ can be fixed to the inverse of the sum of the CRLBs of range and velocity in the monostatic case when $SNR=0\text{dB}$. In this way the weighting coefficients depend on the SNR and the normalization constraint can be viewed as a terms of comparison of the

performance of the bistatic channel. That is, a channel can be considered a good channel if $\text{trace}\{J_B^{-1}\}$ is lower than γ^{-1} , while a channel is bad if $\text{trace}\{J_B^{-1}\}$ is greater than γ^{-1} .

Note that the receiver to implement the given test for both the weighting rules, depending on cell under test of the surveillance map, needs to continually update the weights. Moreover, note that the matrix in eq. (4.22) is 2×2 and therefore the inversion is straightforward.

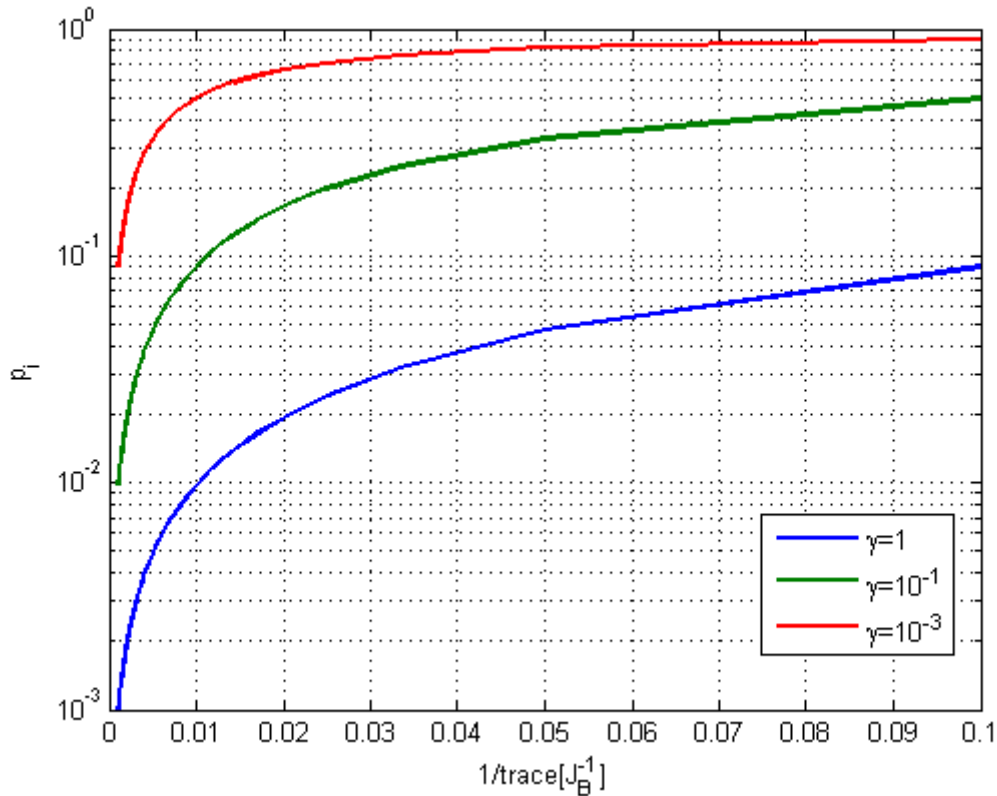


Figure 4.15 - Weighting coefficients of eq. (4.22) as a function of the inverse of the trace of the inverse of the Fisher Information Matrix for different values of the constraint γ .

4.5 Performance of the optimum multistatic detector

Figure 4.16 shows the multistatic scenario analyzed in our simulations. The multistatic system is composed by one transmitter and three receivers. The distance between the transmitter and each receiver is the same and equal to 30km. The transmitted signal is a burst of Linear Frequency Modulated pulses where $T=250\mu\text{sec}$, $T_R=1\text{msec}$, $B=1\text{MHz}$, $f_c=10\text{GHz}$ and $N=8$ (Number of coherent pulses).

The value of $Const$ in eq. (4.15) is 186 dBm^4 , in this case if $R_T=R_R=141\text{km}$ the expected

SNR is -20 dB. As showed in Figure 4.16, in our simulation we considered three cases. In the first one we considered a target in the middle of the first baseline, that is between the transmitter and the first receiver. In this case the target is moving with a speed of 250 m/sec and direction of 135° with respect to the horizontal axis. In the second case the target is in the second baseline, 10 km far from the transmitter, moving with a speed of 250 m/sec and direction of 150° . While in the third case, the target is 15 km far from the third baseline and 20 km far from the second baseline, and it is moving with a speed of 250 m/sec and direction of 180° whit respect to the horizontal axis. Table 4.2 shows the weighting coefficients obtained with both the methods, that is the “SNR” rule in eq. (4.18) and the “Trace” rule in eq. (4.22). Note that the coefficients have been normalized in order to satisfy the relationship $\sum p_i=1$. As apparent from Figure 4.16, in Case 1 the target is in the first baseline, therefore the resolution of the first receiver is totally lost also if the SNR for this path is the highest.

As apparent from Table 4.2, the coefficient corresponding to the first receiver is null using the Trace rule while it is the highest using the SNR rule. Similar considerations can be drawn for Case 2. In the third case the target is in an optimal position for all the receiver, the main difference from one receiver to the other is related only to the energy path loss, therefore the weighting coefficients obtained with both the rule are almost the same.

Figure 4.17 shows the Receiver Operating Characteristic (ROC) of the multistatic detector in eq. (4.17) for all the three analyzed cases. We also plotted the ROC obtained by forcing all the coefficients to $1/N$. As apparent from the results the ROC obtained in Case 3 (dash-dotted lines) are almost the same for the three weighting rules, while in Case 1 (solid lines) and Case 2 (dashed-lines) the performances obtained whit the Trace rule are the best. Moreover, in Case 1, the performance obtained with the SNR rule is lower than that obtained with all the weights equal to $1/N$. In this case, the SNR for the first receiver is the highest but, due to bad geometry, the resolution is totally lost. Using the SNR rule, the central processor emphasizes the observations from the first sensors and this strongly degrades the performance of the multistatic detector.

	SNR	TRACE
Case 1	$\mathbf{p}=[0.3495; 0.3328; 0.3177]$	$\mathbf{p}=[0.0000; 0.4984; 0.5016]$
Case 2	$\mathbf{p}=[0.3317; 0.3366; 0.3317]$	$\mathbf{p}=[0.5000; 0.0000; 0.5000]$
Case 3	$\mathbf{p}=[0.2735; 0.3553; 0.3712]$	$\mathbf{p}=[0.2939; 0.3449; 0.3612]$

Table 4.2- Weigting Coefficients

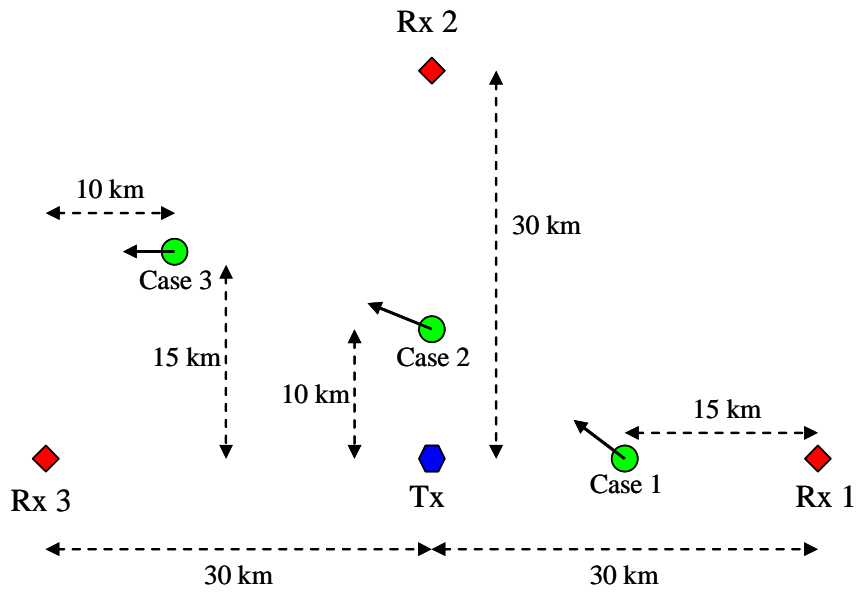


Figure 4.16 - Simulated scenario

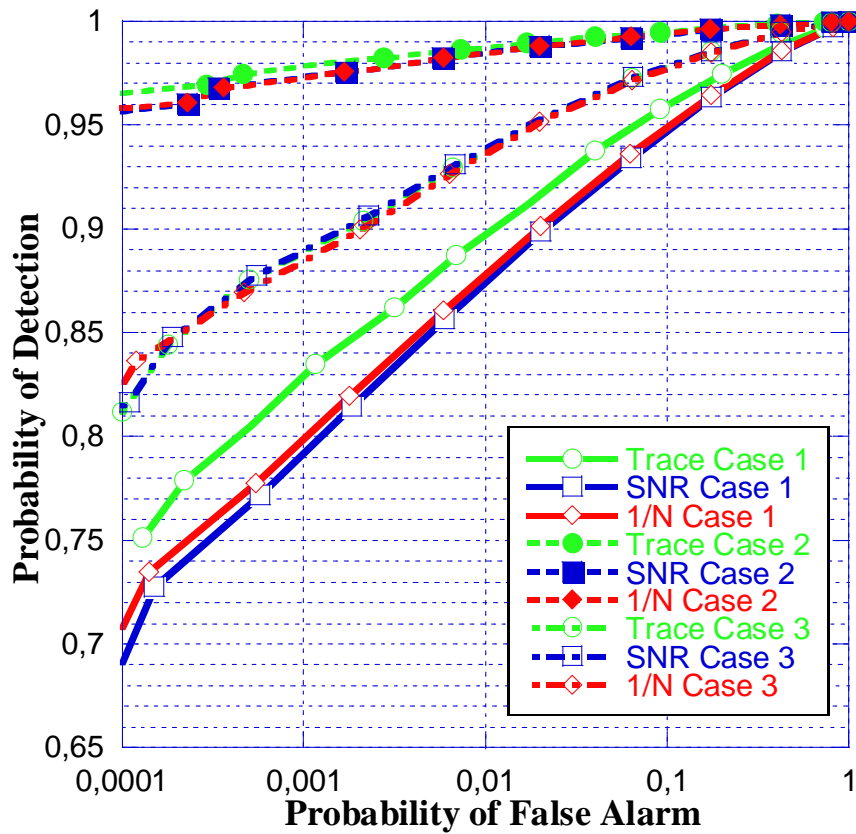


Figure 4.17 - Receiver Operating Characteristic of the Multistatic Detector.

5 Posterior Cramér-Rao Lower Bounds for Bistatic Systems

5.1 Introduction

This Chapter deals with the Posterior Cramér-Rao Lower Bound (PCRLB) for sequential target state estimators for a bistatic tracking problem. In the context of tracking, the PCRLB provides a powerful tool, enabling one to determine a lower bound on the optimal achievable accuracy of target state estimation. The bistatic PCRLBs are analyzed and compared to the monostatic counterparts for a fixed target trajectory. Two different kinematic models are analyzed: constant velocity and constant acceleration. The derived bounds are also valid when the target trajectory is characterized by the combination of these two motion.

In previous Chapters, we evaluated the bistatic Cramér-Rao Lower Bound (CRLB) for the target range and velocity both for active and passive systems. In particular, the performance in estimating these two parameters, considered here as the radar measurements, strongly depends on the bistatic geometry which clearly changes while the target is moving along its trajectory. In this Chapter, exploiting the general method provided by Tichavsky et al. [Tic98], we derive the Posterior CRLB (PCRLB) of target state for bistatic radar tracking.

The definitions of CRLB and PCRLB are similar. The CRLB is defined to be the inverse of the Fisher information matrix and provides a mean square error bound on the performance of any unbiased estimator of an unknown parameter vector. The bound is referred to as the PCRLB if this parameter vector is also subject to random fluctuations.

The bistatic bounds derived in this work are also valid for monostatic radar, considered as a bistatic system where the distance from transmitter to receiver is null. The PCRLBs of both systems are then analyzed and compared.

5.2 Analyzed Scenario

As showed in Figure 5.1, the geometry of the analyzed scenario is two-dimensional where the receiver is located at the origin while the transmitter is on the y axis at a distance from the receiver equal to the baseline L . The target is moving with the trajectory showed in figure.

Measuring the target delay and the Doppler shift, the receiver is able to evaluate the range from the receiver to target and the bistatic velocity, that is, the component of the target velocity in the direction of the bisector of the angle at the vertex which represents the target. The receiver look angle is assumed known.

The basic problem is to estimate the target position and velocity from noise corrupted range and bistatic velocity data. Next we define the problem mathematically by considering two target motion models, the constant velocity and the constant acceleration motions.

Then, we derive the CRLB for sequential estimators of the target state for the zero process noise case, that is, when the target trajectory is purely deterministic.

The PCRLB are derived assuming that the measurement sensor is operating with detection probability equal to one.

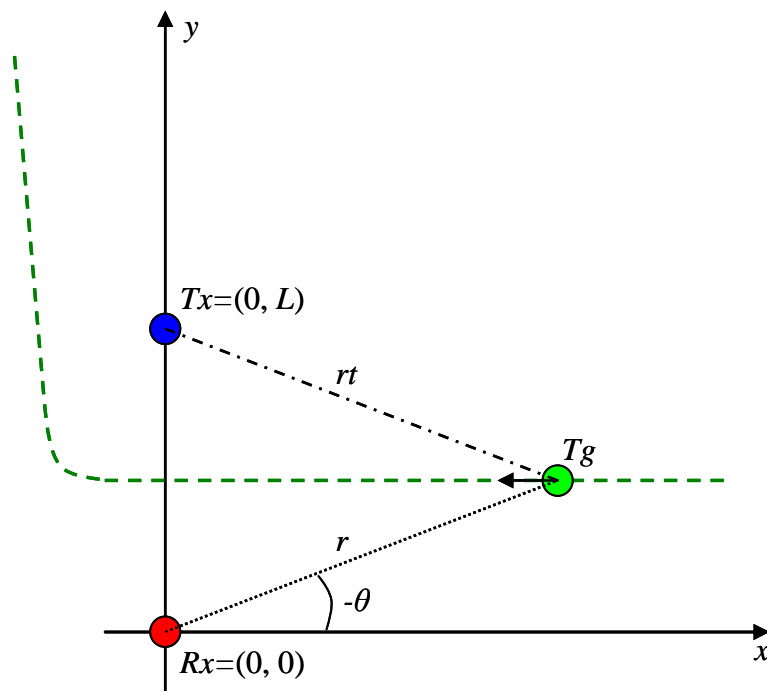


Figure 5.1- Bistatic geometry and target trajectory.

5.3 Constant velocity motion

Let's consider first the problem of the constant velocity motion. In this case the target, located at (x, y) , is assumed to move with a constant velocity (\dot{x}, \dot{y}) , with a state vector defined as $\mathbf{x}=[x, \dot{x}, y, \dot{y}]^T$. Assuming that the evolution of the state vector is purely deterministic, it is possible to write $\mathbf{x}_{k+1}=\mathbf{F}\mathbf{x}_k$, where:

$$\mathbf{F} = \begin{bmatrix} 1 & T & 0 & 0 \\ 0 & 1 & 0 & 0 \\ 0 & 0 & 1 & T \\ 0 & 0 & 0 & 1 \end{bmatrix} \quad (5.1)$$

and T is the sampling time.

The available measurements at time k are the range from receiver to target and the bistatic velocity. The measurement equations can be put in the following vectorial form:

$$\mathbf{z}_k = \mathbf{h}(\mathbf{x}_k) + \mathbf{w}_k \quad (5.2)$$

where \mathbf{z}_k is the collection of the bistatic measurements at the k th time instant while $\mathbf{h}(\mathbf{x}_k)=[r_k, v_k]^T=[h_r(\mathbf{x}_k), h_v(\mathbf{x}_k)]^T$ is a non linear vector function of the state vector \mathbf{x}_k . The bistatic measurements are affected by additive Gaussian noise \mathbf{w}_k with zero mean and covariance matrix \mathbf{R}_k . To give explicit expression of $\mathbf{h}(\mathbf{x}_k)$, referring to the bistatic geometry of Figure 5.1, it is easy to verify that

$$h_r(\mathbf{x}_k) = r_k = \sqrt{x_k^2 + y_k^2}, \quad (5.3)$$

$$h_v(\mathbf{x}_k) = v_k = \frac{\tilde{x}_k \dot{x}_k + \tilde{y}_k \dot{y}_k}{\sqrt{\tilde{x}_k^2 + \tilde{y}_k^2}} \quad (5.4)$$

where

$$\tilde{x}_k = \frac{L}{L + r_k + rt_k} x_k - x_k, \quad (5.5)$$

$$\tilde{y}_k = \frac{L}{L + r_k + rt_k} (y_k + r_k) - y_k, \quad (5.6)$$

$$rt_k = \sqrt{x_k^2 + (y_k - L)^2} \quad (5.7)$$

The problem of developing the PCRLB for bistatic radar tracking has been analyzed in [Ris04] using different target measurements, anyway the matrix \mathbf{R}_k has been modeled constant and independent on the bistatic geometry.

As showed in the previous Chapters, in bistatic radar systems, the performance in estimating the range and the bistatic velocity heavily depends on the transmitted waveform and on the geometry of the scenario, that is, the position of receivers and transmitters with respect to the position of the target. In particular we showed that the Fisher Information Matrix (FIM) of the range and the bistatic velocity is $\mathbf{J}_k^B = \mathbf{P}_k \mathbf{J}_M \mathbf{P}_k^T$ where, \mathbf{J}_M is constant and depends only on the transmitted waveform, while \mathbf{P}_k depends on the geometry. In particular, \mathbf{P}_k is redefined⁶ here as

$$\mathbf{P}_k = \begin{bmatrix} \frac{\partial \tau_k}{\partial r_k} & \frac{\partial \xi_k}{\partial r_k} \\ \frac{\partial \tau_k}{\partial v_k} & \frac{\partial \xi_k}{\partial v_k} \end{bmatrix}, \quad (5.8)$$

where τ_k and ξ_k are the delay and the Doppler shift of the radar target, that, referring to Figure 5.1, should be obtained using the geometry dependent non linear equations:

$$\tau_k = \frac{r_k + \sqrt{r_k^2 + L^2 + 2r_k L \sin \theta_k}}{c}, \quad (5.9)$$

$$\xi_k = 2 \frac{f_c}{c} v_k \sqrt{2 + \frac{r_k + L \sin \theta_k}{2\sqrt{r_k^2 + L^2 + 2r_k L \sin \theta_k}}}, \quad (5.10)$$

where c is the speed of light, f_c is the carrier frequency and θ_k is the receiver look angle.

Matrix \mathbf{J}_M depends on the transmitted waveform.

As showed before, when the transmitted signal is a sequence of linear frequency modulated (LFM) pulses, the \mathbf{J}_M is given by:

$$\mathbf{J}_M = -\frac{2T_p^2 \pi^2 \text{SNR}}{3} \begin{bmatrix} -\beta^2 & \beta \\ \beta & -1 - \left(\frac{T_R}{T_p}\right)^2 (N_p^2 - 1) \end{bmatrix}, \quad (5.11)$$

⁶ With respect to (3.17) we only changed the notation.

where N_p is the number of pulses of the transmitted burst, T_R is the pulse repetition time and T_p is the duration of each pulse, with $T_p < T_R/2$. Moreover, $\beta T_p^2 = B T_p$ is the signal effective time-bandwidth product and B is the total frequency deviation. The signal-to-noise power ratio (SNR) is inversely proportional to the path loss factor $(r_k \cdot r_{t_k})^2$ due to propagation.

Assuming that the receiver is efficient in estimating the range and the bistatic velocity, the inverse of the covariance matrix \mathbf{R}_k is given by $\mathbf{R}_k^{-1} = \mathbf{P}_k \mathbf{J}_M \mathbf{P}_k^T$. From these results it is apparent that, in the analyzed problem, the errors on the measurements are not independent and also they depend on the geometry. In [Tic98] Tichavsky et al. provided an elegant method of computing matrix \mathbf{J}_k , in particular, for the zero process noise case, the information matrix can be computed recursively using the following equation [Tay79],[Tic98],[Ris04]:

$$\mathbf{J}_{k+1} = [\mathbf{F}^{-1}]^T \mathbf{J}_k \mathbf{F}^{-1} + \tilde{\mathbf{H}}_{k+1}^T \mathbf{R}_{k+1}^{-1} \tilde{\mathbf{H}}_{k+1}, \quad (5.12)$$

where $\tilde{\mathbf{H}}_{k+1}$ is the Jacobian of $\mathbf{h}(\mathbf{x}_{k+1})$ evaluated at the true state \mathbf{x}_{k+1} ; that is:

$$\tilde{\mathbf{H}}_{k+1} = \begin{bmatrix} \frac{\partial h_r}{\partial x_{k+1}} & \frac{\partial h_r}{\partial \dot{x}_{k+1}} & \frac{\partial h_r}{\partial y_{k+1}} & \frac{\partial h_r}{\partial \dot{y}_{k+1}} \\ \frac{\partial h_v}{\partial x_{k+1}} & \frac{\partial h_v}{\partial \dot{x}_{k+1}} & \frac{\partial h_v}{\partial y_{k+1}} & \frac{\partial h_v}{\partial \dot{y}_{k+1}} \end{bmatrix}. \quad (5.13)$$

The expressions of the elements of $\tilde{\mathbf{H}}_{k+1}$ are given by

$$\frac{\partial h_r}{\partial x_{k+1}} = \frac{x_{k+1}}{r_{k+1}}, \quad (5.14)$$

$$\frac{\partial h_r}{\partial \dot{x}_{k+1}} = 0, \quad (5.15)$$

$$\frac{\partial h_r}{\partial y_{k+1}} = \frac{y_{k+1}}{r_{k+1}}, \quad (5.16)$$

$$\frac{\partial h_r}{\partial \dot{y}_{k+1}} = 0, \quad (5.17)$$

$$\frac{\partial h_v}{\partial x_{k+1}} = \frac{1}{d_{k+1}^2} \left[\begin{array}{l} \left(\dot{x}_{k+1} \frac{\partial \tilde{x}_{k+1}}{\partial x_{k+1}} + \dot{y}_{k+1} \frac{\partial \tilde{y}_{k+1}}{\partial x_{k+1}} \right) d_{k+1} + \dots \\ \dots - (\tilde{x}_{k+1} \dot{x}_{k+1} + \tilde{y}_{k+1} \dot{y}_{k+1}) \frac{\partial d_{k+1}}{\partial x_{k+1}} \end{array} \right], \quad (5.18)$$

$$\frac{\partial h_v}{\partial y_{k+1}} = \frac{1}{d_{k+1}^2} \left[\begin{array}{l} \left(\dot{x}_{k+1} \frac{\partial \tilde{x}_{k+1}}{\partial y_{k+1}} + \dot{y}_{k+1} \frac{\partial \tilde{y}_{k+1}}{\partial y_{k+1}} \right) d_{k+1} + \dots \\ \dots - (\tilde{x}_{k+1} \dot{x}_{k+1} + \tilde{y}_{k+1} \dot{y}_{k+1}) \frac{\partial d_{k+1}}{\partial y_{k+1}} \end{array} \right], \quad (5.19)$$

$$\frac{\partial h_v}{\partial \dot{x}_{k+1}} = \frac{\tilde{x}_{k+1}}{d_{k+1}}, \quad (5.20)$$

$$\frac{\partial h_v}{\partial \dot{y}_{k+1}} = \frac{\tilde{y}_{k+1}}{d_{k+1}} \quad (5.21)$$

where $d_{k+1} = \sqrt{\tilde{x}_{k+1}^2 + \tilde{y}_{k+1}^2}$. The derivatives that appear in (5.18) and (5.19) can be straightforwardly derived and are not reported here for lack of space. From these equations it is clear that the FIM \mathbf{J}_k depends on target trajectory, sensor accuracy (through \mathbf{R}_k , which is itself dependent on the target trajectory and on the transmitted waveform), the sampling interval T and the baseline length L . In particular, it is known that when the target is crossing the baseline, resolution is totally lost and therefore the errors of the measurements tends to infinity [Far09]. Matrix \mathbf{R}_k^{-1} tends to zero and hence also the second term in (5.12). In this case there is no information gain collecting the target measurements. Moreover, it is clear that for $L=0$ the bistatic PCRLBs coincide with the monostatic PCRLBs (the PCRLB are given by taking the diagonal elements of the inverse of \mathbf{J}_k).

In the monostatic case, matrix \mathbf{P}_k of (5.8) becomes diagonal and constant, therefore the errors on the measurements become independent of the geometry. Concluding, the recursion in (5.12) starts with the initial FIM \mathbf{J}_0 that, assuming the initial distribution of \mathbf{x}_0 is Gaussian, is equal to the inverse of the covariance matrix of \mathbf{x}_0 [Tic98], [Ris04].

5.4 Constant acceleration motion

For the constant acceleration motion the problems is very similar to the one treated in the previous subsection. The state vector is defined as $\bar{\mathbf{x}}=[\mathbf{x}^T, \mathbf{a}^T]^T=[x, \dot{x}, y, \dot{y}, \ddot{x}, \ddot{y}]^T$, where \ddot{x} and \ddot{y} are the accelerations along the x and y directions, which are assumed constant. Even in this case the state equation is linear and is defined as $\bar{\mathbf{x}}_{k+1} = \bar{\mathbf{F}}_k \bar{\mathbf{x}}_k$, where

$$\bar{\mathbf{F}}_k = \begin{bmatrix} \mathbf{F} & \mathbf{G}_k \\ \mathbf{0}_{2 \times 4} & \mathbf{I}_2 \end{bmatrix}. \quad (5.22)$$

\mathbf{F} is the same matrix defined in (5.1), \mathbf{I}_2 is the 2×2 identity matrix, $\mathbf{0}_{2 \times 4}$ is a matrix whose elements are zero while \mathbf{G}_k is a matrix which takes into account the effect of acceleration. In particular, $\mathbf{G}_k = \mathbf{0}_{4 \times 2}$ for the constant velocity motion, while $\mathbf{G}_k = \mathbf{G}$ for the constant acceleration motion, where

$$\mathbf{G}^T = \begin{bmatrix} T^2/2 & T & 0 & 0 \\ 0 & 0 & T^2/2 & T \end{bmatrix} \quad (5.23)$$

Considering the zero process noise case, the FIM of the state vector $\bar{\mathbf{x}}_k$ can be obtained using the following equation:

$$\bar{\mathbf{J}}_{k+1} = [\bar{\mathbf{F}}_k^{-1}]^T \bar{\mathbf{J}}_k \bar{\mathbf{F}}_k^{-1} + \bar{\mathbf{H}}_{k+1}^T \mathbf{R}_{k+1}^{-1} \bar{\mathbf{H}}_{k+1}, \quad (5.24)$$

where

$$\bar{\mathbf{F}}_k^{-1} = \begin{bmatrix} \mathbf{F}^{-1} & -\mathbf{F}^{-1} \mathbf{G}_k \\ \mathbf{0}_{2 \times 4} & \mathbf{I}_2 \end{bmatrix} \quad (5.25)$$

and, considering that the measurements of the range and the bistatic velocity do not depend on the acceleration,

$$\bar{\mathbf{H}}_{k+1} = \begin{bmatrix} \tilde{\mathbf{H}}_{k+1} & \mathbf{0}_{2 \times 2} \end{bmatrix}. \quad (5.26)$$

In this work, we are interested on evaluating the PCRLB of the target position and velocity. Therefore, it is useful to write the FIM in (5.24) using the following block matrix notation:

$$\bar{\mathbf{J}}_{k+1} = \begin{bmatrix} \mathbf{J}_{k+1} & \tilde{\mathbf{J}}_{k+1} \\ \tilde{\mathbf{J}}_{k+1}^T & \mathbf{J}_{k+1} \end{bmatrix}, \quad (5.27)$$

where the top-left matrix \mathbf{J}_k is the 4×4 information matrix of the state vector \mathbf{x}_k . After straightforward manipulation, it is easy to verify that:

$$\mathbf{J}_{k+1} = [\mathbf{F}^{-1}]^T \mathbf{J}_k \mathbf{F}^{-1} + \tilde{\mathbf{H}}_{k+1}^T \mathbf{R}_{k+1}^{-1} \tilde{\mathbf{H}}_{k+1}, \quad (5.28)$$

$$\tilde{\mathbf{J}}_{k+1} = -[\mathbf{F}^{-1}]^T \mathbf{J}_k \mathbf{F}^{-1} \mathbf{G}_k + [\mathbf{F}^{-1}]^T \tilde{\mathbf{J}}_k, \quad (5.29)$$

$$\mathbf{J}_{k+1} = \mathbf{G}_k^T [\mathbf{F}^{-1}]^T \mathbf{J}_k \mathbf{F}^{-1} \mathbf{G}_k - \tilde{\mathbf{J}}_k^T \mathbf{F}^{-1} \mathbf{G}_k - \mathbf{G}_k^T [\mathbf{F}^{-1}]^T \tilde{\mathbf{J}}_k + \mathbf{J}_k. \quad (5.30)$$

The PCRLBs on target position and target velocity estimation accuracy are given by the first four element on the principal diagonal of the inverse of $\bar{\mathbf{J}}_k$. In particular, the top-left 4×4 sub-matrix of the inverse of $\bar{\mathbf{J}}_k$ can be obtained as:

$$\left[\bar{\mathbf{J}}_{k+1}^{-1} \right]_{1:4,1:4} = \left(\mathbf{J}_{k+1} - \tilde{\mathbf{J}}_{k+1} \mathbf{J}_{k+1}^{-1} \tilde{\mathbf{J}}_{k+1}^T \right)^{-1}. \quad (5.31)$$

With respect to (5.12), in eq. (5.31) there is a term that takes into account the effects of acceleration. Moreover, considering $\mathbf{G}_k = \mathbf{0}_{4 \times 2}$, that is forcing the acceleration to zero, it is easy to verify that (5.31) is similar to (5.12), the only difference is a term that takes into account the loss of information due to the estimation of the target acceleration performed with the same dataset.

Even in this case, the monostatic PCRLBs are given by forcing the baseline $L=0$. It is clear that the result in (5.12) is useful only when the target is moving with constant velocity. On the other hand, when the target trajectory is characterized by the combination of different target motions, i.e. constant velocity followed by constant acceleration, the useful equation is (5.31) obtained by switching appropriately the matrix \mathbf{G}_k .

5.5 PCRLB for Monostatic and Bistatic radar systems

The PCRLBs of target position and velocity has been evaluated referring to the scenario of Figure 5.1. We considered both the monostatic and the bistatic cases. In the bistatic configuration, the baseline has been fixed to 50Km. The transmitted signal is a burst of $N_p=8$ LFM pulses, where $T_p=250\mu\text{sec}$, $T_R=1\text{msec}$, $B=1\text{MHz}$, $f_c=10\text{GHz}$. The target trajectory is formed of two straight lines separated by a centripetal acceleration motion. On the straight lines, the target moves with constant velocity. At $t=0$ the target is in $(x=10L, y=L/2)$ moving with constant velocity $(\dot{x}=-100, \dot{y}=0)$ m/sec. At $t=5000\text{sec}$ the target crosses the baseline while at $t=5400\text{sec}$ it starts the manoeuvre whose duration is 360 sec. At the end of the manoeuvre, the target starts to move with constant velocity $(\dot{x}=-5, \dot{y}=100)\text{m/sec}$.

The trajectory is sampled with a sampling interval of $T=1\text{sec}$. Using the results obtained in Section 5.4, Figures 5.2-5.5 show the PCRLBs of the target position and target velocity for the monostatic radar (in red, $L=0$) and for the bistatic case (in blue, $L=50$ km).

Since the magnitudes of errors, as predicted by the PCRLBs, are very large in the initial interval, the bounds are plotted for $t>4000\text{sec}$. In order to highlight the dependence of the performance of bistatic system on the geometry, the bounds have been calculated by keeping constant the SNR at 0dB.

Initially, the performance of the monostatic system and the bistatic one are the same. When the distance from receiver to target is one order of magnitude greater than the baseline, the bistatic system behaves as the monostatic one.

On the other hand, when the target approaches the baseline, the information due to the target measurements tends to zero and the information gain is only due to the a priori information.

For this reason, the bistatic PCRLBs around $t=5000\text{sec}$ are flatter than the monostatic PCRLBs. The discontinuity at $t=5400\text{sec}$ is due to the beginning of the acceleration and, after the transient state, the performance of the two systems tend to be the same. At the beginning of the transient, the bistatic PCRLB are lower than their monostatic counterparts.

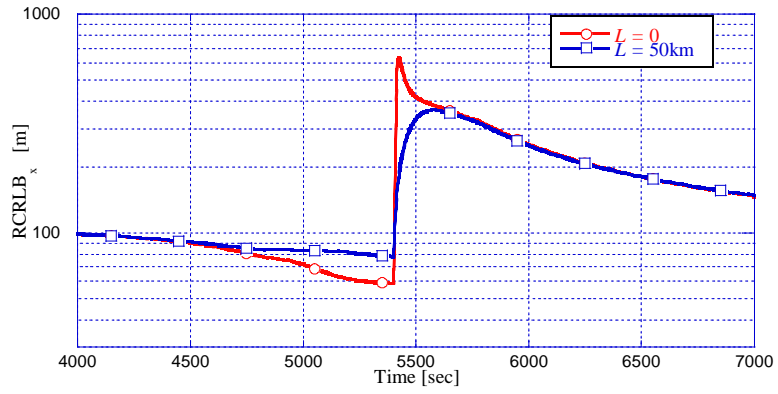


Figure 5.2 – Root of the PCRLB of the x position [m].

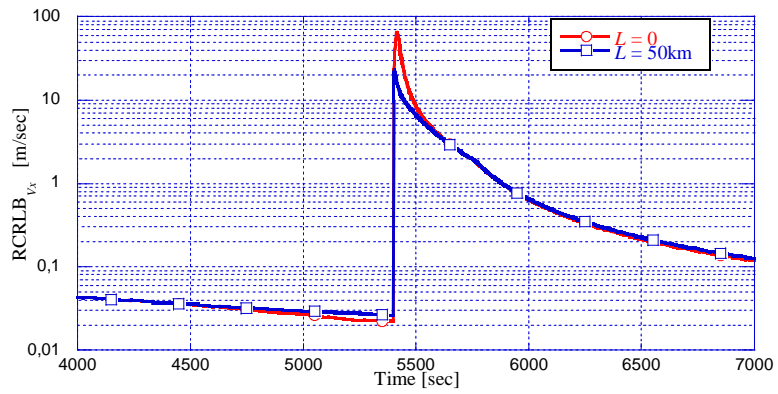


Figure 5.3 – Root of the PCRLB of the \dot{x} speed [m/sec].

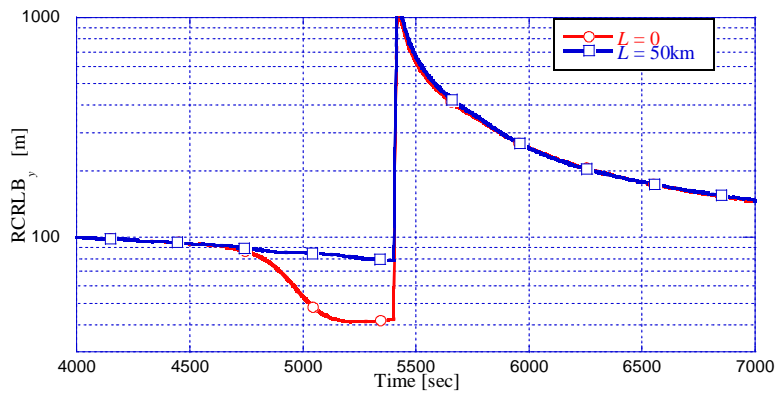


Figure 5.4 – Root of the PCRLB of the y position [m].

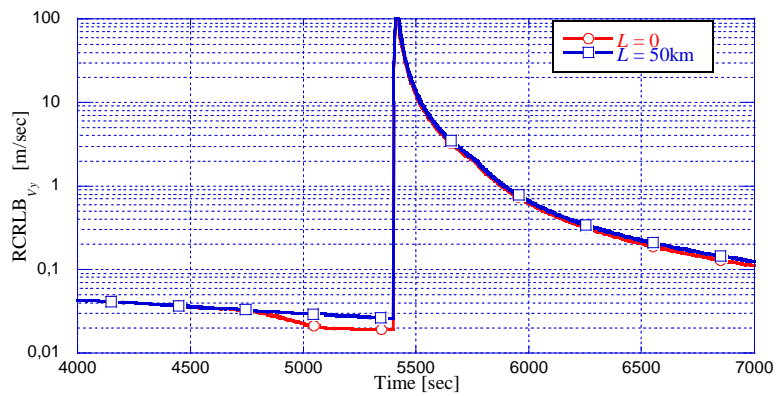


Figure 5.5 – Root of the PCRLB of the \dot{y} speed [m/sec].

Conclusions

In this work we considered a multistatic radar scenario and we derived the bistatic Cramér-Rao lower bounds on the estimation accuracy of the target range and velocity. To this purpose we exploited the relation between the ambiguity function and the Fisher information matrix, which shows how the FIM depends on the sharpness of the AF mainlobe in the range-velocity plane. In the bistatic case both geometry factors and transmitted waveforms play an important role in the shape of the AF, and therefore in the estimation accuracy of the target range and velocity. The CRLBs depend on the bistatic geometry parameters, i.e. the target direction of arrival, the bistatic baseline length and the distance between the target and the receiver. This dependence is very strong and can be appreciated considering the case of a target close to the baseline joining the transmitter and receiver. In this case, the resolution is totally lost because the target echo arrives at the receiver at the same instant as the direct signal, independent of the target location, and the Doppler shift of a target crossing the bistatic baseline must be zero, because the transmitter-to-target range changes in an equal and opposite way to the target-to-receiver range, independent of the magnitude and direction of the target velocity. The information gained through the calculation of the bistatic CRLBs can be used for the choice of the optimum transmit-receive pair in a multistatic radar system. In other words, the selection of the TX-RX pair, or set of bistatic pairs, can be based upon the values of the bistatic CRLBs for the geometry under investigation. The optimal pair was defined as that exhibiting the lowest bistatic CRLB for the target velocity or range, and the system selects the best channel dynamically, that is, using the knowledge of the CRLBs and the kinematic parameters of the target estimated in the previous time intervals.

In this work we assumed that only one couple of TX-RX is active, basically neglecting the interference among the other transmitters on the selected one. This ideal situation can be approximately achieved selecting orthogonal waveforms for all the transmitters and matching dynamically the selected receivers to the waveform of the selected transmitter.

This report also dealt with the design and performance evaluation of a multistatic detection algorithm. The analyzed multistatic detector refers to a centralized nomenclature where the data at each receiver are first collected by a central processor and then jointly combined for the detection. In particular, The most adopted coherent techniques refer to a fusion rule where the weighting coefficients are an increasing function of the expected SNR without taking into

account the dependence of the performance upon the geometry. Therefore, depending on the geometry, it is also possible that in channel with an high SNR the estimation accuracy of the target parameters is very low. In this work we proposed an Optimized Coherent Processor where the rule for obtain the weighting coefficients depends on the FIM, which is itself dependent on the SNR, the AF and therefore on the geometry and the transmitted waveform. From the results it is apparent that using the proposed technique it is possible to improve the performance of the multistatic detector. The obtained results can serve as a guideline for future multistatic fusion rule development.

We also calculated the Posterior Cramér-Rao Lower Bound (PCRLB) for sequential target state estimators for a bistatic tracking problem. We analyzed and compared the bistatic PCRLBs to the monostatic counterparts for a fixed target trajectory. In particular, we analyzed two different kinematic models: constant velocity and constant acceleration. The derived bounds are also valid when the target trajectory is characterized by the combination of these two motion.

APPENDIX A: Relation between CRLB and AF

In this appendix we report the proof of eq. (3.1). The complex signal received by the radar is

$$r(t) = s(t, \mathbf{A}) + w(t) \quad 0 \leq t \leq T \quad (\text{A.1})$$

where $w(t)$ is a zero mean complex Gaussian process and $s(t, \mathbf{A})$ is the received signal in absence of noise which depends on the vector $\mathbf{A} = [A_1 \ A_2 \ \dots \ A_N]^T$ composed by the unknown, non-random parameters that we want to estimate. We let the observation interval $[0, T]$ be long enough to completely contain the pulse.

We approach the problem by making a K -coefficient approximation of $r(t)$. Assuming that

$$\varphi_i(t) \dots i = 1, 2, \dots, K \quad (\text{A.2})$$

is a orthonormal basis, the K -coefficient approximation of $r(t)$ is given by

$$r_k(t) = \sum_{i=1}^K r_i \varphi_i(t) \quad (\text{A.3})$$

where

$$r_i = \int_0^T r(t) \varphi_i(t) dt \quad (\text{A.4})$$

Substituting eq. (A.1) into this expression, we obtain

$$r_i = s_i(\mathbf{A}) + w_i \quad (\text{A.5})$$

where

$$s_i(\mathbf{A}) = \int_0^T s(t, \mathbf{A}) \varphi_i(t) dt \quad (\text{A.6})$$

and

$$w_i = \int_0^T w(t) \varphi_i(t) dt \quad (\text{A.7})$$

Therefore, the samples r_i are independent, identically distributed (IID), complex Gaussian variables with variance σ_w^2 and mean $s_i(\mathbf{A})$, in short notation $r_i \sim CN(s_i(\mathbf{A}), \sigma_w^2)$. The probability density function of r_i is given by:

$$p_{r_i}(r_i, \mathbf{A}) = \frac{1}{\pi\sigma_w^2} e^{-\frac{|r_i - s_i(\mathbf{A})|^2}{\sigma_w^2}} \quad (\text{A.8})$$

In order to find the CRLB of the non-random parameters A_n , where $n=1,2,\dots,N$, the first step is to find the likelihood function. With obvious notation, the likelihood function can be written as

$$\Lambda_1[r_K(t), \mathbf{A}] = p_{r_K(t), \mathbf{A}}(r_K(t), \mathbf{A}) = \prod_{i=1}^K \frac{1}{\pi\sigma_w^2} e^{-\frac{|r_i - s_i(\mathbf{A})|^2}{\sigma_w^2}} \quad (\text{A.9})$$

Now, if we let $K \rightarrow \infty$, $\Lambda_1[r_K(t), \mathbf{A}]$ is not well defined. In [Van71] it is shown that we can divide a likelihood function by anything that does not depend on \mathbf{A} and still have a likelihood function. In order to avoid the convergence problem, we divide (A.9) by

$$p_{r_K(t)|H_0}(r_K(t)|H_0) = \prod_{i=1}^K \frac{1}{\pi\sigma_w^2} e^{-\frac{|r_i|^2}{\sigma_w^2}} \quad (\text{A.10})$$

before letting $K \rightarrow \infty$. Because this function does not depend on \mathbf{A} , it is legitimate to divide by it here. Let define the likelihood function

$$\Lambda[r_K(t), \mathbf{A}] = \frac{\Lambda_1[r_K(t), \mathbf{A}]}{p_{r_K(t)|H_0}(r_K(t)|H_0)} \quad (\text{A.11})$$

Substituting into this expression, cancelling common terms and taking the logarithm, we obtain

$$\begin{aligned}
\ln \Lambda[r_K(t), \mathbf{A}] &= -\frac{1}{\sigma_w^2} \sum_{i=1}^K \left[|s_i(\mathbf{A})|^2 - 2\Re(r_i^* s_i(\mathbf{A})) \right] = \\
&= -\frac{1}{\sigma_w^2} \sum_{i=1}^K \left[|s_i(\mathbf{A})|^2 - r_i^* s_i(\mathbf{A}) - r_i s_i^*(\mathbf{A}) \right]
\end{aligned} \tag{A.12}$$

Letting $K \rightarrow \infty$ we have

$$\ln \Lambda[r(t), \mathbf{A}] = -\frac{1}{\sigma_w^2} \int_0^T |s(t, \mathbf{A})|^2 dt + \frac{1}{\sigma_w^2} \int_0^T r^*(t) s(t, \mathbf{A}) dt + \frac{1}{\sigma_w^2} \int_0^T r(t) s^*(t, \mathbf{A}) dt \tag{A.13}$$

From [Kay93] the Fisher Information Matrix (FIM) is given by

$$\mathbf{J} = \begin{bmatrix} -E \left(\frac{\partial^2 \ln \Lambda[r(t), \mathbf{A}]}{\partial A_1^2} \right) & -E \left(\frac{\partial^2 \ln \Lambda[r(t), \mathbf{A}]}{\partial A_1 \partial A_2} \right) & \dots & -E \left(\frac{\partial^2 \ln \Lambda[r(t), \mathbf{A}]}{\partial A_1 \partial A_N} \right) \\ -E \left(\frac{\partial^2 \ln \Lambda[r(t), \mathbf{A}]}{\partial A_2 \partial A_1} \right) & -E \left(\frac{\partial^2 \ln \Lambda[r(t), \mathbf{A}]}{\partial A_2^2} \right) & \dots & \dots \\ \dots & \dots & \dots & \dots \\ -E \left(\frac{\partial^2 \ln \Lambda[r(t), \mathbf{A}]}{\partial A_N \partial A_1} \right) & \dots & \dots & -E \left(\frac{\partial^2 \ln \Lambda[r(t), \mathbf{A}]}{\partial A_N^2} \right) \end{bmatrix} \tag{A.14}$$

where $E(\cdot)$ is the Expectation operator.

By differentiating eq. (A.13) with respect to A_n we obtain:

$$\begin{aligned}
\frac{\partial \ln \Lambda[r(t), \mathbf{A}]}{\partial A_n} &= -\frac{1}{\sigma_w^2} \int_0^T \frac{\partial s(t, \mathbf{A})}{\partial A_n} s^*(t, \mathbf{A}) dt - \frac{1}{\sigma_w^2} \int_0^T s(t, \mathbf{A}) \frac{\partial s^*(t, \mathbf{A})}{\partial A_n} dt + \\
&+ \frac{1}{\sigma_w^2} \int_0^T r^*(t) \frac{\partial s(t, \mathbf{A})}{\partial A_n} dt + \frac{1}{\sigma_w^2} \int_0^T r(t) \frac{\partial s^*(t, \mathbf{A})}{\partial A_n} dt
\end{aligned} \tag{A.15}$$

that can be written as

$$\frac{\partial \ln \Lambda[r(t), \mathbf{A}]}{\partial A_n} = \frac{1}{\sigma_w^2} \int_0^T [r(t) - s(t, \mathbf{A})]^* \frac{\partial s(t, \mathbf{A})}{\partial A_n} dt + \frac{1}{\sigma_w^2} \int_0^T [r(t) - s(t, \mathbf{A})] \frac{\partial s^*(t, \mathbf{A})}{\partial A_n} dt \tag{A.16}$$

Differentiating again with respect to A_m we obtain:

$$\begin{aligned} \frac{\partial^2 \ln \Lambda[r(t), \mathbf{A}]}{\partial A_n \partial A_m} &= \frac{1}{\sigma_w^2} \int_0^T \left\{ -\frac{\partial s^*(t, \mathbf{A})}{\partial A_m} \frac{\partial s(t, \mathbf{A})}{\partial A_n} + [r(t) - s(t, \mathbf{A})]^* \frac{\partial^2 s(t, \mathbf{A})}{\partial A_n \partial A_m} \right\} dt + \\ &+ \frac{1}{\sigma_w^2} \int_0^T \left\{ -\frac{\partial s(t, \mathbf{A})}{\partial A_m} \frac{\partial s^*(t, \mathbf{A})}{\partial A_n} + [r(t) - s(t, \mathbf{A})] \frac{\partial^2 s^*(t, \mathbf{A})}{\partial A_n \partial A_m} \right\} dt \end{aligned} \quad (\text{A.17})$$

Taking the expectation, we obtain:

$$E\left(\frac{\partial^2 \ln \Lambda[r(t), \mathbf{A}]}{\partial A_n \partial A_m}\right) = -\frac{1}{\sigma_w^2} \int_0^T \frac{\partial s^*(t, \mathbf{A})}{\partial A_m} \frac{\partial s(t, \mathbf{A})}{\partial A_n} dt - \frac{1}{\sigma_w^2} \int_0^T \frac{\partial s(t, \mathbf{A})}{\partial A_m} \frac{\partial s^*(t, \mathbf{A})}{\partial A_n} dt \quad (\text{A.18})$$

where we observed that

$$E(r(t) - s(t, \mathbf{A})) = E(w(t)) = 0 \quad (\text{A.19})$$

Assuming that

$$s(t, \mathbf{A}) = \sqrt{E}u(t, \mathbf{A}) \quad (\text{A.20})$$

where E is the energy of $s(t, \mathbf{A})$ and $u(t, \mathbf{A})$ is a unitary energy signal, eq. (A.18) can be written as

$$E\left(\frac{\partial^2 \ln \Lambda[r(t), \mathbf{A}]}{\partial A_n \partial A_m}\right) = SNR \frac{\partial^2}{\partial A_n \partial A_m} \int_0^T |u(t, \mathbf{A})|^2 dt \quad (\text{A.21})$$

where $SNR = E/\sigma_w^2$ is the Signal to Noise Ratio.

It is interesting to observe that $\int_0^T |u(t, \mathbf{A})|^2 dt$ is the Ambiguity Function of $u(t, \mathbf{A})$ evaluated

around its maximum. Denoting $\chi(\mathbf{A}) = \int_0^T |u(t, \mathbf{A})|^2 dt$, it is possible to write

$$\mathbf{J} = -SNR \begin{bmatrix} \frac{\partial^2 \chi(\mathbf{A})}{\partial A_1^2} & \frac{\partial^2 \chi(\mathbf{A})}{\partial A_1 \partial A_2} & \cdots & \frac{\partial^2 \chi(\mathbf{A})}{\partial A_1 \partial A_N} \\ \frac{\partial^2 \chi(\mathbf{A})}{\partial A_2 \partial A_1} & \frac{\partial^2 \chi(\mathbf{A})}{\partial A_2^2} & \cdots & \cdots \\ \cdots & \cdots & \cdots & \cdots \\ \frac{\partial^2 \chi(\mathbf{A})}{\partial A_N \partial A_1} & \cdots & \cdots & \frac{\partial^2 \chi(\mathbf{A})}{\partial A_N^2} \end{bmatrix} \quad (\text{A.22})$$

Or, equivalently:

$$\mathbf{J}_{n,m} = -2SNR \frac{\partial^2 \Theta(\mathbf{A})}{\partial A_n \partial A_m} \quad (\text{A.23})$$

where $\Theta(\mathbf{A}) = \chi^2(\mathbf{A})$.

APPENDIX B: CRLBs of Doppler and Delay

When the parameters to estimate are the Delay τ and the Doppler shift ν , we have:

$$\mathbf{A} = [\tau, \nu] \quad (\text{B.1})$$

$$u(t, \mathbf{A}) = u(t - \tau)e^{j2\pi\nu t} \quad (\text{B.2})$$

Using the results derived in Appendix A, it is possible to derive the elements of the Fisher Information Matrix. Using Parseval's theorem, the first element of the FIM is given by:

$$[\mathbf{J}]_{1,1} = 2SNR \int_{-\infty}^{+\infty} \frac{\partial u(t, \mathbf{A})}{\partial \tau} \frac{\partial u^*(t, \mathbf{A})}{\partial \tau} dt = 2SNR \int_{-\infty}^{+\infty} \left| \frac{\partial u(t - \tau)}{\partial \tau} \right|^2 dt = 2SNR \int_{-\infty}^{+\infty} 4\pi^2 f^2 |U(f)|^2 df \quad (\text{B.3})$$

which is an approximate measure of the frequency spread of the signal $u(t)$.

The element 2,2 of the FIM is

$$\begin{aligned} [\mathbf{J}]_{2,2} &= 2SNR \int_{-\infty}^{+\infty} \frac{\partial u(t, \mathbf{A})}{\partial \nu} \frac{\partial u^*(t, \mathbf{A})}{\partial \nu} dt = 2SNR \int_{-\infty}^{+\infty} 4\pi^2 t^2 |u(t - \tau)|^2 dt = \\ &= 2SNR \cdot 4\pi^2 \left[\int_{-\infty}^{+\infty} t^2 |u(t)|^2 dt + 2\tau \int_{-\infty}^{+\infty} t |u(t)|^2 dt + \tau^2 \int_{-\infty}^{+\infty} |u(t)|^2 dt \right] \end{aligned} \quad (\text{B.4})$$

letting $\tau \rightarrow 0$, results

$$[\mathbf{J}]_{2,2} = 2SNR \int_{-\infty}^{+\infty} 4\pi^2 t^2 |u(t)|^2 dt \quad (\text{B.5})$$

which is an approximate measure of the time spread of the signal $u(t)$.

The elements 2,1 and 1,2 are given by

$$\begin{aligned}
[\mathbf{J}]_{1,2} &= [\mathbf{J}]_{2,1} = SNR \left\{ \int_{-\infty}^{+\infty} \frac{\partial u(t, \mathbf{A})}{\partial \tau} \frac{\partial u^*(t, \mathbf{A})}{\partial \nu} dt + \int_{-\infty}^{+\infty} \frac{\partial u^*(t, \mathbf{A})}{\partial \tau} \frac{\partial u(t, \mathbf{A})}{\partial \nu} dt \right\} = \\
&= 2SNR \cdot \Re \left\{ -j2\pi \int_{-\infty}^{+\infty} t \frac{\partial u(t-\tau)}{\partial \tau} u^*(t-\tau) dt \right\} = 2SNR \cdot \Im \left\{ 2\pi \int_{-\infty}^{+\infty} t \frac{\partial u(t-\tau)}{\partial \tau} u^*(t-\tau) dt \right\} = \text{(B.6)} \\
&= -2SNR \cdot \Im \left\{ 2\pi \int_{-\infty}^{+\infty} (t+\tau) \frac{\partial u(t)}{\partial t} u^*(t) dt \right\}
\end{aligned}$$

letting $\tau \rightarrow 0$, we have

$$[\mathbf{J}]_{1,2} = [\mathbf{J}]_{2,1} = -2SNR \cdot \Im \left\{ 2\pi \int_{-\infty}^{+\infty} t \frac{\partial u(t)}{\partial t} u^*(t) dt \right\} \quad \text{(B.7)}$$

These results are in agreement with those obtained in [Van71].

APPENDIX C: CRLBs of Doppler and Delay using a SFM pulse

Let's consider the SFM pulse

$$u(t) = \frac{1}{\sqrt{T}} e^{j\beta \sin(2\pi f_0 t + \varphi)} \text{rect}\left(\frac{t}{T}\right) \quad (\text{C.1})$$

It is easy to verify that

$$\frac{\partial u(t)}{\partial t} = \frac{1}{\sqrt{T}} j\beta 2\pi f_0 \cos(2\pi f_0 t + \varphi) e^{j\beta \sin(2\pi f_0 t + \varphi)} \text{rect}\left(\frac{t}{T}\right) \quad (\text{C.2})$$

considering that

$$\frac{\partial u(t-\tau)}{\partial \tau} = -\frac{\partial u(t)}{\partial t} \Big|_{t=t-\tau} \quad (\text{C.3})$$

the elements of the FIM are given by

$$\begin{aligned} [\mathbf{J}]_{1,1} &= 2SNR \int_{-\infty}^{+\infty} \left| \frac{\partial u(t-\tau)}{\partial \tau} \right|^2 dt = 2SNR \frac{\beta^2 4\pi^2 f_0^2}{T} \int_{-T/2}^{T/2} \cos^2(2\pi f_0 t + \varphi) dt = \\ &= 2SNR \frac{\beta^2 2\pi f_0}{T} [2\pi f_0 T + \sin(2\pi f_0 T) \cos(2\varphi)] \end{aligned} \quad (\text{C.4})$$

$$\begin{aligned} [\mathbf{J}]_{1,2} &= [\mathbf{J}]_{2,1} = -2SNR \cdot \Im \left\{ 2\pi \int_{-\infty}^{+\infty} t \frac{\partial u(t)}{\partial \tau} u^*(t) dt \right\} = \\ &= -2SNR \frac{\beta 4\pi^2 f_0}{T} \int_{-T/2}^{T/2} t \cos(2\pi f_0 t + \varphi) dt = \\ &= -2SNR \frac{2\beta \sin(\varphi)}{Tf_0} [\pi f_0 T \cos(\pi f_0 T) - \sin(\pi f_0 T)] \end{aligned} \quad (\text{C.5})$$

$$[\mathbf{J}]_{2,2} = 2SNR \cdot 4\pi^2 \int_{-\infty}^{+\infty} t |u(t)|^2 dt = 2SNR \frac{\pi^2 T^2}{3} \quad (\text{C.6})$$

Therefore, the CRLBs of the Delay τ and the Doppler shift ν are given by

$$CRLB(\tau) = [\mathbf{J}^{-1}]_{1,1} = \frac{[\mathbf{J}]_{2,2}}{[\mathbf{J}]_{1,1}[\mathbf{J}]_{2,2} - ([\mathbf{J}]_{1,2})^2} \quad (\text{C.7})$$

$$CRLB(\nu) = [\mathbf{J}^{-1}]_{2,2} = \frac{[\mathbf{J}]_{1,1}}{[\mathbf{J}]_{1,1}[\mathbf{J}]_{2,2} - ([\mathbf{J}]_{1,2})^2} \quad (\text{C.8})$$

As an example, let's consider the case in which the observation time T is a multiple integer of the period of the modulating signal, that is

$$T = \frac{k}{f_0} \quad (\text{C.9})$$

In this case, the FIM is given by

$$\mathbf{J} = 2SNR \begin{bmatrix} 4\pi^2 \beta^2 f_0^2 & -(-1)^k 2\pi\beta \sin(\varphi) \\ -(-1)^k 2\pi\beta \sin(\varphi) & \frac{\pi^2 T^2}{3} \end{bmatrix} \quad (\text{C.10})$$

then

$$CRLB(\tau) = \frac{1}{2SNR} \frac{k^2}{12\beta^2 f_0^2 \left(\frac{\pi^2 k^2}{3} - \sin^2(\varphi) \right)} \quad (\text{C.11})$$

$$CRLB(\nu) = \frac{1}{2SNR} \frac{f_0^2}{\frac{\pi^2 k^2}{3} - \sin^2(\varphi)} \quad (\text{C.12})$$

Considering that $\frac{\pi^2 k^2}{3} \gg \sin^2(\varphi)$ and taking the square root, it is possible to approximate

the RCRLB (Root Cramer-Rao Lower Bound) as

$$RCRLB(\tau) \approx \frac{1}{\sqrt{2SNR}} \frac{1}{2\pi\beta f_0} \approx \frac{1}{\sqrt{2SNR}} \frac{1}{\pi B_c} \quad (C.13)$$

$$RCRLB(v) \approx \frac{1}{\sqrt{2SNR}} \frac{\sqrt{3}f_0}{\pi k} = \frac{1}{\sqrt{2SNR}} \frac{\sqrt{3}}{T} \quad (C.14)$$

where $B_c \approx 2\beta f_0$ is the Carson's Bandwidth⁷ of $u(t)$. It is interesting to observe that $RCRLB(v)$ is inversely proportional to the time duration of the reference signal, while $RCRLB(\tau)$ is inversely proportional to its bandwidth. From this result we can observe that the best performance is obtained with modulating signals with high spectral content and poorest performance is obtained with slow varying modulating signals.

⁷ The Carson's bandwidth is the approximate bandwidth of a frequency (or phase) modulated signal. Carson's bandwidth rule is expressed by the relation $B_c = 2(\Delta f + B)$ where Δf is the peak frequency deviation, and B is the bandwidth of the modulating signal. In our case, it is easy to demonstrate that $B_c \approx 2\beta f_0$. Carson's rule does not apply well when the modulating signal contains discontinuities, such as a square wave.

APPENDIX D: CRLB derivation: Change of variables

In the previous section we derived that in the Monostatic case the elements of the FIM are given by:

$$[\mathbf{J}^M]_{n,m} = 2 \cdot SNR \left\{ \int_{-\infty}^{+\infty} \frac{\partial u^*(t, \mathbf{A})}{\partial A_m} \frac{\partial u(t, \mathbf{A})}{\partial A_n} dt + \int_{-\infty}^{+\infty} \frac{\partial u(t, \mathbf{A})}{\partial A_m} \frac{\partial u^*(t, \mathbf{A})}{\partial A_n} dt \right\} \quad (\text{D.1})$$

for easy of notation, let assume that $\mathbf{A} = [A_1 \ A_2]$.

Let's consider the case in which the vector \mathbf{A} is a function of the vector \mathbf{B} , composed by the new set of unknown, non-random parameters that we want to estimate. In this case, the FIM is given by

$$[\mathbf{J}^B]_{n,m} = 2 \cdot SNR \left\{ \int_{-\infty}^{+\infty} \frac{\partial u^*(t, \mathbf{A}(\mathbf{B}))}{\partial B_m} \frac{\partial u(t, \mathbf{A}(\mathbf{B}))}{\partial B_n} dt + \int_{-\infty}^{+\infty} \frac{\partial u(t, \mathbf{A}(\mathbf{B}))}{\partial B_m} \frac{\partial u^*(t, \mathbf{A}(\mathbf{B}))}{\partial B_n} dt \right\} \quad (\text{D.2})$$

Using the derivative chain rule (see Appendix E), we have

$$\frac{\partial u(t, \mathbf{A}(\mathbf{B}))}{\partial B_n} = \frac{\partial u(t, \mathbf{A}(\mathbf{B}))}{\partial A_1} \frac{\partial A_1}{\partial B_n} + \frac{\partial u(t, \mathbf{A}(\mathbf{B}))}{\partial A_2} \frac{\partial A_2}{\partial B_n} \quad (\text{D.3})$$

$$\frac{\partial u^*(t, \mathbf{A}(\mathbf{B}))}{\partial B_m} = \frac{\partial u^*(t, \mathbf{A}(\mathbf{B}))}{\partial A_1} \frac{\partial A_1}{\partial B_m} + \frac{\partial u^*(t, \mathbf{A}(\mathbf{B}))}{\partial A_2} \frac{\partial A_2}{\partial B_m} \quad (\text{D.4})$$

therefore, it is possible to write:

$$[\mathbf{J}^B]_{n,m} = [\mathbf{J}^M]_{1,1} \frac{\partial A_1}{\partial B_n} \frac{\partial A_1}{\partial B_m} + [\mathbf{J}^M]_{1,2} \frac{\partial A_1}{\partial B_n} \frac{\partial A_2}{\partial B_m} + [\mathbf{J}^M]_{2,1} \frac{\partial A_2}{\partial B_n} \frac{\partial A_1}{\partial B_m} + [\mathbf{J}^M]_{2,2} \frac{\partial A_2}{\partial B_n} \frac{\partial A_2}{\partial B_m} \quad (\text{D.5})$$

APPENDIX E: CRLB derivation: Chain rule

Suppose we need to derive with respect to x and y the function $z=f(u,v)$ where $u=h(x,y)$ and $v=g(x,y)$. Then for the chain rule:

$$\frac{\partial z}{\partial x} = \frac{\partial f}{\partial u} \frac{\partial u}{\partial x} + \frac{\partial f}{\partial v} \frac{\partial v}{\partial x}, \quad \frac{\partial z}{\partial y} = \frac{\partial f}{\partial u} \frac{\partial u}{\partial y} + \frac{\partial f}{\partial v} \frac{\partial v}{\partial y} \quad (\text{E.1})$$

For the second derivatives the following relations hold

$$\frac{\partial^2 z}{\partial x^2} = \frac{\partial^2 f}{\partial u^2} \left(\frac{\partial u}{\partial x} \right)^2 + 2 \frac{\partial^2 f}{\partial u \partial v} \frac{\partial v}{\partial x} \frac{\partial u}{\partial x} + \frac{\partial^2 f}{\partial v^2} \left(\frac{\partial v}{\partial x} \right)^2 + \frac{\partial f}{\partial u} \frac{\partial^2 u}{\partial x^2} + \frac{\partial^2 v}{\partial x^2} \frac{\partial f}{\partial v} \quad (\text{E.2})$$

$$\frac{\partial^2 z}{\partial y^2} = \frac{\partial^2 f}{\partial u^2} \left(\frac{\partial u}{\partial y} \right)^2 + 2 \frac{\partial^2 f}{\partial u \partial v} \frac{\partial v}{\partial y} \frac{\partial u}{\partial y} + \frac{\partial^2 f}{\partial v^2} \left(\frac{\partial v}{\partial y} \right)^2 + \frac{\partial f}{\partial u} \frac{\partial^2 u}{\partial y^2} + \frac{\partial^2 v}{\partial y^2} \frac{\partial f}{\partial v} \quad (\text{E.3})$$

$$\begin{aligned} \frac{\partial^2 z}{\partial x \partial y} = \frac{\partial^2 z}{\partial y \partial x} &= \frac{\partial^2 f}{\partial u^2} \frac{\partial u}{\partial y} \frac{\partial u}{\partial x} + \frac{\partial^2 f}{\partial u \partial v} \frac{\partial v}{\partial y} \frac{\partial u}{\partial x} + \frac{\partial f}{\partial u} \frac{\partial^2 u}{\partial x \partial y} \\ &+ \frac{\partial^2 f}{\partial u \partial v} \frac{\partial v}{\partial x} \frac{\partial u}{\partial y} + \frac{\partial^2 f}{\partial v^2} \frac{\partial v}{\partial y} \frac{\partial v}{\partial x} + \frac{\partial f}{\partial v} \frac{\partial^2 v}{\partial x \partial y} \end{aligned} \quad (\text{E.4})$$

References

- [Bra06] I. Bradaric, G.T. Capraro, D. D. Weiner, and M. C. Wicks, "Multistatic Radar Systems Signal Processing," *2006 IEEE Radar Conference*, Verona, New York, USA, April, 2006.
- [Bra07a] I. Bradaric, G.T. Capraro, D. D. Weiner, and M. C. Wicks, "A Framework for the Analysis of Multistatic Radar Systems with Multiple Transmitters," *International Conference on Electromagnetics in Advanced Applications*, Torino, Italy, September 2007.
- [Bra07b] I. Bradaric, G.T. Capraro, and M. C. Wicks, "Waveform Diversity for Different Multistatic Radar Configurations," *Asilomar Conference on Signals, Systems, and Computers*, November 2007.
- [Che98] V.S. Chernyak, *Fundamentals of Multisite Radar Systems. Multistatic Radars and Multiradar Systems*, Gordon and Breach Science Publishers, 1998.
- [Che09] V.S. Chernyak, "About the Use of Bistatic Measurements for Higher Object Localization Accuracy in Multisite Radar Systems," *2009 IEEE Radar Conference*, pp.1-6, Pasadena, USA, May 2009
- [Dad86] D'Addio, E.; Farina, A.; , "Overview of detection theory in multistatic radar," *Communications, Radar and Signal Processing, IEE Proceedings F* , vol.133, no.7, pp.613-623, December 1986
- [Dem07] A. De Maio and M. Lops, "Design Principles of MIMO Radar Detectors", *IEEE Trans. on AES*, Vol. 43, No. 3, July 2007, pp. 886-898.
- [Der10] Derham, T.; Doughty, S.; Baker, C.; Woodbridge, K.; , "Ambiguity Functions for Spatially Coherent and Incoherent Multistatic Radar," *IEEE Trans. on Aerospace and Electronic Systems*, vol.46, no.1, pp.230-245, Jan. 2010
- [Dog01] A. Dogandzic, A. Nehorai, "Cramér-Rao Bounds for estimating Range, Velocity, and Direction with and Active Array", *IEEE Trans. on Signal Processing*, Vol. 49, No. 6, June 2001, pp. 1122-1137.
- [Cap06] G. T. Capraro, A. Farina, H. Griffiths, and M. C. Wicks, "Knowledge-Based Radar Signal and Data Processing," *IEEE Signal Processing Magazine*, Vol. 23, No. 1, pp. 18-29, January 2006.
- [Con83] E. Conte; E. D'Addio; A. Farina; M. Longo , "Multistatic radar detection: synthesis and comparison of optimum and suboptimum receivers," *IEE Proceedings F, Communications, Radar and Signal Processing*, vol.130, no.6, pp.484-494, October 1983
- [Far02] A. Farina, B. Ristic, L. Timmoneri, "Cramer-Rao bound for nonlinear filtering with PD<1 and its application to target tracking", *IEEE Trans on Signal Processing*, vol. 50, issue 8, August 2002, pp. 1916-1924.
- [Far09] A. Farina, F. Gini, M. Greco, P. Stinco and L. Verrazzani, "Optimal Selection of the TX-RX Pair in a Multistatic Radar System", *COGIS'09*, Paris, France, November 2009.

- [Gin99] F. Gini and G.B. Giannakis, "Hybrid FM-Polynomial Phase Signal Modeling: Parameter Estimation and Cramér–Rao Bounds" *IEEE Trans. on Signal Processing*, Vol. 47, No. 2, February 1999.
- [Gin00] F. Gini, M. Montanari, and L. Verrazzani, "Estimation of Chirp Radar Signals in Compound-Gaussian Clutter: A Cyclostationary Approach," *IEEE Trans. on Signal Processing*, vol. 48, No. 4, pp. 1029-1039, April 2000.
- [Gre09] M. Greco, F. Gini, A. Farina, "Cramér-Rao Bounds for Bistatic Radars", *CAMSAP09*, Aruba, 13-16 December 2009.
- [Gre10a] M. Greco, P. Stinco, F. Gini, M. Rangaswamy, "Cramér-Rao Bounds and TX-RX Selection in a Multistatic Radar Scenario (invited)", *IEEE International Radar Conference 2010*, Washington DC, USA, 10-14 May 2010.
- [Gre10b] M. Greco, F. Gini, P. Stinco, A. Farina "Cramér-Rao bounds and selection of bistatic channels for multistatic radar systems", *IEEE Trans. on AES*, in press July 2010.
- [Gri05] H.D. Griffiths and C.J. Baker; "Measurement and analysis of ambiguity functions of passive radar transmissions", *2005 IEEE International Radar Conference*, 9-12 May 2005 Page(s):321 – 325.
- [Her04] M. Hernandez, B. Ristic, A. Farina, L. Timmoneri, "A comparison of two Cramer-Rao bounds for non-linear filtering with $PD < 1$ ", *IEEE Trans. On Signal Processing*, vol. 52, no. 9, September 2004, pp. 2361-2370.
- [Her06] M. Hernandez, A. Farina, B. Ristic, "A PCRLB for tracking in cluttered environments: measurement sequence conditioning approach", *IEEE TAES* vol. 42, issue 2, April 2006, vol. 42, no. 2, pp. 680-704.
- [Jac86] M.C. Jackson; , "The geometry of bistatic radar systems," *Communications, Radar and Signal Processing, IEE Proceedings F* , vol.133, no.7, pp.604-612, December 1986
- [Kay93] S.M. Kay, *Fundamentals of Statistical Signal Processing, Estimation Theory*. Englewood Cliffs, NJ: Prentice-Hall, 1993.
- [Kel61] E.J. Kelly, "The radar measurement of range, velocity and acceleration," *IRE Trans. Military Electron.*, vol. ME-5, pp. 51–57, 1961.
- [Lev04] N. Levanon, E. Mozeson, *Radar Signals*, New York: Wiley, 2004.
- [Pap05] I. Papoutsis, C.J. Baker, and H.D. Griffiths, "Netted Radar and the Ambiguity Function," *2005 IEEE International Radar Conference*, Washington DC, 2005.
- [Ric05] Mark A. Richards, Ph. D.; "Fundamentals of Radar Signal Processing" McGraw-Hill Electronic Engineering; Ch. 4, 2005.
- [Rih69] Rihaczec, A.W.: Principles of High Resolution Radar, McGraw-Hill, New York 1969.
- [Ris04] Ristic, B., Farina, A. and Hernandez, M., 'Cramér-Rao lower bound for tracking multiple targets', *IET Radar, Sonar and Navigation*, Vol.151, No.3, pp129-134, June 2004.
- [San07] G. San Antonio, D.R. Fuhrmann, F.C. Robey, "MIMO Ambiguity Functions", *IEEE Journal of Selected Topics in Signal Processing*, Volume 1, Issue 1, June 2007 Page(s):167 – 177.

- [Sko01] M. Sko01, "Introduction to Radar systems", Third Edition, McGraw-Hill, New York, NY, 2001.
- [Sti10] P. Stinco, M. Greco, F. Gini, "Data Fusion in a Multistatic Radar System (invited)", *2010 International Conference on Synthetic Aperture Sonar and Synthetic Aperture Radar*, 13-14 September, Lerici, Italy.
- [Sti11] P. Stinco, M. Greco, F. Gini, A. Farina "Posterior Cramer-Rao Lower Bounds for Bistatic Radar Systems" Submitted to: *ICASSP 2011*.
- [Tay79] J. H. Taylor, "The Cramer–Rao estimation error lower bound computation for deterministic nonlinear systems," *IEEE Trans. on Automatic Control*, vol. AC-24, pp. 343–344, April 1979.
- [Tic98] P. Tichavsky, C.H. Muravchik, and A. Nehorai, "Posterior Cramér-Rao bounds for discrete-time nonlinear filtering", *IEEE Trans.s on SP*, 46, 5 (1998), 1386-1396.
- [Tsa97] T. Tsao, M. Slamani, P. Varshney, D. Weiner, H. Schwarzlander, "Ambiguity Function for a Bistatic Radar", *IEEE Trans. on Aerospace and Electronic Systems*, Vol. 33, No. 3, July 1997, pp. 1041-1051.
- [Van71] H.L. Van Trees, *Detection, Estimation and Modulation Theory*. New York: Wiley, 1971, Vol. III.
- [Wod80] Woodward, P.M., *Probability and Information Theory, with Applications to Radar*, Pergamon Press, 1953; reprinted by Artech House, 1980.
- [Zho96] G.T. Zhou, G.B. Giannakis, and A. Swami, "On polynomial phase signals with time-varying amplitudes," *IEEE Trans. Signal Processing*, vol. 44, pp. 848–861, Apr. 1996.